

# The Apertif Radio Transient System (ARTS): Design, Commissioning, Data Release, and Detection of the first 5 Fast Radio Bursts

Joeri van Leeuwen<sup>1,2\*</sup>, Eric Kooistra<sup>1</sup>, Leon Oostrum<sup>1,2,3</sup>, Liam Connor<sup>1,4</sup>, J. E. Hargreaves<sup>1</sup>, Yogesh Maan<sup>5,1</sup>,  
Inés Pastor-Marazuela<sup>2,1</sup>, Emily Petroff<sup>2,6,7</sup>, D. van der Schuur<sup>1</sup>, Alessio Sclocco<sup>3</sup>, Samayra M. Straal<sup>8,9</sup>,  
Dany Vohl<sup>2,1</sup>, Stefan J. Wijnholds<sup>1</sup>, E. A. K. Adams<sup>1,10</sup>, B. Adebahr<sup>11</sup>, J. Attema<sup>3</sup>, C. G. Bassa<sup>1</sup>, J. E. Bast<sup>1</sup>,  
Anna Bilous<sup>1</sup>, W. J. G. de Blok<sup>1,12,10</sup>, O. M. Boersma<sup>2</sup>, A. H. W. M. Coolen<sup>1</sup>, H. Dénes<sup>1</sup>, S. Damstra<sup>1</sup>,  
J. P. R. de Reijer<sup>1</sup>, D. W. Gardenier<sup>1,2</sup>, Y. G. Grange<sup>1</sup>, A. W. Gunst<sup>1</sup>, K. M. Hess<sup>13,1,10</sup>, H. A. Holties<sup>1</sup>, B. Hut<sup>1</sup>,  
A. Kutkin<sup>1</sup>, G. Marcel Loose<sup>1</sup>, D. M. Lucero<sup>14</sup>, Á. Mika<sup>1</sup>, K. Mikhailov<sup>2,1</sup>, R. Morganti<sup>1,10</sup>, V. A. Moss<sup>15,16,1</sup>,  
H. Mulder<sup>1</sup>, M. J. Norden<sup>1</sup>, T. A. Oosterloo<sup>1,10</sup>, Emaneula Orrú<sup>1</sup>, Z. Paragi<sup>17</sup>, A. P. Schoenmakers<sup>1</sup>,  
K. J. C. Stuurwold<sup>1</sup>, S. ter Veen<sup>1</sup>, W. A. van Cappellen<sup>1</sup>, J. M. van der Hulst<sup>10</sup>, G. N. J. van Diepen<sup>1</sup>, Y. Y. Wang<sup>2</sup>,  
A. W. Zanting<sup>1</sup>, and J. Ziemke<sup>1,18</sup>

<sup>1</sup> ASTRON, the Netherlands Institute for Radio Astronomy, Oude Hoogeveensedijk 4, 7991 PD Dwingeloo, The Netherlands

<sup>2</sup> Anton Pannekoek Institute, University of Amsterdam, Postbus 94249, 1090 GE Amsterdam, The Netherlands

<sup>3</sup> Netherlands eScience Center, Science Park 402, 1098 XH Amsterdam, The Netherlands

<sup>4</sup> Cahill Center for Astronomy, California Institute of Technology, Pasadena, CA, USA

<sup>5</sup> National Centre for Radio Astrophysics, Tata Institute of Fundamental Research, Pune 411007, Maharashtra, India

<sup>6</sup> Veni Fellow

<sup>7</sup> Department of Physics, McGill University, 3600 rue University, Montréal, QC H3A 2T8, Canada

<sup>8</sup> NYU Abu Dhabi, PO Box 129188, Abu Dhabi, United Arab Emirates

<sup>9</sup> Center for Astro, Particle, and Planetary Physics (CAP<sup>3</sup>), NYU Abu Dhabi, PO Box 129188, Abu Dhabi, United Arab Emirates

<sup>10</sup> Kapteyn Astronomical Institute, University of Groningen, PO Box 800, 9700 AV Groningen, The Netherlands

<sup>11</sup> Astronomisches Institut der Ruhr-Universität Bochum (AIRUB), Universitätsstrasse 150, 44780 Bochum, Germany

<sup>12</sup> Dept. of Astronomy, Univ. of Cape Town, Private Bag X3, Rondebosch 7701, South Africa

<sup>13</sup> Instituto de Astrofísica de Andalucía (CSIC), Glorieta de la Astronomía s/n, 18008 Granada, Spain

<sup>14</sup> Department of Physics, Virginia Polytechnic Institute and State University, 50 West Campus Drive, Blacksburg, VA 24061, USA

<sup>15</sup> CSIRO Astronomy and Space Science, Australia Telescope National Facility, PO Box 76, Epping NSW 1710, Australia

<sup>16</sup> Sydney Institute for Astronomy, School of Physics, University of Sydney, Sydney, New South Wales 2006, Australia

<sup>17</sup> Joint Institute for VLBI ERIC (JIVE), Oude Hoogeveensedijk 4, 7991 PD Dwingeloo, The Netherlands

<sup>18</sup> University of Oslo Center for Information Technology, P.O. Box 1059, 0316 Oslo, Norway

May 26, 2022

## ABSTRACT

Fast Radio Bursts must be powered by uniquely energetic emission mechanisms. This requirement has eliminated a number of possible source types, but several remain. Identifying the physical nature of Fast Radio Burst (FRB) emitters arguably requires good localisation of more detections, and broadband studies enabled by real-time alerting. We here present the Apertif Radio Transient System (ARTS), a supercomputing radio-telescope instrument that performs real-time FRB detection and localisation on the Westerbork Synthesis Radio Telescope (WSRT) interferometer. It reaches coherent-addition sensitivity over the entire field of the view of the primary-dish beam. After commissioning results verified the system performed as planned, we initiated the Apertif FRB survey (ALERT). Over the first 5 weeks we observed at design sensitivity in 2019, we detected 5 new FRBs, and interferometrically localised each of these to 0.4–10 sq. arcmin. All detections are broad band and very narrow, of order 1 ms duration, and unscattered. Dispersion measures are generally high. Only through the very high time and frequency resolution of ARTS are these hard-to-find FRBs detected, producing an unbiased view of the intrinsic population properties. Most localisation regions are small enough to rule out the presence of associated persistent radio sources. Three FRBs cut through the halos of M31 and M33. We demonstrate that Apertif can localise one-off FRBs with an accuracy that maps magneto-ionic material along well-defined lines of sight. The rate of 1 every ~7 days next ensures a considerable number of new sources are detected for such study. The combination of detection rate and localisation accuracy exemplified by the 5 first ARTS FRBs thus marks a new phase in which a growing number of bursts can be used to probe our Universe.

**Key words.** FRBs – pulsars: general – instrumentation

\* E-mail: [leeuwen@astron.nl](mailto:leeuwen@astron.nl)

# 1. Introduction

## 1.1. Fast radio transients

Of all the time variable sources observable with modern radio telescopes, none have produced such a flurry of excitement in recent years as Fast Radio Bursts (FRBs). These bursts were discovered in 2007 by Lorimer et al. and have since emerged as a unique source class characterized by bright, short radio pulses with fluences  $\mathcal{F} \sim 1 \text{ Jy ms}$ . Thanks to large-scale, high time resolution radio surveys the population of known FRBs has grown rapidly, with more than 600 FRB sources now published (see Petroff et al. 2019a, 2021, for recent reviews).

While the population of FRBs has grown rapidly, and even though a subset ( $\sim 4\%$ ) of FRBs were discovered to repeat (Spitler et al. 2016; CHIME/FRB Collaboration et al. 2019; Fonseca et al. 2020), the progenitors of FRBs remain a mystery. The detection in 2020 of a bright FRB-like burst from a magnetar in our own Galaxy (CHIME/FRB Collaboration et al. 2020; Bochenek et al. 2020) has given weight to theories that FRBs are produced by highly magnetised neutron stars, perhaps in extreme environments, in distant galaxies. However, a wide range of other theories have also been proposed to explain FRB emission, from neutron stars to black holes to stellar explosions (see Platts et al. 2019, for a theory review), and indeed multiple channels that produce such energetic millisecond radio bursts may exist throughout the Universe.

### 1.1.1. Current survey challenges

Much observational progress has occurred since FRBs were first discovered; however, many fundamental questions about the nature of FRBs remain. The total fraction of FRBs that repeat remains an essential open question in the field, with many attempts made to model the underlying population (Gardenier et al. 2021; James et al. 2020). Sustained follow-up of an FRB source is needed to detect repeats; whether all FRBs eventually reappear actively drives investigation in ongoing and upcoming surveys.

More specific properties related to FRBs are also being studied in detail with new surveys. The polarization behavior of FRBs may provide important insight into their emission mechanism, but only a subset of FRBs have known polarization information due to the need to preserve higher time resolution data. Among bursts with polarization data, many are highly linearly polarized (Michilli et al. 2018; Bannister et al. 2019; Fonseca et al. 2020; Connor et al. 2020); others, however, show distinct circular polarization (Petroff et al. 2015a; Kumar et al. 2022; Day et al. 2020). Some linearly polarized FRBs have been seen to reside in highly magnetized (Michilli et al. 2018) and highly variable (Hilmarsson et al. 2021) environments.

Recently, periodic behavior on several timescales has also been observed for a number of FRBs. Two sources, FRB 20121102A and FRB 20180916B, have distinct windows of active emission, periodic on timescales of  $\sim 160$  and  $16.3$  days, respectively (Rajwade et al. 2020; Cruces et al. 2021; CHIME/FRB Collaboration et al. 2020). The activity window of FRB 20180916B is frequency dependent (Pastor-Marazuela et al. 2021; Pleunis et al. 2021b), perhaps indicative of precession or occultation by a binary wind. Sub-burst periodicity (periodic spacing of sub-components within a single FRB pulse), has also been observed at high significance for one FRB (CHIME/FRB Collaboration et al. 2021a) and at lower significance for three others (CHIME/FRB Collaboration et al. 2021a; Pastor-Marazuela et al. 2022a).

Despite the high all-sky FRB rate, estimated to be a few thousand FRBs  $\text{sky}^{-1} \text{ day}^{-1}$  (Chawla et al. 2017), there are many challenges facing current instruments searching for these bursts. Blind searches for FRBs require covering a range of pulse duration trials; they also necessitate searching a large range of dispersion measures (DMs). This DM corresponds to the integrated electron column density along the line of sight, and is observed as a frequency dependent time delay across the observing bandwidth. The enormous search parameter space requires dedicated hardware and software, typically housed on a massive compute cluster to keep up with data streaming off the telescope.

Effective FRB searches further require a large instantaneous field-of-view survey instrument, to maximise the probability of observing the location on the sky location where an FRB goes off. In the past, this has come at the expense of localization accuracy, and many FRBs are only localized to regions on the sky of  $10' \times 10'$ . An increasingly interesting area of investigation is the study of FRB host galaxies, but so far only two dozen hosts have been identified through precision localization<sup>1</sup> as this often requires a radio interferometer, or even very long baseline interferometry (Marcote et al. 2020).

In addition to the challenges of understanding the underlying population(s) of FRBs, their physical properties, and their progenitors, there are also technical challenges involved in their discovery at scale. With next generation telescopes such as the Square Kilometre Array (SKA) it will no longer be possible to preserve the raw survey data for offline searches (Macquart et al. 2015). Instead, new sources will need to be identified in real time to capture the telescope data for later analysis. New automated FRB search techniques and pipelines taking advantage of classification and machine learning tools will need to be developed in the coming years to prepare for this eventuality (Connor & van Leeuwen 2018).

## 1.2. The era of interferometers for time domain

To address all these challenges, new FRB search efforts are increasingly employing interferometers to survey the sky (Caleb et al. 2017; Bannister et al. 2017; Maan & van Leeuwen 2017; Law et al. 2018; CHIME/FRB Collaboration et al. 2018). Interferometers, coherently or incoherently combining signals from many smaller elements or dishes, have the advantage of a large instantaneous field of view. Recent technological advances have resulted in new receivers such as Phased Array Feeds (PAFs; Sect. 2), which further place many additional elements at the focus of each dish of a telescope array.

### 1.2.1. Processing power

One of the largest challenges of interferometric radio astronomy has been, and still is, the computation. Beamforming a large part of the telescope field of view requires a powerful signal processor to combine all elements in phase. This is more difficult still when combining the multi-element PAF systems to form beams on the sky. Forming coherent beams, and searching the time stream of each for impulsive radio signals such as FRBs, provides an added technical challenge.

Faster and more agile processing units available in recent years have made it possible to form more beams and search them quickly, in some cases in real time. These searches still require large compute clusters to deal with the massive amounts of data streaming from the telescope and distribute it over many pro-

<sup>1</sup> <https://frbhosts.org/>

cessing nodes. Many FRB search efforts, including those with Apertif that we will describe next, now house dedicated computing clusters on-site to search the data in real time for bursts (Sect. 3).

### 1.2.2. Localisation

The raw localisation ability of an interferometer depends on the length of the longest baseline, and the ability to coherently beam-form all resulting resolution elements. Even more precise localisation is possible for brighter signals that appear in several such beams (cf. Sect. 5.1.4), or where the raw voltage streams from the telescope remain available for refining correlation and beamforming offline. While the main benefit of PAFs on an interferometer is their increased field-of-view, detections in multiple PAF beams can provide improved localization of a source such as a new FRB.

For FRBs, arcsecond or better localisation is needed to identify a host galaxy unambiguously (Eftekhar et al. 2018), and interferometers provide the only path to such an association. More than 20 FRBs have been precisely localised and traced back to their hosts using interferometric arrays such as ASKAP, DSA-10, the EVN, and the VLA (e.g., Chatterjee et al. 2017; Bannister et al. 2019; Ravi et al. 2019; Marcote et al. 2020).

### 1.3. The benefits of real-time search

Since it is unknown whether all FRBs repeat, and on what timescale an individual source will produce repeating pulses, the goal in most cases is to localise an FRB from the discovery pulse. Identifying an FRB in real time in the data stream can aid localisation efforts, particularly in the case where the data are archived at lower resolution or the raw voltages are not stored. If an FRB is found in the incoming signal, data can be preserved at higher resolution and/or with the full Stokes parameters (e.g., Petroff et al. 2015a; Fonseca et al. 2020).

With a real-time FRB detection it also becomes possible to trigger other telescopes to conduct multi-wavelength and multi-messenger follow-up. Such emission has been predicted in various regimes (optical, X-ray, gravitational waves, etc.) by several theories (Platts et al. 2019), but as yet no emission outside the radio regime has been observed for extragalactic FRBs. X-ray emission from the Galactic magnetar SGR 1935+2154 coincident with a bright radio burst (Mereghetti et al. 2020) shows that such emission may be detectable if follow-up observations are conducted promptly. Triggers on FRB events are now possible with Virtual Observatory Events (VOEvents) for FRBs (Petroff et al. 2017).

The highest and lowest radio frequencies at which FRBs are detectable remain unknown. Early blind and triggered searches with the Low Frequency Array (LOFAR) and the Murchison Widefield Array (MWA) at frequencies of 100–200 MHz were unsuccessful (Coenen et al. 2014; Sokolowski et al. 2018; Chawla et al. 2020). However, studies of repeating FRBs at low frequencies, including commensal observing between WSRT and LOFAR, have proven more fruitful. Several bursts from repeating FRB 20180916B have been detected by LOFAR, leading to the discovery of frequency-dependent activity windows for this source (Pastor-Marazuela et al. 2021; Pleunis et al. 2021b). Searches for coincident emission at high and low radio frequencies require real-time classification and triggering.

### 1.4. Solutions with ARTS on Apertif

To investigate some of these outstanding core questions on FRBs, we designed the Apertif Radio Transient System (ARTS; van Leeuwen 2014) to harness Apertif, the APERTure Tile In Focus (van Cappellen et al. 2022) on the Westerbork Synthesis Radio Telescope (WSRT) for finding and studying FRBs.

The system operates on an interferometer, the WSRT, to provide a spatial resolution of order  $10' \times 10''$ . Apertif, the new PAF front-end system at Westerbork, delivers a large instantaneous Field of View (FoV), of 8.2 sq. deg. Where the previous system produced a single primary beam, the new front ends generate 40. Together these increase the FoV by a factor 30. Although the antenna elements and amplifiers are not cryogenically cooled, Apertif operates at a nominal system temperature of 70 K (Oosterloo et al. 2009). The bandwidth is 300 MHz around 1.4 GHz, in two linear polarisations. Of the 12 dishes outfitted with PAFs, the 8 equidistant ones that are most efficiently combined at full sensitivity together deliver a gain of  $\sim 1$  K/Jy. That sensitivity is comparable to the successful Parkes FRB surveys, but at much larger field of view. Apertif thus has the potential to deeply survey the entire fast-transient sky in radio. A search pipeline and dedicated cluster identify FRBs in real-time, and resolve their structure at high time and frequency resolution ( $82 \mu\text{s} / 195 \text{ kHz}$ ).

In this paper we describe ARTS and its first discoveries. We outline its science potential (Sect. 2), describe the design and implementation (Sects. 3–5), and present the commissioning results (Sect. 6), system performance (Sect. 7), and survey planning (Sect. 8). In Sect. 9 and 10 we present and discuss our first science results, which include the discovery of 5 new FRBs. We close with our data and code releases (Sect. 11), plans and expectations (Sect. 12) and conclusions (Sect. 13). Supporting details are found in Appendix A–D.

The above sections outline the complete system, providing the reader with the overall rationale, setup and results. More specialist readers are suggested to start with the relevant sections and optionally follow back the references there. Astronomers mostly interested in the newest results could read Sects. 2, 6, 9, 10 and 13. Time-domain specialists could add Sects. 3–5, 7. Astronomers interested in FRB populations and surveys should add Sects. 7, 8 and 12. For reproducing or improving the system and results, use Sect. 11 and Appendix A–D.

## 2. Apertif for Time Domain: ARTS

The Apertif time-domain potential is realised through ARTS, an instrument that can search wide fields for fast transients.

Downstream from the PAFs, high-throughput and high-performance processing hardware enables analysis of this full field and bandwidth. Processing revolves around Field-Programmable Gate Arrays (FPGAs) for channelisers, correlators, and a hierarchy of beamformers (BFs), and around CPUs and Graphics processing units (GPUs) for pipelines. These are directed by modern firmware and software, powering a real-time detection system that combines the new, large FoV with the high angular resolution of the array. ARTS is directly connected to LOFAR (van Haarlem et al. 2013), also operated by ASTRON.

### 2.1. Science Motivation

The system was designed around our goals of discovering and characterizing FRBs, primarily; and our aims of finding and studying neutron stars, and the time-domain counterparts of slow, image-domain transients, secondarily.



### 2.1.1. Fast Radio Bursts

Using FRBs as cosmological tools and understanding the underlying source population(s) requires a large number of detections – thus, a survey with good sensitivity, FoV, and time on sky. These three characteristics are provided by ARTS. Given the estimated  $10^3$ – $10^4$  bursts per day of fluence  $>1$  Jy ms (e.g., Chawla et al. 2017), many will occur in the Apertif 8-deg<sup>2</sup> field of view. As Apertif is a full-time survey machine, ARTS detects an FRB roughly every week of observing (see Sect. 12 and Maan & van Leeuwen 2017). ARTS combines high time and frequency resolution with the ability to capture full-Stokes polarisation data. It features a new GPU FRB search pipeline, and a machine learning classifier to better identify and trigger on FRB candidates.

Potentially most important in determining the formation of FRBs is localising the bursts. If FRBs are formed by young neutron stars, the galaxy in which they reside will need to have recently been forming massive stars. To identify the host galaxy with high confidence, the FRB position error box must be small enough to hold only a single candidate host. A young neutron star emitting FRBs may still be surrounded by a nebula, that could be detected in follow-up observations if the FRB is well enough localised. Theories in which Active Galactic Nuclei (AGNs) are related to the formation of FRBs could be falsified if localisation regions never contain these; or continue to be possible if they do. Finally, for nearby bursts, sub-arcsec localisation, using Very Long Baseline Interferometry (VLBI), can connect the (repeating) FRB emitters with features *within* the host galaxy. ARTS contains the hardware to connect the WSRT to VLBI (Sect. 4.1.3); but more importantly, the addition of Apertif onto an interferometer with a baseline of over 1 km provides good *instantaneous* FRB localisation (Sect. 7.4).

### 2.1.2. Neutron Stars

The surface gravity of these extremely compact stars, about  $10^9$  times the gravity on Earth, is the largest of any object visible in the Universe. The internal densities of ten times nuclear density have not existed elsewhere since the Universe was  $\sim 1$  ms old.

The combination of this high density and the millisecond rotation periods turns pulsars, radio-emitting neutron stars, into near-perfect cosmic time keepers (e.g. Hulse & Taylor 1975). Performing high precision pulsar timing on individual binary stars, such as double neutron star (DNS) systems, informs us of the underlying binary evolution (e.g. van Leeuwen et al. 2015), and enables tests of general relativity (Kramer et al. 2006; Desvignes et al. 2019).

Three groups of neutron stars are only very sporadically active in radio: rotating radio transients (RRATs), intermittent pulsars, and radio-transient magnetars. Given the odds against their detection, the number of such transient neutron stars must be comparable to that of radio pulsars (Keane et al. 2011).

ARTS performs full-FoV searches for single pulses of such pulsars, in a survey mode. It can also provide a high-time-resolution data stream, with real time coherent-dedispersion, and online folding, for a timing mode. Together these allow for both searches for, and studies of, radio-emitting neutron stars.

### 2.1.3. Prompt and slow emission from neutron-star mergers

The orbits of DNSs decay, due to the emission of gravitational waves, until eventually the neutron stars merge. The energy reservoir in this coalescence is so large that multiple stages could produce radio emission, on different timescales (see, e.g., Chu

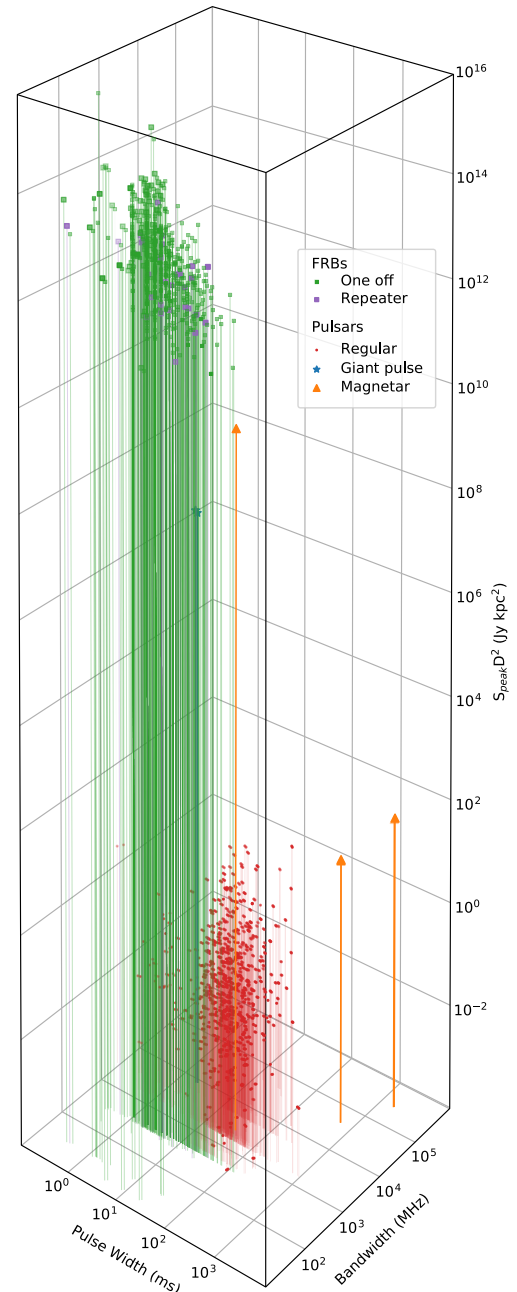


Fig. 1: Phase space diagram of emission duration and emission bandwidth versus pseudo luminosity ( $S_{pk} D^2$ ), for different fast radio transients at peak flux  $S_{pk}$  and distance  $D$ . FRBs are similar to other fast transients in their short and relatively broad-band emission; but in pseudo luminosity they strongly stand out from the pulsars, magnetars, and giant pulses also plotted. Catalog data, per 2022 Feb 1, taken from FRBCAT (Petroff et al. 2016), the Transient Name Server (TNS; [www.wis-tns.org](http://www.wis-tns.org)), ATNF (Manchester et al. 2005), and EPN were complemented by individual data from Camilo et al. (2006), Maan et al. (2019), Dai et al. (2019), Pearlman et al. (2018), Mikami et al. (2016), Bera & Chengalur (2019), and Bochenek et al. (2020).

et al. 2016). Prompt emission could possibly form at the merger, and possibly at slightly later time during the collapse of an intermediary massive neutron star into a black hole. Incoherent radio emission is expected from the reverse shock and the afterglow, and produces an image-domain, slow radio transient (Hal-



linan et al. 2017). Apertif allows for the study of both kinds of emission. Afterglow searches are carried out in image domain (Boersma et al. 2021) while prompt emission could be detected in time domain.

## 2.2. Key Apertif features for time domain studies

### 2.2.1. Regular interferometer

Wide-field transient surveys at both full (coherent-addition) sensitivity and high time resolution are almost always limited by the large computational demands involved. In the LOFAR surveys, the tied-array beams cover about 1/9th of the potential FoV (the stations beam; Coenen et al. 2014; Sanidas et al. 2019). In the Square Kilometre Array (SKA), the planned 1500 beams of SKA1-Mid cover 1/3rd of the primary beam (Smits et al. 2009). No sparse two-dimensional or irregularly laid-out interferometer has the capability to find fast transients at full sensitivity, over its entire FoV. One unique feature of the WSRT is its linear and regularly-spaced, E-W layout. This produces full-sensitivity Tied-Array Beams (TABs) that are not single, small circular beams, but have a large area in the N-S direction, and multiple sensitive sidelobes (Janssen et al. 2009). This means parallel coherent beams do not need to be computed over the entire 2-D FoV, but only over the 1-D distance between the main lobe and the first sidelobe (Sect. 2.4.2). Exploiting this fact allows us to overcome the computing limitations of full-FoV surveys with e.g., LOFAR and SKA.

This elongation of the TABs in the N-S direction has a downside: short-lived transients such as FRBs can only be localised to modest precision in that direction. The instantaneous localisation in the E-W direction, on the other hand, is very good ( $\sim 10''$ ). Additionally, every time a source repeats at a different hour angle, the localisation ellipse rotates on the sky. For repeating sources, the accurate E-W localisation thus translates to an accurate final localisation on the sky of about  $10'' \times 10''$  (see, e.g., Maan & van Leeuwen 2017, and Sect. 7.4).

### 2.2.2. Steerable dishes

For FRB and slow transient science, the ability of WSRT to point its dishes gives Apertif a significant advantage over other wide-field surveys in the northern hemisphere. A fixed, transit instrument such as CHIME is able to search its full FoV in part because a significant portion of its budget was dedicated to compute rather than building steerable dishes. This comes with the limitation that sources can only be observed for a relatively short time, at transit.

Because the WSRT dishes can be pointed over the entire hemisphere, and track much longer than fixed apertures, Apertif is able to dedicate significant follow-up time to repeating FRBs that are known to be active (cf. Pastor-Marazuela et al. 2021), gravitational wave afterglows, or Galactic neutron stars.

### 2.2.3. Digital backend: commensal systems

The pulsar surveys in which the first FRBs were found (e.g., Lorimer et al. 2007; Thornton et al. 2013; Spitler et al. 2014) operated only during a relatively small fraction of their total available telescope time. And yet, for rare bursts such as these, the total time on sky is exceedingly important. Systems that search for FRBs in a secondary mode – commensal to other, primary projects that determine such characteristics (e.g. pointing) – are thus very valuable. Commensal systems such as CRAFT

(Macquart et al. 2010; Bannister et al. 2017) and CHIME/FRB (CHIME/FRB Collaboration et al. 2019) have found FRBs with this approach. Exploiting the fact that the incoming Apertif PAF data and the modular hardware can be easily duplicated, ARTS was designed and built to run in parallel<sup>2</sup> to all other imaging Apertif surveys (Adams & van Leeuwen 2019; Hess et al. 2022). Coherently combining the 8 WSRT dishes that are equidistant in the imaging “Maxi-Short” configuration, would produce a commensal transient search with the same wide field, and similar sensitivity, as the dedicated survey.

### 2.2.4. Digital backend: high resolution

The high time and frequency resolution of the ARTS digital backend offers an advantage for both the study of known pulsars and FRBs (see, e.g., Bilous et al. 2022; Oostrum et al. 2020, respectively) as well as the detection of new sources. Many FRBs appear to be sub-millisecond in duration, which means a large number of bursts are currently missed due to the deleterious effects of instrumental smearing (Connor 2019). ARTS searches filterbank intensity data with more favorable smearing properties than comparable instruments, boosting its detection rate and enabling the discovery of higher-DM, narrower FRBs.

### 2.2.5. Connection to LOFAR

The linear-array nature of WSRT means it can localise an FRB very well in the E-W direction but only to modest N-S precision (cf. Sect. 2.4.2). But if it emits over a broad band, this same FRB will arrive later at low frequencies. Triggering the LOFAR all-sky Transient Buffer Boards (TBBs; Stappers et al. 2011; ter Veen 2015; ter Veen et al. 2019) on the FRB, and detecting it at 150 MHz, would allow for localisation using the two-dimensional array of LOFAR stations over The Netherlands and Europe. That would pinpoint the FRB with arcsec precision.

Previous blind LOFAR searches (Coenen et al. 2014; Karastergiou et al. 2015; Sanidas et al. 2019; ter Veen et al. 2019; van Leeuwen et al. 2020) have not found FRBs. This could partly be caused by the residual dispersion smearing that remains after trial dedispersion at such low frequencies. In the triggered case, the dispersion measure (DM) is known, allowing for more accurate dedispersion plus a significant reduction of the number of DM trials, improving detection confidence levels.

Still, also when the DM was known, low-frequency FRB observations were unsuccessful before 2021 (see, e.g., Houben et al. 2019). Only with the detection of FRB 20180916B were FRBs seen for the first time below 200 MHz; and while we found that the all-sky low-frequency FRB rate is appreciable (Pastor-Marazuela et al. 2021), no single FRB burst was ever seen to emit at both 150 MHz and 1.4 GHz. The simultaneous ARTS-LOFAR observing that enabled these detections is detailed in Pastor-Marazuela et al. (2021).

## 2.3. Design and engineering method

Maximally using the unique benefits of Apertif to further time-domain research could lead to a complex system. The resulting instrument was expected to consist of many layers of hardware, firmware, software and operation procedures. To oversee its design, implementation, and later its verification ARTS was designed according to the “V” model (Fig. 2). This model describes the flow of design, building and testing. Four main use

<sup>2</sup> At time of writing this mode, however, is not commissioned.

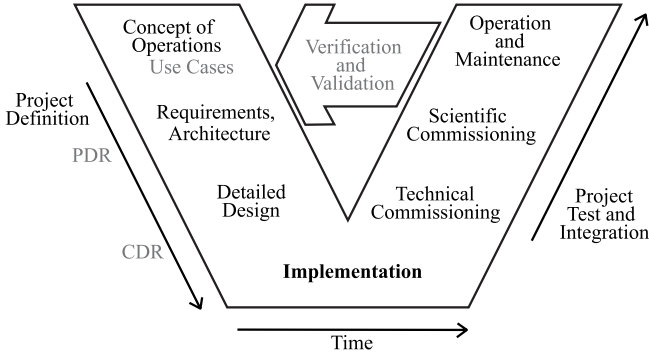


Fig. 2: System development V model mapped to ARTS.

cases (top-left; detailed, as science case SC 1.4, in [Straal 2018](#)) described the top-level sets of requirements for the system, for (1) Pulsar Timing, (2) VLBI, (3) Fast-transient searching commensal to imaging, and (4) Dedicated transient searching. These were numbered to reflect increasing complexity; their priority is the inverse, the dedicated search ranking highest.

These cases led to first, scientific requirements, and next, the derived technical requirements. Specific commissioning steps were defined that can test each requirement. Based on these, conceptual designs were drawn up, and together with demonstrator implementations these were reviewed in a Preliminary Design Review (PDR). Detailed designs were next reviewed in a Critical Design Review (CDR), and implemented. After technical and scientific commissioning (see, [Mikhailov 2018](#); [Straal 2018](#); [Oostrum 2020b](#), and Sect. 6), and revision where required, the system was brought into operation, including regular maintenance. At that point the system was functional; and that is the system we describe below.

#### 2.4. High level system overview

Time-domain observations with Apertif are defined by the science teams and scheduled by the observatory operators. Together, a number of subsystems (Sect. 2.4.1) form and process

an hierarchical series of beams (see Sect. 2.4.2). Transient detections in ARTS produce triggers to allow for follow-up in close to real time, and data products stored in the Apertif Long-Term Archive (ALTA), where they are publicly available.

##### 2.4.1. Three sets of subsystems

ARTS comprises the following major sets of subsystems. These work together as illustrated in Fig. 3.

The first subsystem set is the hardware platform (Sect. 3). It consists, first, of the dishes of the WSRT east-west interferometer and the Apertif PAFs. Front-end beamformers next provide dish processing. Tied-array beamformers built using FPGAs on high-performance processing boards (UniBoard and UniBoard<sup>2</sup>), are connected through fast networking to a GPU cluster.

The second set is the firmware and software sub systems (Sect. 4) that control and produce one or multiple TABs, or ‘pencil beams’. These can be in Nyquist sampled, complex-voltage format for pulsar timing (and VLBI). The data in these TABs can also be ‘detected’, i.e., converted to the four Stokes parameters, allowing subsequent partial integration to reduce data rates. That way, many hundreds of beams can be streamed out.

The third set of subsystems comprises the ARTS pipelines (Sect. 5). These perform transient searching and pulsar timing. For pulsar timing, the central single TAB is coherently dedispersed and folded in real time, on a single multi-GPU node. For the transient search, all Stokes-I TABs are cleaned of Radio Frequency Interference (RFI), dedispersed over a number of trial DMs, corrected for chromatic effects, and searched for transient events. Good candidates immediately trigger data dumps from a ring buffer of full Stokes-IQUV data. A deep learning implementation further classifies all candidates. Results and data are public to the outside world through VOEvents and the archive (Sect. 11).

##### 2.4.2. Hierarchical beam forming

One of the innovative aspects of ARTS is its use of hierarchical beamforming to allow for searches throughout the en-

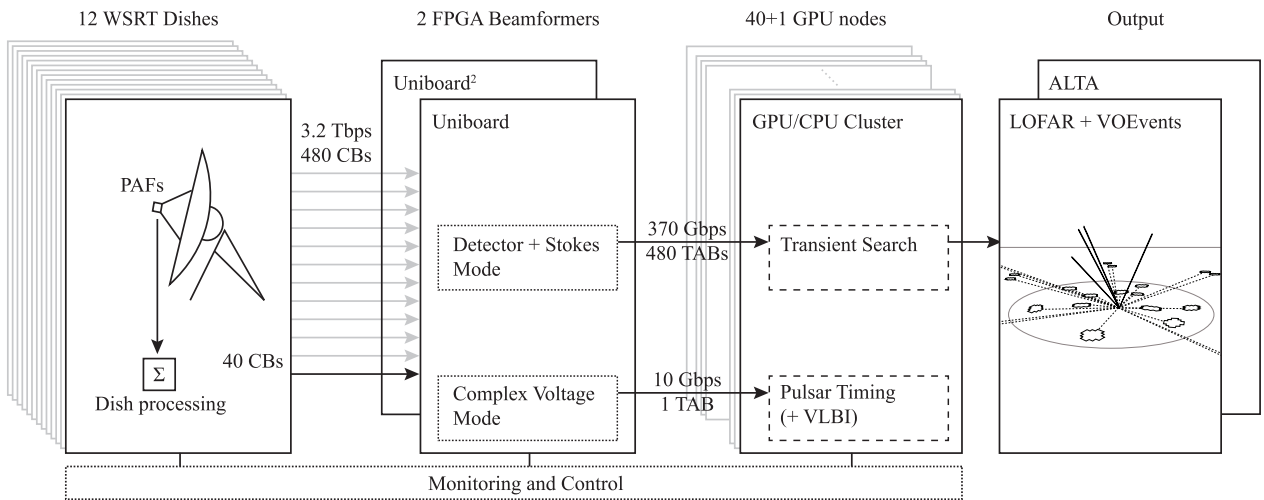


Fig. 3: Top-level diagram for ARTS. Different line styles indicate different types of subsystems, each described in their own Section. Full lines are hardware elements (Sect. 3). Dotted boxes depict firmware and software (Sect. 4). Dashed items are science pipelines (Sect. 5). The LOFAR and ALTA output are described in Section 11.

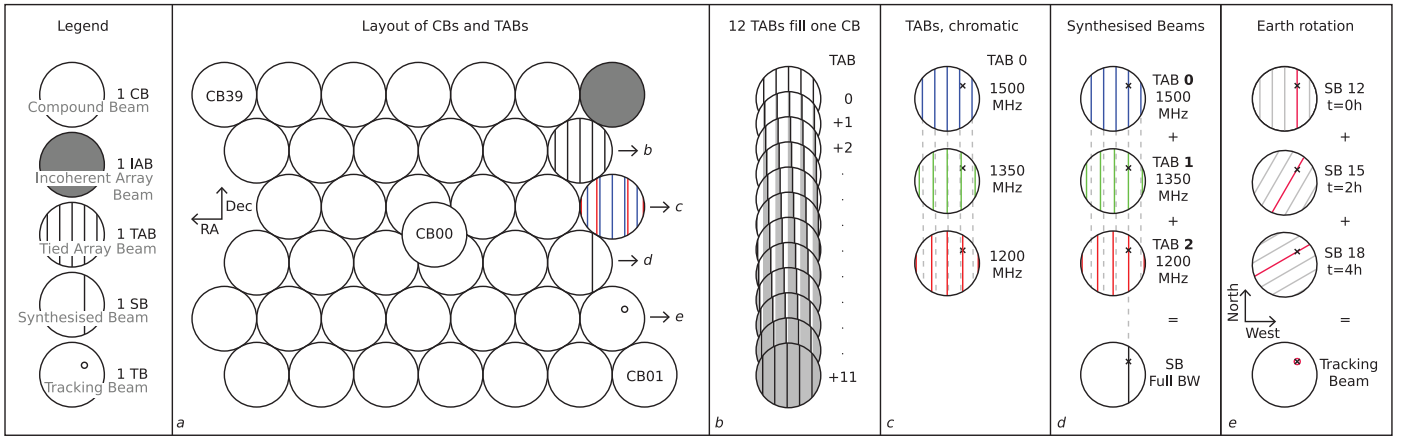


Fig. 4: An overview of the beam hierarchy in ARTS. Panel a) shows the 40 Compound Beams (CBs) formed by each PAF. The output signals of these CBs can be combined into Incoherent-Array Beams (IABs) or coherent TABs, whose grating responses fill the entire CB as shown in panel b). The frequency-dependence of these grating responses shown in panel c) can be exploited to disambiguate them by combining signals from multiple TABs to form a Synthesised Beam (SB) as illustrated in panel d). Finally, a Tracking Beam (TB) can be formed towards a specific locus within the CB combining multiple SBs over time as shown in panel e).

tire primary-beam FoV, at coherent-addition sensitivity. That is a challenge in many wide-field fast-transient instruments (for example the upcoming SKA; [Backer 2000](#), and LOFAR; [van Leeuwen & Stappers 2010](#)). We give a short conceptual overview of these beam forming steps here, because they are important in all subsystem sets. A more quantitative description is given in [Appendix D](#).

Figure 4 provides an overview of all constituents of the beamforming hierarchy. The base is formed by the 40 Compound Beams (CBs) formed by the PAF in each Apertif dish. Each CB has the same FoV as the primary dish beam, with a diameter of  $\sim 0.5^\circ$ , and produces a full-bandwidth, Nyquist sampled output data stream. Together, the CBs cover the FoV of the Apertif system as shown in [Fig. 4a](#).

The data streams of corresponding CBs of multiple dishes are combined using either an incoherent beamformer or a coherent beamformer. Using the incoherent beamformer, 40 Incoherent-Array Beams (IABs), one per CB, are formed that together cover the compound Field of View (FoV) of Apertif with a sensitivity improvement over a single dish that scales with the square root of the number of dishes used. When using *coherent* beamforming, the peak sensitivity scales linearly with the number of dishes involved, but more data streams need to be analysed as the FoV per TAB is smaller. For a regularly spaced 1-D array like WSRT, each TAB is not a single field: all sidelobes reach the same sensitivity as the central peak, and add to the TAB FoV. Together, 12 TABs now completely cover the FoV of their CB. This high TAB filling factor is illustrated in [Fig. 4b](#). It was first used by [Janssen et al. \(2009\)](#), to find new pulsars. Such full FoV beam forming requires that we only use those dishes that are spaced equidistantly. These are the 8 dishes RT2–RT9, plus the movable dishes RTA and B if they are located on the common baseline grid.

While we exploit the TAB grating to increase the TAB FoV, it also presents a degeneracy in the location of a detected event. We may not know through which grating sidelobe the signal is coming in. Fortunately the grating responses are frequency dependent – see [Fig. 4c](#). A source slightly further from the phase center than the specific grating response of a certain TAB at e.g. 1500 MHz, may fall exactly in the grating response of that TAB at 1200 MHz. Thus, most grating responses will detect a source

over limited frequency range. To make a detection over the full bandwidth the correct frequency-dependent TABs are combined to form a so-called Synthesised Beam (SB), as illustrated in [panel 4d](#). In ARTS, 71 SBs are formed in each CB. As it is integrated into the subband dedispersion ([Sect. 5.1.1](#)), this frequency re-organisation itself comes with no additional computational cost; but the increased number of beams (12 TABs to 71 SBs) do require more computing down stream. The SBs provide instantaneous localisation with a resolution determined by the array size in one direction, and the size of the CB in the other.

The orientation of the grating responses on the sky changes with time due to Earth rotation. A specific locus thus moves through different SBs ([Fig. 4e](#)). By combining the best positioned SBs in time, we form the last constituent of our hierarchy of beams: the TB. Over a 12-hour observation,  $\sim 3000$  unique loci form within each CB.

### 3. Description of Time Domain System: I. Hardware

A general description of Apertif is available in [van Cappellen et al. \(2022\)](#). In the next three sections we describe the time-domain capabilities. A number of subsystems in Apertif are shared between imaging, time-domain and VLBI modes. Where required for context, we provide high-level descriptions of these. This first section covers function and hardware. Further details on these are found in [Appendix A](#) and [B](#).

#### 3.1. Dishes in E-W Interferometer

The WSRT consists of fourteen 25-m dishes in a linear East-West array. It started operations in 1970 (for a recent overview see [Strom et al. 2018](#), marking the 50th anniversary of the array). The accuracy of the steel structure, the parabolic surface of the dish, and the size of the mesh, mean WSRT can be used up to  $\sim 8$  GHz. It was, however, designed for 21-cm wavelength observing. At the installation of Apertif the dishes too were refurbished and they operate as new. The mounts are equatorial. The 10 most western dishes, Radio Telescope (RT) 0–9, are fixed at redundant, 144 m intervals. RTA and B are immediately east of RT9, and can be moved on a rail track. RTC and D are on a track that is 1.3 km further east. Because of this dominant common



baseline, the instantaneous interferometric beam has highly sensitive sidelobes. This trait is exploited in ARTS (Sect. 2.4.2). The linear nature of the array demands that imaging uses Earth rotation to fill the  $u$ - $v$  plane. WSRT imaging pointings thus generally take 12 hrs.

### 3.2. Phased Array Feed (PAF)

Apertif includes PAFs (also known as focal plane arrays, FPAs) in 12 of the WSRT dishes, RT2-RTD. Each feed contains 121 receiver elements, 61 for X polarisation and 60 for Y polarisation, as opposed to the previous generation of receivers, the Multi Frequency Front Ends (MFFEs; cf. Tan 1991, Bregman et al. 2018), that were single pixel. The Vivaldi antenna elements in the PAFs are optimized for 1500 MHz. The elements also host the Low-Noise Amplifier (LNA), and are uncooled. The LNAs includes a filter that suppresses the strong RFI present below the nominal bottom of the Apertif band, at 1130 MHz. This does, however, contribute  $\sim 20$  K to the total system temperature of  $\sim 70$  K (van Cappellen et al. 2022). For the 12 dishes combined, and for the central, most sensitive CB, this produces an System-Equivalent Flux Density (SEFD) of  $\sim 45$  Jy at 0.75 aperture efficiency. For the 8 dishes generally used in ARTS, we find a median SEFD over all CBs of 85 Jy (Sect. 7.1).

### 3.3. Front-end digital processing

At the 12 dishes, the Apertif Front-End Beamformers (FEBFs; Sect. A.1) sample the Radio Frequency (RF) data from the PAF at 800 MHz. This yields a timing accuracy of 1.25 ns, at a total input data rate of 9.8 Tb/s. The sampled bandwidth is a contiguous 400 MHz band, tuneable between 1130–1720 MHz. The digitized data of all antenna elements is separated into 512 subbands, each 0.78125 MHz wide. At each dish, a rack of eight Uniboards (UNBs; Szomoru 2010), four per polarisation, beamforms the subband signals over the PAF elements, into so-called *beamlets*. Each FPGA in Uniboard (UNB) filterbanks and beamforms  $1/16^{\text{th}}$  of the subbands into CBs.

The CB pattern is laid out in a configuration that maximises even coverage over multiple, adjacent pointings (Hess et al. 2022). Initially Apertif was designed for 37 CBs (Oosterloo et al. 2009). Because the Apertif and ARTS hardware produce CBs in multiples of 8, the surveys now use 40.

Next, 384 out of the 512 subbands are selected for output, to achieve the final 300 MHz bandwidth. When expressed as 6-bit numbers, these fill the data transport capacity over the 384 links of 10 Gbps each, to the central building for correlation and/or tied-array beamforming. In total, the twelve Apertif-equipped dishes produce  $12 \times 40$  CBs. This data stream (called CB480) contains 3.5 Tb/s of compound-beam data (Sect. A.1, B.1; and Table A.1).

### 3.4. The ARTS Tied-Array Beamformer (TABF) and Apertif Correlator (X) subsystems

The Apertif Correlator (“X”) and ARTS TABF both use the same Apertif FEBF CB480 data. In Fig. 5 we show how these subsystems relate. The transpose  $T_{\text{array}} = T_{\text{dish}} + T_{\text{pol}}$  groups the data from all  $N_{\text{tp}} = N_{\text{pol}} \times N_{\text{dish}} = 24$  single polarization telescope paths (TP) in the WSRT array. The Apertif X creates visibilities by cross correlating the compound beams between all dish pairs. The ARTS TABF creates array beams by summing compound beams over the dishes. These array beams can be coher-

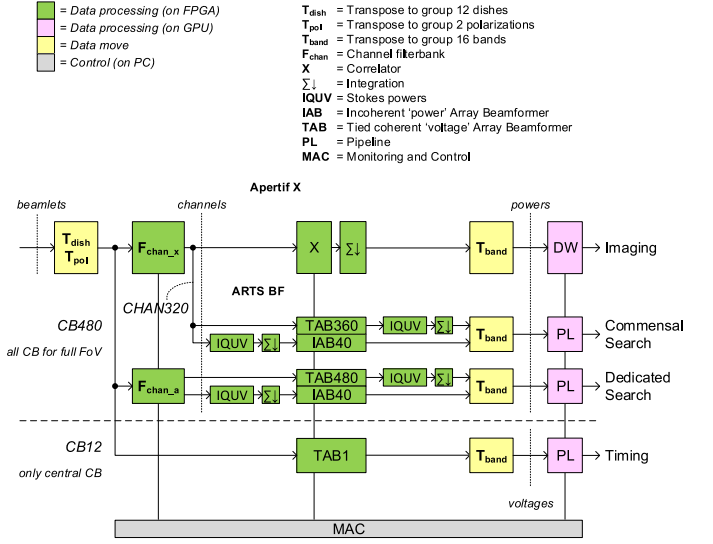


Fig. 5: The ARTS TABF subsystem and the Apertif X subsystem.

ent TABs or IABs, for either voltage, power or full Stokes power data (Eq. A.1, Sect. A.3, A.4).

### 3.5. The ARTS Tied-Array Beamformer (TABF)

The function of the TABF is to create the IAB and TAB data, and to transpose the data for the Arts Pipeline processing (PL; Sect. 5). For the search data the TABF also functions to reduce data rates, by integrating in time.

For searching, the ARTS TABF first separates the beamlets into 64 subchannels, using a similar filterbank ( $F_{\text{chan},x}$  in Fig. 5) as Apertif X. The search modes use all 40 CBs. The TABF can combine all 12 dishes (480 CBs) but in practice only includes dishes that are equidistant in the array configuration at the time. The output of the  $IQUV$  data is integrated over 16 subchannels to achieve the required  $81.92 \mu\text{s}$  time and 195 kHz frequency resolution (Sect. A.2). The standard TABF output are integrated full Stokes  $IQUV$  array power beams, 480 for dedicated search and 360 for commensal search. Optionally, IABs can be produced. In that case the order of beamforming and detection are switched.

For timing-mode (and VLBI) output, the FEBF transposing is bypassed (see Sect. A.1 and Fig. A.2) and the beamlets are used directly. The central CB is voltage beam-formed into a single TAB (TAB1 in Fig. 5).

An important requirement on the central beam forming hardware, identified in the design process (Sect. 2.3), is the handling of the large amount of input links, and the high data rate of  $\sim 3.5$  Tb/s, produced by the Apertif dish processing (Sect. 3.3). The relatively low number of operations per bit required led to the implementation of the tied-array beamformers on FPGAs.

In dedicated ARTS mode, the time-domain survey determines the baselines and the pointing of the WSRT dishes. In commensal mode (Sect. 2.2.3), the Apertif imaging science case is in control, and the correlator runs. Therefore the dedicated search (and timing) run *instead* of Apertif X, and can then use the same 16 UniBoards used by the correlator, as detailed in the next subsection.

The ARTS commensal transient search runs at the same time as the Apertif X. Firmware for both does not fit together on 16 UniBoards. The commensal search thus needs to run on a sepa-

rate set of FPGA boards. Four Uniboard<sup>2</sup>s (UNB2s) can provide the required Input/Output (I/O) and compute in a setup described in Sect. 3.7.

Fig. 6 shows how the ARTS FPGA beamformer maps on Uniboard and UNB2, and how the boards are interconnected.

### 3.6. Dedicated ARTS TABF on Central Uniboards

The central ARTS beamformer consists of 16 UNBs with a total of 128 FPGAs (for details, see Appendix B.2). Each UNB processes  $1/16^{\text{th}}$  of the bandwidth (i.e., 18.75 MHz) of all dishes. Each FPGA receives the X or Y data from three dishes within that band. For the dedicated FRB survey, the data are reordered such that each FPGA processes the data from five CBs.

The UNBs are equipped with Optical-Electrical Boards (OEBs; Sect. B.2) to handle the demanding I/O. All 384 10-GE ports are required for data that comes in. For X, outgoing data can fit on the 1 Gbps ports because the time integration strongly reduce the data rate. But for the TABF the complete usage of the links by the input is a challenge. The ARTS dedicated search makes 12 TABs/CB that also require 128 10-GE links, for transport and transpose of the data to the PL. For all 384 ports, the Rx and Tx are thus physically split. The UNBs receive Apertif FEBF data over Rx and send beam formed data over Tx to the PL.

The data processing in both the Apertif FEBF and the ARTS TABF Uniboards is clocked at 200 MHz. All are locked to the same 10 MHz reference as the Analogue-to-Digital Converters (ADCs) sample clock (Sect. B.1) such the processing rate in all FPGAs is held fixed relative to each other.

During dedicated FRB survey observations, the Uniboards generate 480 TABs with a time resolution of 81.92  $\mu$ s and 1536 frequency channels over a bandwidth of 300 MHz. For each TAB, both a Stokes I and a Stokes-IQV data stream are created, for a total output data rate of  $\sim 360$  Gb/s.

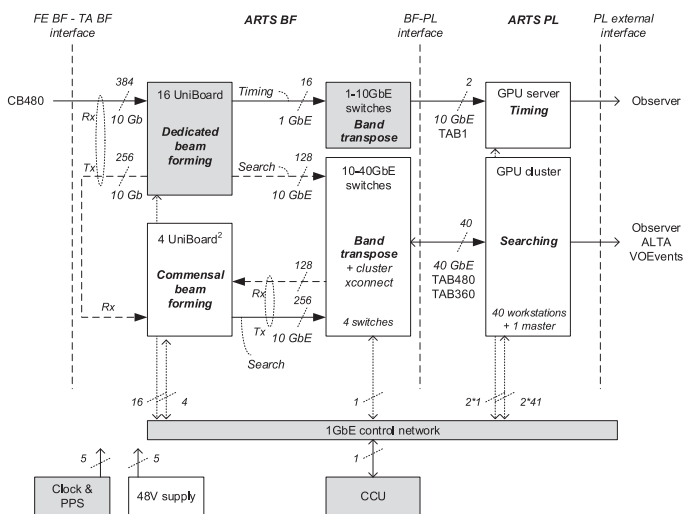


Fig. 6: The mapping of the ARTS system on the UNBs, UNB2s, switch, and CPU/GPU cluster hardware. The dashed Tx links are unidirectional links. The dashed Rx links are full duplex links that are combined with the UNB2 Tx links.

### 3.7. Commensal ARTS TABF on Central Uniboard<sup>2</sup>s

In the central building, a set of four UNB2s (Schoonderbeek et al. 2019) is also installed, to be able to run imaging and time-domain at the same time. That commensal search uses 8 dishes as input and requires making 9 TABs/CB. Four UNB2s each with four Arria10 FPGAs (see Sect. A.5) can create these beams, but then a channel filterbank does not also fit. Therefore the TABF for commensal search uses the output from the channel filterbank in the Apertif X, that will then be running on the UNBs. The filterbank in the Apertif X correlator already makes 64 channels, the same as the dedicated search. The Uniboard<sup>2</sup>s receive the CHAN320 data (8 dishes  $\times$  40 CBs) from the 16 UNBs, as visualized in Fig. 5 and detailed in Appendix B.3.

### 3.8. Networking and interconnect

The central UNBs receive the CB480 input from the Apertif FEBF (Fig. 6) over the 384 10G Rx links (Sect. 3.6). The 10G Tx part of these same links is used to offload the output TAB data, or to pass on data to the 4 UNB2s. For the dedicated search 360 Gbps (Table A.1) of TAB power data is carried via 128 10G links. Each UNBs or UNB2 beam forms all telescopes and CBs but only for part of the bandwidth of these TAB power data. For searching, these data need to be transposed such that all bands for a single set of TABs converge in a single PL GPU node (Fig. 7). In the data network, this band transpose function  $T_{\text{band}}$  is implemented using Commercial Of The Shelf (COTS) 10/40 GbE switches (called the transposer in Fig. 6 and in Sect. B.5). Initial designs required a custom transposer, but the switches were able to handle the uni-directional links produced by UNB and UNB2 (see Sect. B.5).

In commensal-search mode, the UNBs operate as correlator, and only pass on the CHAN320 data to the UNB2s. One third necessarily passes through the same 128 10G connections mentioned above, and goes through the switches, as indicated by the dashed links Fig. 6. The other two thirds is directly passed on from UniBoard via 256 10G links. The UNB2 output of 270 Gbps is transposed and sent to the PL. This is a factor 9/12 less than for dedicated search, because commensal mode has 9 TABs.

For timing, the modest data rate of 9.6 Gbps (2 pols  $\times$  300 MHz  $\times$  2 complex  $\times$  8 bit; Table A.1) is carried via 16 1GbE links.

### 3.9. ARTS GPU cluster

Data for pulsar timing is coherently dedispersed and folded by a single GPU-accelerated server (“ARTS-0”). This machine contains 2 CPUs with 6 physical cores each, 2 Titan-X GPUs, 2 10GE Networks Interface Cards, and 18 HD slots with 16 active disks in a JBOD configuration.

Data for searching is much higher volume, and is processed by a 41-node GPU cluster. Each node has identical hardware, which is listed in Table 1. One node serves as master/login node; it does not receive any data from the beamformer. The other 40 nodes provide a total of 160 GPUs, 1600 CPU cores, 5 TB RAM, and  $\sim 1.3$  PB storage, for a theoretical peak performance of  $\sim 2$  PFLOP/s.

Each of the 40 worker nodes processes the data from one compound beam. That way cross detections can immediately be compared between TABs in a CB; and tracking beams made. The incoming data rates per CB are 1.8 Gbps of Stokes I data, and 7.2 Gbps of Stokes IQUV data. Half of the storage is available for the incoming Stokes I data, which when writing continuously

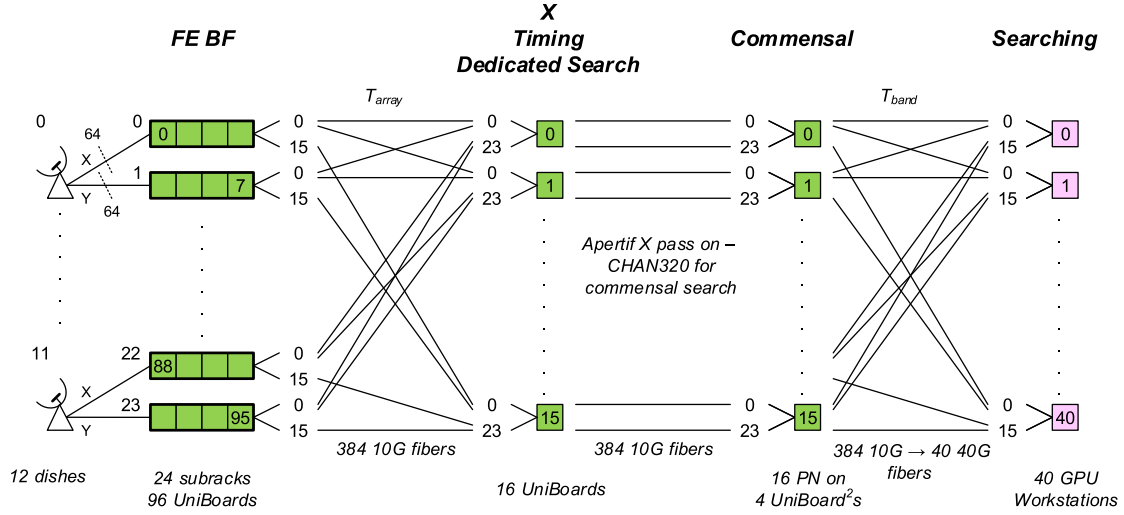


Fig. 7: The interconnectivity in the Apertif data streams. Data moves from left to right, through the Apertif Front-End Beamformer, Correlator, ARTS Tied-Array Beamformers, and Pipeline processing on the GPU nodes.

Table 1: Hardware overview of a GPU cluster node. The cluster consists of 41 nodes with identical hardware.

CPU	2 × Intel Xeon E5-2640 v4 (40 cores total)
GPU	4 × Nvidia 1080 Ti
RAM	128 GB
Network	40 Gbps, full-duplex
Storage	32 TB in 2 independent hardware RAID0

fills up in ~20 hrs. Hence any processing that requires access to these data should take at most a few hours to run.

Transient data buffers were initially designed to reside on the UNBs. The GPU cluster, however, could hold more DDR3 memory more economically, with simpler transient-dump control functions. Thus, the Arts BF now outputs full Stokes IQUV (for dumping), instead of only the Stokes I data (for searching). This Stokes IQUV data is only stored upon a trigger from the transient pipeline, so even though the Stokes IQUV data rate is four times that of Stokes I, its storage will fill up very slowly.

Both Stokes I and IQUV data are buffered in RAM, for 10 and 15 s, respectively, and made available to the datawriters and pipelines. Over the system, these buffer about 1 TB of data for triggering.

### 3.10. Housing

ARTS is located in an RF-shielded High Frequency cabin in the central building of WSRT. The cabin contains coolers with air-water heat exchangers. This water is pumped through an outside chiller, that operates passively when possible, and only uses compressors when required. In the cabin, three cabinets house the UNBs and switch equipment. These are air cooled through the cabin ambient cooling. The ARTS GPU servers and UNB2s are distributed over 6 racks in a single row. Three large dedicated reverse coolers create a cold and hot isle. Cold air flows through the servers to the hot isle. The CPUs and GPUs are cooled against this air. The FPGAs on UNB2 are liquid cooled, and exchange heat with the air flow outside the UNB2 box. When operational, the total ARTS system uses 50 kW of power.

### 3.11. Control

Through the control network, ARTS and Apertif are directed by a Central Control Unit (CCU) computer that connects to the TABF and the PL via Ethernet. The CCU is synchronized with the atomic clock of the WSRT using the standard network time protocol (NTP).

## 4. Description of Time Domain System: II. Firmware and Software

### 4.1. Firmware

In the following subsections we describe how the ARTS TABFs in Fig. 3 are implemented in Hardware Description Language (HDL) firmware on the FPGAs on UNB and UNB2 (Sect. 3.6, 3.7). More detail is available in Appendix C.1.

Each operating mode has a dedicated FPGA application design that either runs on all 128 FPGAs of the TABF UNBs or on all 16 FPGAs of UNB2. The designs contain functions for the TABF itself, for monitoring during operation, and for testing during commissioning. Switching between modes occurs by changing the design image. The flash memory of UniBoard and UniBoard2 typically contains a default image and an application image. Changing application requires reprogramming the flash. There are three different FPGA images for the 16 UNBs: search, timing and correlation. The 4 UNB2 can run two images: the commensal search and the dedicated-search pass through.

The voltage beamformer function is at the heart of the TABF system. A coherent beamformer weights and sums the input voltages from the input dishes. For the single voltage TAB (for timing or VLBI), the VHDL component from the subband CB beamformer in the Apertif FEBF (van Cappellen et al. 2022) was directly reused. The multi-beam TABF function for surveying contains further parameters that define the increased number of weights. This TABF operates per CB and thus provides the voltage TAB480 and voltage TAB360 functionality.

The subchannel filterbank and integrator functions are weaved into one. This reduces aliasing losses. On the one hand, samples should be integrated in time to 81.92  $\mu$ s to reduce data rate. On the other hand, the fine channel Polyphase Filter Bank (PFB: called  $F_{\text{chan}_a}$  in Fig. 5) for search mode needs to separate



Article number, page 11 of 40

detailed in van Cappellen et al. (2022) and Appendix C.2; the ARTS software in Oostrum (2020b).

#### 4.2.1. Monitoring And Control (MAC)

The Apertif MAC (Loose 2016, and Sect. C.2) comprises relatively independent software components that communicate through a message bus (cf. Sect. C.2.2). As in LOFAR, we use a Qpid bus. The MAC next contains three software layers: drivers, controllers and orchestration (Sect. C.2.3). The first contains the drivers for all hardware components. These handle all I/O to all hardware components. The second contains the high level controllers. These each cover one specific system function such as control of a dish, the correlator, or the beamformer. Each controller typically interacts with several drivers. All basic, shared functions of these controllers are implemented through a controller framework (cf. Sect. C.2.5). The orchestration layer sets different components through the entire system.

#### 4.2.2. Apertif Task DataBase (ATDB)

The Apertif Task DataBase (ATDB; Vermaas et al. 2019) is the workflow that guides Apertif observations from specification to safe delivery into ALTA. ATDB is implemented as a microservices architecture, where a central database contains just enough information about the observation to guide it through the workflow. The database is wrapped inside a Django web application and can be accessed by a range of (Python) ATDB services through a ReSTful API. The workflow is mostly automated, but offers a GUI for testing. Each of the ATDB services has a specific task. They are triggered by a specific observation status, and after performing their task leave the observation in different status. Together, this orchestra of services forms a very flexible, adaptable and lightweight workflow.

#### 4.2.3. ARTS Drivers and Controllers

For the ARTS TABF, a driver uploads the TAB static weights during system setup. Other parts of the system are set up when an observation is started by ATDB sending a parameter-set file (*parset*, as used in LOFAR; Stappers et al. 2011) over the Qpid messaging bus. Two controllers direct the ARTS GPU cluster (see, Fig. C.4 and Oostrum 2020b). ARTSSURVEYCONTROL, on the master node, receives the parset with commands and parameters. These include the CBs that need to be recorded. For each of these, pointing and processing settings are sent to the ARTSSURVEYNODECONTROL controllers running on worker nodes.

Processing on the nodes, as overseen by ARTSSURVEYNODECONTROL, revolves around the data memory buffers. Following ARTS predecessor PuMa-II (Karuppusamy et al. 2008), these buffers use PSRDADA<sup>3</sup> formats and tools. Four buffers are created: two for Stokes-I and two for Stokes-IQUV data; per set, the main buffer continuously holds all incoming data, while the trigger buffer uses *data\_dbevent* to store a selected amount when an external trigger is received. Stokes-IQUV triggered data is written to disk using *dada\_dbdisk*. Multiple processes read from the main Stokes-I buffer. First, ARTSSURVEYNODECONTROL starts three instances of GPU search pipeline AMBER (Sect. 5.1.1) across three GPUs. Then, it starts two data writers: *dadafilterbank* (for high-resolution filterbank files), and *dadafits* (for archive resolution FITS files). Two instances of *fill\_ringbuffer* fill the main Stokes I and IQUV buffers from

the network. Finally, ARTSSURVEYNODECONTROL starts ARTS processing pipeline DARC (Sect. 5.1.2).

When an observation finishes, each instance of ARTSSURVEYNODECONTROL reports back to ATDB which FITS data products were generated for long-term archiving in ALTA.

#### 4.2.4. ARTAMIS

The dish position, the subband statistics in the form of auto correlation powers, the power in the LNAs, the operational firmware image, and the Local Control Unit (LCU) data are monitored through the All-Round Telescope Array Monitoring and Information System (ARTAMIS; Schoenmakers et al. 2019). This real-time monitoring system of the entire WSRT is based on ETM/Siemens WinCC-OA. That same framework monitors LOFAR. Data is acquired through custom-built interfaces using a WinCC-OA C++ API, and through Simple Network Management Protocol (SNMP). Data is available to all users through a web interface. Adjustable alarms alert the telescope operators, and allow investigations into specific subsystems. The WSRT operators have an instantaneous view on the whole system on a single screen, with color codings for alarm tracking and follow-up. Trend graphs of datapoints versus time aid with diagnosing alarm root causes or understanding data quality issues. Custom data displays cater to specific users and use cases.

#### 4.2.5. ALTA

The Apertif Long-Term Archive (ALTA<sup>4</sup>; Holties et al. 2019) provides the long-term storage for raw and processed Apertif data. It covers data management, discovery, and access. The system combines 2 PB online disk-based storage, a PostgreSQL database server, and a web-based user portal (all hosted at ASTRON), with tape-based scalable data storage hosted at SURFsara. The online storage provides low latency access to user-selected data products, and caches tape-based data.

Rule-based data management for this tiered and distributed storage environment is provided through iRODS<sup>5</sup>. It enables high performance access, through a single namespace. Like all raw and processed data, the ARTS filterbank files are ingested using a PIP-installable client package. Ingests are transaction based and part of automated workflows. Metadata is parsed into the ALTA data-model schema, and incorporated into the its database. This supports full data provenance, and is compliant with Virtual Observatory (VO) standards. A web interface is provided by a ReactJS frontend and a full REST API backend built on Django. Public data is exposed through a WEBDAV interface, on an NGINX webserver.

For public users, the primary entry point to access these ALTA data is through the ASTRON Virtual Observatory services (Sect. 11.2). There, data collections including the one described in this paper are published.

## 5. Description of Time Domain System: III. Science Pipelines

### 5.1. FRB Searching

Searching for FRBs is an inherently computational process. This Section presents the different parts of the ARTS search pipeline.

<sup>4</sup> <https://alta.astron.nl>

<sup>5</sup> <https://irods.org>

<sup>3</sup> <http://psrdada.sourceforge.net/> (van Straten et al. 2021)

### 5.1.1. AMBER

The Apertif Monitor for Bursts Encountered in Real-Time (AMBER; Sclocco et al. 2016) is the real-time software pipeline for single pulse detection used within ARTS. The goal of AMBER is to identify FRB candidates, i.e. dedispersed signals with high signal-to-noise ratio, from the beamformed data stream described in Section 4.1.1. AMBER is optimized for execution on highly parallel architectures, such as the GPUs installed on the ARTS cluster. AMBER is implemented in C++, with the GPU kernels implemented in OpenCL.

One of the key points in the design of AMBER is modularity. Each component of the pipeline is a separate module, and is developed and maintained on its own. This design allows developers to work on new modules, or make changes to existing ones, with minimal impact on the AMBER code base. Moreover, modules can be reused in other projects such as SKA without requiring a hard dependency on AMBER.

The standard pipeline is composed by seven processing stages sequentially applied to data chunks: (1) Radio Frequency Interference (RFI) mitigation, (2) downsampling, (3) dedispersion, (4) integration, (5) signal-to-noise evaluation, (6) candidates selection, and (7) clustering. Among these seven stages, four are optional and can be enabled by the user when starting AMBER, while the others are always executed. We briefly describe each stage below.

**RFI mitigation (optional).** Two distinct filters are applied to the input data to identify and remove – in real time – any bright wide-band low-DM RFI and bright narrowband RFI, respectively; this module is described in more detail in Sclocco et al. (2019).

**Downsampling (optional).** This module reduces the time resolution of the input data. Downsampling data is particularly useful when searching for transients at high DM. There, very high time resolution is not required as the intra-channel smearing of high-DM candidates is already larger than the original sampling time. At high DM steps, AMBER also requires longer-duration chunks of data, which can be prohibitive due to memory limitations of the hardware.

**Dedispersion.** This module constitutes the base for the searching algorithm. It implements dedispersion using an algorithm derived from the brute force approach. Recognising that, in GPU dedispersion, optimizing for memory limitations is more fruitful than for compute bounds, the module is highly tuned for data reuse. It can dedisperse in both a single step, or using a more efficient two step process including subbanding. During subbanding, the module creates the SBs described in Sect. 2.4.2, as illustrated in Fig. 9. A further overview of the module design and performance is available in Sclocco et al. (2016).

**Integration (optional).** FRBs pulses span a range of time durations. The Signal-to-Noise ratio (S/N) is highest if the time series are down sampled such that all emission is collected in a single time bin. We thus search over a range of down sampling factors. During integration, the dedispersed time series are downsampled in the time dimension according to this user-defined discrete set of trial pulse widths. This integration thus acts as a convolution kernel that smooths the signal and approaches the maximum intrinsic S/N of transients of various pulse widths.

**S/N evaluation.** This module provides a way to compute the S/N of all peaks in the dedispersed, and optionally integrated,

time series. Different ways of computing the S/N of a time series are implemented in this module, and users can select the method that best fits their data.

**Candidates selection.** Candidates with S/N higher than a user-defined threshold are stored and made ready to be included in the output.

**Clustering (optional).** At this stage, selected candidates with similar DM or pulse width are clustered together, thereby reducing the total number of candidates reported in the output. Each cluster is represented by the candidate with the highest S/N.

Eventually, all candidates found in the current input chunk are stored in a text file, and after the output is saved, AMBER continues processing the next chunk of input data.

AMBER is distributed under version 2.0 of the Apache License, and the source code is available on GitHub<sup>6</sup>. Source code portability, i.e. the ability to compile and run AMBER on different hardware platforms, is provided by using standardised and open languages such as C++ and OpenCL. However, AMBER is not just portable at the source code level: as a result of the combination of run-time code generation, user configurability, and auto-tuning, AMBER can also provide performance portability, and can be automatically adapted to achieve high-performance on different hardware platforms (see e.g. Mikhailov & Sclocco 2018), and for different observational parameters and searching strategies.

### 5.1.2. DARC

In real time, AMBER delivers metadata of FRB candidates. Based on these, the decision whether to store the Stokes-IQUV data buffer to disk, and/or trigger a LOFAR observation is taken in the DARC<sup>7</sup> pipeline (the Data Analysis of Real-time Candidates; Oostrum 2021c). DARC also orchestrates the automated *offline* processing of the best FRB candidates by the deep neural network (Sect. 5.1.3). A detailed description of DARC is available in Oostrum (2020b).

**Global design** To ease development and improve readability, DARC, too, is split into several modules (Table 2). These fall in three categories: monitoring and control, offline processing, and real-time processing. Real-time processing is only active for the current observation, while offline processing may be running for several observations simultaneously. An overview of the DARC modules and how DARC connects to the ARTS MAC (Sect. 4.2.3) is given in Fig. C.4.

**Monitoring and control** Each node of the ARTS GPU cluster (Sect. 3.9) runs an instance of DARC. The DARCMASTER module receives the control signals from the ARTS MAC (Sect. 4.2.3) and manages all other DARC modules. On the master node, the STATUSWEBSITE module monitors the nodes, for a local status web page.

**Real-time analysis** When an observation starts, DARC runs real-time processing for that observation. Every second, the AMBERLISTENER module reads in the candidates from each AMBER instance. Each candidate has a beam number, down-sampling factor, arrival time, width, DM, and S/N. A single transient may be detected in multiple points in this 6-dimensional pa-

<sup>6</sup> <https://github.com/TRASAL/AMBER>

<sup>7</sup> <https://www.github.com/loostrum/darc>; Apache-2.0 License



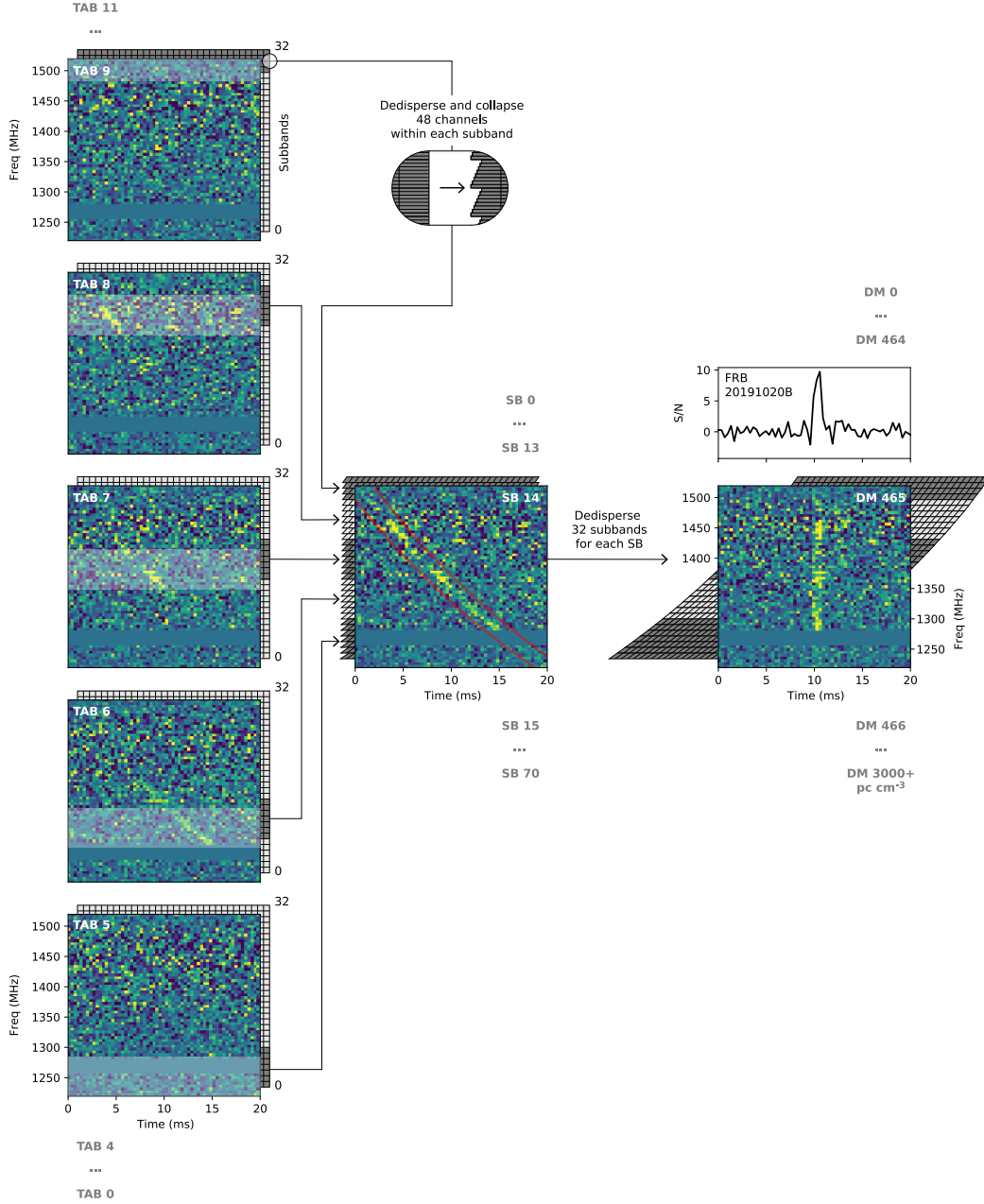


Fig. 9: The formation of the SBs during subband dedispersion demonstrated through the detection of FRB 20191020B. Combinations of 12 TABs (left column) produce 71 SBs. The TABs are combined in units of subbands, each consisting of 48 channels. Each subband is first dedispersed to a coarse DM. For SB 14 the resulting intermediate time-frequency plot is shown in the center. We show this step here for clarity but in the production implementation it is optimized out. For ease of visibility the FRB is shown here at a DM that is reduced by a factor 20. In the second step of dedispersion, the subbands are aligned over 32 trial DMs. FRB 20191020B was thus detected as shown on the right.

parameter space. AMBER already clusters candidates that are close in time, DM, and downsampling factor. The AMBERCLUSTERING module clusters the candidates further over the DM/arrival time plane, and across all SBs of the CB.

If the resulting highest S/N event exceeds either the known or new-source threshold (Table 3), the next pipeline step, DADATRIGGER, initiates an IQUV dump and/or LOFAR TBB trigger.

The length of the IQUV dump equals the dispersion delay across the band with a minimum of 2 s, plus an extra empty 2 s to determine noise statistics. The start and end time are rounded down and up, respectively, to the incoming data cadence of

1.024 s chunks. Overlapping IQUV triggers are merged into one, eliminating dead time there; but disk-pool writing speeds limit triggers to one per minute.

The LOFARTRIGGER module on the master node collects the worker-node inputs, representing all CBs, and selects the highest S/N trigger to be sent to LOFAR. The VOEVENTGENERATOR module can next format and send an xml VOEvent to the broker, for triggers to the outside world (Sect. 11.1).

**Offline analysis** After recording finishes, the offline processing is automatically started. OFFLINEPROCESSING performs a deeper

Table 2: DARC modules and tasks, see also Fig. C.4.

Module	Task
<i>Monitoring and control:</i>	
DARCMaster	Manages all other modules
STATUSWebsite	Generates a web page with the status of each module
<i>Offline:</i>	
OFFLINEPROCESSING	Full offline processing pipeline
<i>Real-time:</i>	
AMBERLISTENER	Reads AMBER candidates from disk
AMBERCLUSTERING	Determines for which candidates to trigger a Stokes-IQUV dump and/or LOFAR TBB observation
DADATRIGGER	Executes Stokes-IQUV triggers through PSRDADA
LOFARTRIGGER	Executes LOFAR triggers
VOEVENTGENERATOR	Sends VOEvents to outside world

search for FRB candidates, and informs the team of the results via email. The module also takes care of system verification and calibration. This processing typically runs while the next observation is being analysed in real time.

Using the same method as the real-time system, the offline processing now clusters all candidates from the observation at the same time. Any candidates with a  $DM < 20 \text{ pc cm}^{-3}$  or  $S/N < 10$  are discarded. For all remaining candidates, data from the TAB filterbank files are converted into the required SB data using the DARC multi-threaded SBGENERATOR tool, and cleaned of RFI. We then dedisperse to the DM found by AMBER and downsample in time to the pulse width that maximises the S/N of the frequency-averaged time stream. That refines the initial, real-time AMBER S/N estimate, which was based on only 1.024 s of signal and noise. This re-calculation is especially important for wide pulses, detected at the highest downsampling factor of 250. Offline, the method consists of a matched filter that tries many different box-car widths. For all candidates with post-processing  $S/N > 5$ , the dynamic spectra, DM-time arrays, and metadata are saved to an HDF5 file, as input for the machine learning classifier (Sect. 5.1.3).

The resulting candidate plots from this classifier, together with overall statistics, are e-mailed to the astronomer team and made available on a local website for human vetting and follow-up decision making.

In addition to FRB analysis, the OFFLINEPROCESSING module folds test pulsar data with PREPFOLD from PRESTO<sup>8</sup> (Ransom 2011). It also automatically processes drift scan data, which are used for sensitivity measurements (Sect. 7.1).

### 5.1.3. Machine Learning Classifier

Due to the real-time nature of the ARTS pipeline and the large number of false-positives relative to true astrophysical transients, our candidate classification had to be automated. To this end, we built a binary classifier using deep neural networks (DNN) to select true FRBs and discard false positives generated by RFI and noise fluctuations (Connor & van Leeuwen 2018). The publicly-available package is called `single_pulse_ml`<sup>9</sup> and uses Keras

(Chollet et al. 2015) with a TensorFlow (Abadi et al. 2015) backend for the construction, training, and execution of its convolutional neural networks (Connor 2018). Our machine learning classifier was trained on tens of thousands of false positive triggers from Apertif, as well as an equal number of ‘true positives’ that were generated either by injecting simulated FRBs into real telescope data or by detecting single pulses from Galactic pulsars.

Raw FRB candidates from AMBER are clustered in time, DM, and pulse width and sent to the classifier which then assigns a probability of it being a real astrophysical transient. If the probability is above a set threshold (currently 50%), a diagnostic plot is generated showing the frequency-time intensity array (i.e. dynamic spectrum), DM-time intensity array, and the pulse profile, as well as metadata such as the beam number, S/N, classifier probability, and width.

### 5.1.4. Localisation method

To localise FRBs we make use of the multi-beam information provided by our setup. We create a model of the telescope response on a grid spanned by RA and Dec, and compare this to the measured S/N.

The beam model is constructed from the hierarchical beam-forming techniques described in Sect. 2.4.2 and Appendix D, and is detailed in Oostrum (2020b). First, we create a model of the CBs, based on drift-scan data from both imaging and time-domain drift-scan data. The performance of this model is described in Sect. 7.2. For each CB, we then simulate the tied-array beamformer followed by the construction of the TABs and SBs. This final beam model predicts the relative sensitivity of the different SBs (see Sect. 7.3).

To localise a burst, we next compare its detection footprint against this model. We determine the detection S/N of all SBs covering the CB the burst was found in, and of all neighbouring CBs. A beam model is next generated on a  $40' \times 40'$  grid with a resolution of  $2''$ , centred on the highest-S/N CB. The predicted relative S/Ns over all SBs are then compared to the measured S/Ns, through a  $\chi^2$  method. The final 90% confidence localisation region is then derived from the  $\Delta\chi^2$  values. As the region is generally close to elliptical, we often refer to it below as an ellipse. The most likely localisation position is generally on the semi-major axis, but often away from the center. The localisation precision is evaluated in Sect. 7.4.

### 5.2. Pulsar Timing

ARTS can process a single tied-array beam (Sect. 4.1.3), to perform pulsar timing and to carry out general pulsar studies. During such an observation, the complex sampled voltages are processed in real-time on a dedicated server (Sect. 3.9). This machine, ARTS-0, has two classes of operation: a recording mode and a timing mode. In recording mode, the incoming TAB1 data is written to disk in PSRDADA format (van Straten et al. 2021). For timing, ARTS-0 predicts the pulsar periods and phases for the duration of the observation using tempo2 (Hobbs et al. 2006; Hobbs & Edwards 2012). Using these predictions, 16 instances of dspsr fold and coherently dedisperse the data that come in through the input ringbuffers (see Appendix C.3.1 for details). Each dspsr instance processes a 18.75 MHz subband containing 24 channels of 0.781250 MHz (as produced by the FEBF, Sect. 3.3). The 16 instances are divided over 2 GPUs, which allows the system to reduce data in real time. Subintegrations of

<sup>8</sup> <https://www.github.com/scottansom/presto>

<sup>9</sup> [https://github.com/liamconnor/single\\_pulse\\_ml](https://github.com/liamconnor/single_pulse_ml)

Table 3: Thresholds used during candidate clustering. LOFAR triggering is disabled for known pulsars.

Trigger type	Source type	S/N <sub>min</sub>	DM range (pc cm <sup>-3</sup> )	Downsampling <sub>max</sub>
Stokes IQUV	Known pulsar	10	DM <sub>src</sub> ± 10	-
	Known FRB	10	DM <sub>src</sub> ± 10	-
	New source	10	> 1.2×DM <sub>YMW16</sub>	100
LOFAR	Known FRB	12	DM <sub>src</sub> ± 10	-
	New source	12	> 2.0×DM <sub>YMW16</sub>	80

the resulting folded profiles are stored in a PSRCHIVE (Hotan et al. 2004) format filterbank file every 10 seconds.

## 6. Commissioning results

### 6.1. Pulsar detections

During commissioning, we regularly observed the four pulsars B0329+54, B0531+21, B0950+08, and B1933+16. Single pulses were detectable from each. The integrated profile of a 5-minute observation of each test pulsar is shown in Fig. 10. As detailed in Oostrum (2020b), we used the S/N of these detections and the radiometer equation to produce first, rough estimates of the System-Equivalent Flux Density (SEFD) of the 8-dish system used for these observations. Scintillation and intrinsic brightness variations affect this measurement. Furthermore, the Crab Nebula is not resolved out completely by the TAB on PSR B0531+21, so its emission increases the derived SEFD. The median of the four derived SEFD values is 200 Jy. PSR B1933+16 is the most stable pulsar in the set, and the SEFD its observations suggest (130 Jy) is expected to be the most accurate.

Assuming an aperture efficiency of 70%, a system temperature of 70 K (Oosterloo et al. 2009; van Cappellen et al. 2022), and perfectly coherent beamforming, the theoretical SEFD of eight Apertif dishes is expected to be ~70 Jy. The values derived here are a factor 2-3 higher. Fluctuations in pulsar brightness on that level are not unexpected. A more accurate SEFD can be derived using scans of calibrator sources, as discussed in Sect. 7.1.

### 6.2. Coherence of the Tied-Array Beams

Observing with an interferometric array is most profitable when full beam-forming coherence is obtained. Then, the attained TAB sensitivity evolves linearly with the number of dishes used. For incoherent addition, on the other hand, the IAB evolution follows a square-root law. We measured the efficacy of our telescope addition by observing pulsar B1933+16 over about two dozen telescope combinations (for details, see Straal 2018), and comparing the resulting pulsar S/N between the two modes, after scaling for bandwidth and integration time. The values and resulting dependence are shown in Fig. 11. The sensitivity increase is in good agreement with the expected relation  $S/N \propto \sqrt{n_{\text{dish}}}$  for the IAB, and  $S/N \propto n_{\text{dish}}$  for the TAB, demonstrating the coherence of the multidish beam-forming system.

### 6.3. Timing stability

Early commissioning flagged that the synchronisation of the time stamps (the BSN, Block Sequence Number, Sect. C.1.1) to the Pulse Per Second (PPS) signal did not occur completely

as expected when the ADCs (Analogue-to-Digital Converters; Sect. B.1) were power cycled. Such power cycling (“cold starts”) severely reduced the effectiveness of the CB calibration solution, as the time and phase information of the CBs jumped. Avoiding power cycling during firmware switches (“warm starts”) was found to keep calibration valid, and produce a system at adequate sensitivity and stability for surveys.

Such timestamp jumps, however, are expected to have a deleterious effect on pulsar timing with Apertif (Sect. 5.2). Especially for long-term timing, intermediate system power cycling cannot be avoided. We thus observed a set of precisely timed millisecond pulsars that are part of the European Pulsar Timing Array (Kramer & Champion 2013), over multiple, monthly epochs, with intervening power cycling. We compare the folded Apertif observations of pulsars such as B1855+09, B1937+21 and J1713+0747 against their ephemeris. We find phase offsets that vary between epochs, of over 1 ms in magnitude. This shows the system indeed does not naturally preserve absolute time when power cycled, and does not support a long-term timing program in its current operational state.

In multiple observations taken of PSR J1022+1001 without power cycling in between, the pulse phase does line up to within a ~1 μs. Short-term timing thus is phase coherent.

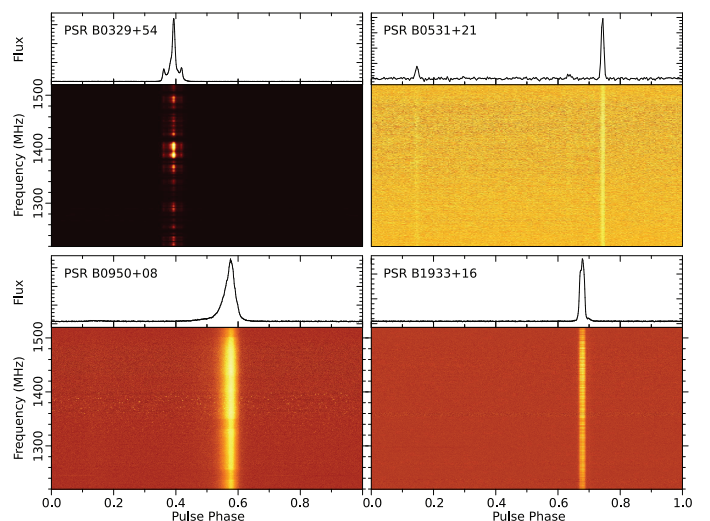


Fig. 10: Integrated profiles and dedispersed frequency-phase diagrams of each test pulsar that is regularly observed with ARTS. These were generated from 5-minute observations.



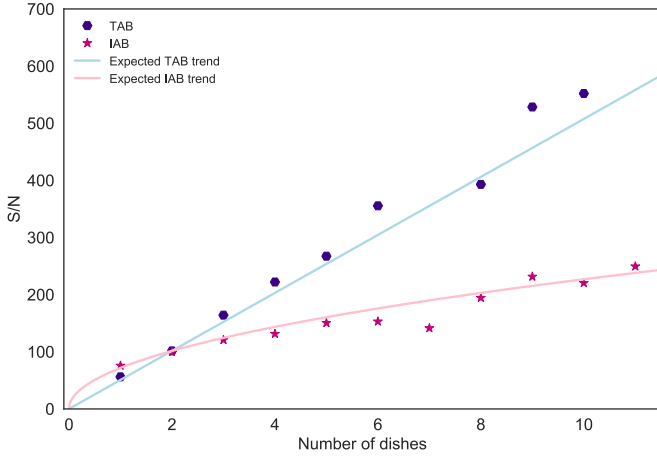


Fig. 11: Signal-to-Noise ratio of PSR B1933+16 versus number of dishes, for coherent and incoherent addition. The two trends are scaled to intersect the 2-dish S/N value.

#### 6.4. Perytons

For testing the telescope sensitivity, pulsars (Sect. 6.1) and quasars (Sect. 7.1) were reliable commissioning sources. To specifically test the ARTS real-time transient detection system we used perytons. Perytons are a type of RFI first discovered at Parkes (Petroff et al. 2015b), generated when microwave-oven doors are opened when the cavity magnetron still operates. The frequency structure of the interference is very similar to the sweep seen for high-dispersion measure sources, which is quite unique for terrestrial RFI. During the Apertif Science Verification Campaign (SVC; Sect. 11.3) we emitted 8 perytons using 2 different ovens, from outside the WSRT control building. AMBER detected the perytons in real time at a DM of nearly  $400 \text{ pc cm}^{-3}$  (Fig. 12).

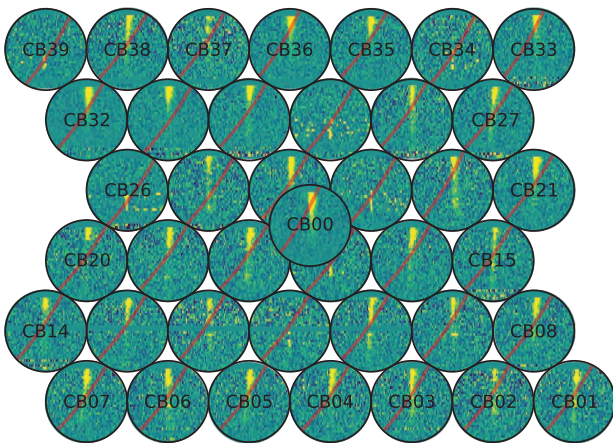


Fig. 12: The peryton was detected in all 40 compound beams (the circles). In each, the respective time-frequency plot is displayed (similar to, e.g., the bottom panel of Fig. 32), dedispersed to  $395 \text{ pc cm}^{-3}$ . The vertical axis spans 300 MHz of bandwidth, the horizontal axis 500 ms of time. The red curve indicates the track a signal with  $\text{DM} = 0 \text{ pc cm}^{-3}$  would have followed.

## 7. Performance

### 7.1. Compound-beam Sensitivity

The ARTS sensitivity depends on the sensitivity the individual CBs and on the calibration accuracy of the delay and phase offset between the dishes. Following this weekly calibration, we use quasars 3C48, 3C147, or 3C286 (Perley & Butler 2017) to determine the sensitivity of the CBs, following the drift-scan method (Oostrum 2020b) summarised below.

For each TAB of each CB, we compare the on-source and off-source values to determine the SEFD from

$$\frac{\text{on} - \text{off}}{\text{off}} = \frac{S_{\text{calibrator}}}{\text{SEFD}}, \quad (1)$$

where  $S_{\text{calibrator}}$  is the calibrator flux density. Fig. 13 shows the derived SEFD for all 480 TABs, on seven different days. The reported SEFDs are the median values in the frequency band not affected by strong RFI. The TAB sensitivity within a CB is relatively constant. The CBs themselves vary, most likely due to variations in the weekly calibration, which can be affected by RFI or the calibrator hour angle.

The sensitivity of a CB is also expected to depend on its position within the PAF, with central elements illuminated best. In Fig. 14 we show the median SEFD of each CB against its offset from the PAF centre. The six outlier points with an  $\text{SEFD} > 120 \text{ Jy}$  are the six CBs at the end of each PAF row. We also see the general, expected trend: beyond  $\sim 1^\circ$  from the PAF centre, the SEFD increases, by  $\sim 30\%$  for the outermost beams (trend confirmed independently in Fig. 38 of van Cappellen et al. 2022). Overall, the median SEFD of the system is  $85 \text{ Jy}$ .

### 7.2. Field of View

Based on the beamforming models described in Sect. 2.4.2 and Appendix D, we determine the theoretical CB sensitivity pattern. The position of each CB is defined as an offset relative to the pointing centre. As the WSRT dishes have equatorial mounts, the CB pattern does not rotate on the sky and the offsets do not change over time in the (RA, Dec) frame. However, because the PAF lies in a plane – the focal plane of the parabolic dishes – the CB offsets do not directly map to offsets in (RA, Dec). Instead, the planar CB offsets have to be projected onto the spherical (RA, Dec) coordinates. This transformation is equivalent to the tangent, or Gnomonic, projection (Oostrum 2020b).

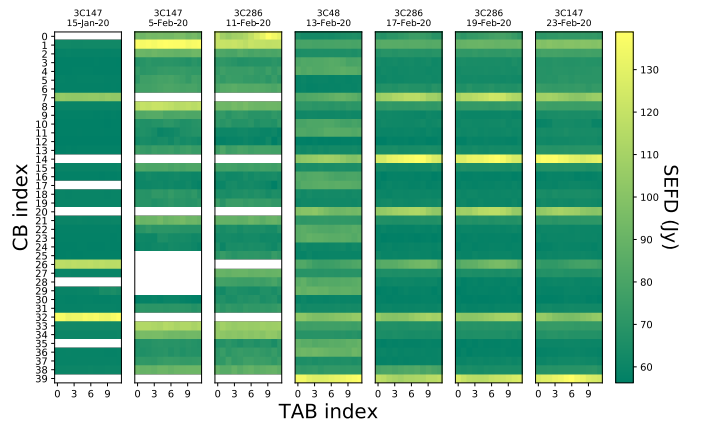


Fig. 13: SEFD for all TABs of all CBs on seven different days. White regions indicate absence of data. Above each figure, the calibrator source and date are indicated.

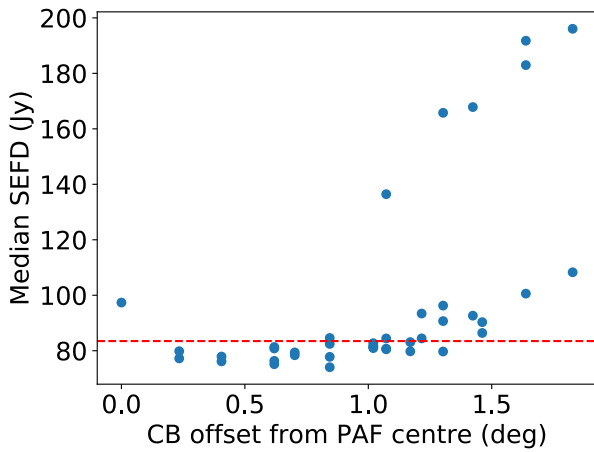


Fig. 14: Median CB SEFD as function of distance to the PAF centre. The red line indicates the overall median sensitivity.

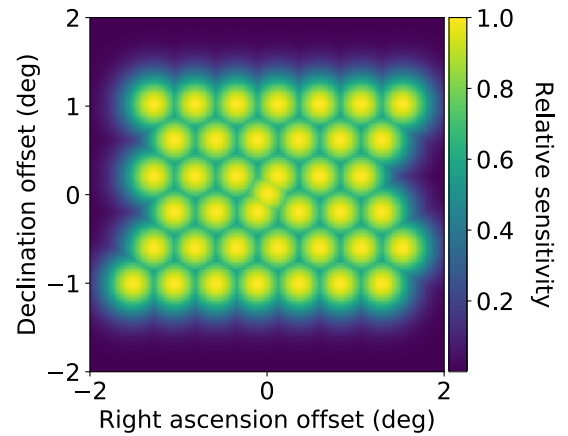
The resulting theoretical model at 1370 MHz of the 40 CBs is as shown in Fig. 15a. This simulation is idealised as it assumes each CB reaches the same peak sensitivity. In reality, both the sensitivity and shape of the CBs depend on their position within the PAF, and change over time as the system is recalibrated weekly (Sect. 7.1). Using drift scans in the image plane, the shape of the CBs was measured in June 2019 (Dénes et al. 2022; Kutkin et al. 2022). As long as none of the main PAF elements contributing to a CB fail, the shape of the CBs should remain fairly constant. A 2D Gaussian was then fit to each CB averaged over all dishes. The size of the CBs is assumed to scale linearly with wavelength.

To account for temporal variations in sensitivity (generally caused by RFI during calibration), a more accurate model is constructed for each observing session with an FRB detection. For those session models, the peak sensitivity of each CB is taken from the time-domain drift scan that is nearest in time. As dish-to-dish sensitivity variations are lost during the tied-array beamforming, we implicitly work on the assumption that each dish has the same sensitivity pattern. Combining the CB sensitivities, shapes, and positions thus leads to a model to the CB sensitivity at each (RA, Dec) point on the localisation grid. The November 2019 model, for example, is shown as Fig. 15b.

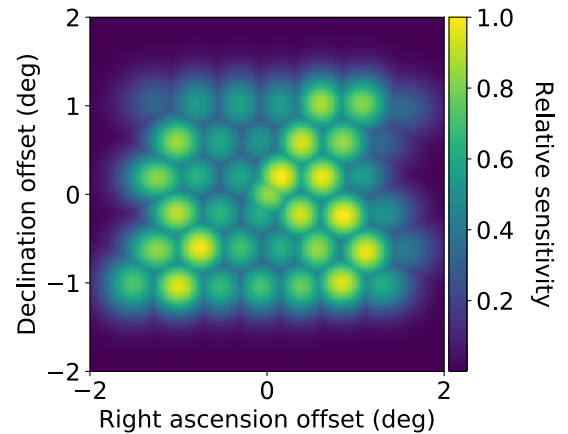
From these models, we calculate the general Apertif FoV, out to the half-power contour. This results in a FoV of 8.2 sq. deg. at 1370 MHz. We note that the FoV of a single CB is  $\sim 0.3$  sq. deg. at 1370 MHz, so Apertif increased the WSRT FoV by a factor  $\sim 30$ . At higher frequencies, the relative FoV increase is even higher.

### 7.3. Tied-array beamforming performance

Within the FoV spanned by the CBs, we next construct the TABs and SBs (Sect. 2.4.2), to find the relative sensitivity of the different SBs. We simulate the ARTS beamformer (Sect. 3.5), recreating its pointing through the application of the geometric phase offset of the CB centre plus the additional TAB offsets (as detailed in Oostrum 2020b). We take the projected baseline length and orientation into account. Because we only use the equidistant dishes in the WSRT array, the resulting TAB grating response has infinitely many sidelobes at the same sensitivity as the main beam. However, this pattern is attenuated by the CB responses seen in Fig. 15.



(a) Ideal beam model.



(b) Fitted beam model, 2019 Nov.

Fig. 15: Model of the 40 CBs of Apertif at 1370 MHz using (a) rotationally symmetric Gaussian beams with equal peak sensitivity and (b) 2D Gaussian fits to each beam, scaled to their measured peak sensitivity in November 2019.

We finally simulate the mapping of the TABs to SBs. For each of 32 subbands we choose most sensitive TAB given the required pointing of the SB (following Appendix D). All SBs have a narrow main beam and several sidelobes. Only the main beam contains signal of the full frequency range, whereas the sidelobes do not. This is best illustrated for a beam on the edge of the CB, as shown in Fig. 16. For a main beam response, see e.g. Fig. 23.

Based on the drift scans of the calibrator quasars through the TABs of each CB (Sect. 7.1), we can determine the TAB beamforming efficiency we achieve. The system temperature of Apertif is  $\sim 70$  K (Oosterloo et al. 2009; van Cappellen et al. 2022). At 1400 MHz, the sky background contributes minimally to the measured noise level. Combining the measured SEFD of 85 Jy of the CB plus TAB system with the aperture efficiency of 75% reported in van Cappellen et al. (2022) leads to a beamforming efficiency  $\beta$  of 0.8. The deviation from 1.0 is likely the result of RFI, especially through its effects on the weekly CB calibration.

### 7.4. Localisation Accuracy

To validate the the accuracy of the localisation described in Sect. 5.1.4, we observed a field that includes both the Crab pulsar (PSR B0531+21) and PSR B0525+21. An example of the local-

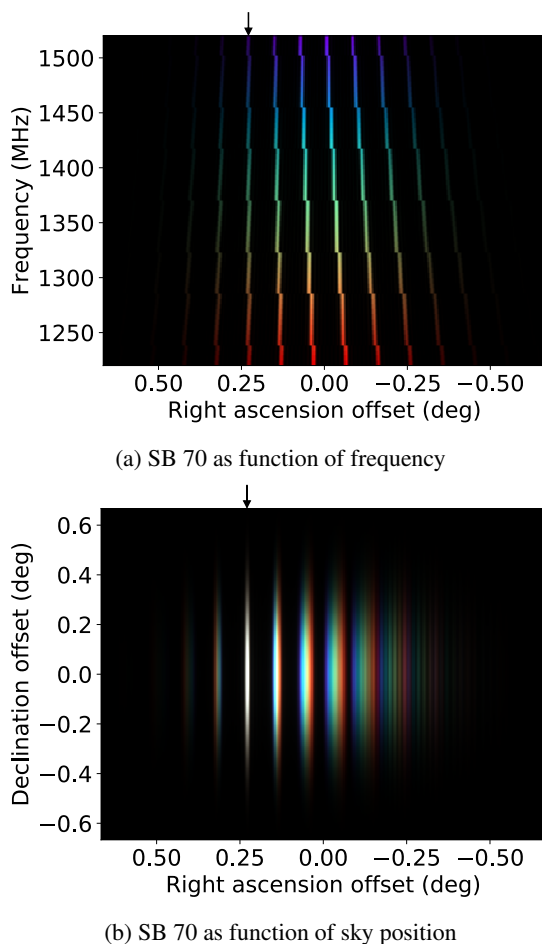


Fig. 16: Model of outermost Synthesized Beam 70. In (a), as a function of RA and frequency. The intended main beam is indicated with an arrow. The discontinuities in the sidelobes occur when the beamforming switches to a different TAB. In (b), as a function of RA and Dec. The colours indicate frequency, where white means an SB is sensitive over the full frequency range. Only the main beam in (b) is broadband, the sidelobes are not.

isation of the Crab pulsar, based on the non-/detection footprint over the CBs and TABs of a single pulse, is shown in Fig. 17. The real position of the pulsar falls within the final 90% localisation region. As the likeliness is quite flat over this region, the fact that the source is away from the center of the region does not signify any systematic offsets. Similar validation on PSR B0525+21 corroborates this outcome (Oostrum 2020b).

For sources that repeat, multiple burst at different hour angles next intersect to further pinpoint the source (Sect. 2.2.1, Fig. 4). Two or three bursts generally suffice. In Fig. 18 we demonstrate how the independent localisation of three separate bursts of FRB 20180916B (Pastor-Marazuela et al. 2021) combines to a final 90%-confidence-level localisation area of  $26''$  by  $9''$ , in which the true position is contained.

## 7.5. RFI Identification and Mitigation

WSRT is located in a radio-quiet zone and its RFI environment is good overall. A number of known RFI sources remain, however (as listed in Oostrum 2020b). These are generally stronger than astrophysical signals and can cause false-positive detections (i.e. non-astrophysical pulses erroneously classified as FRBs).

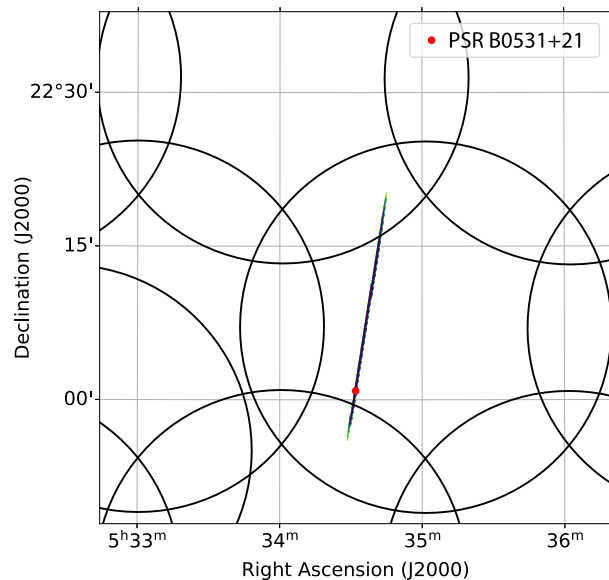


Fig. 17: Localisation of the Crab pulsar using a single pulse. The black circles indicate the size of the CBs at 1370 MHz. The true location falls well within the 90% confidence ellipse that is displayed.

False-positive detections have a direct effect on the search pipeline, as they can rapidly increase the size of the single-pulse candidates list, which in turn requires more processing, in addition to the need for visual verification by astronomers. To reduce the impact of RFI on our pipeline, two mitigation strategies are currently used in ARTS: on-line RFI removal using local statistics (Sect. 5.1.1 and Sclocco et al. 2019), and an off-line deep-learning classifier (Sect. 5.1.3).

### 7.5.1. Direction dependence of RFI

We assessed the variability of RFI against sky direction in the AMBER results of 448 observations taken March-Sept 2019, when online RFI mitigation was not implemented yet in AMBER. Any trigger with  $DM=0$  and  $S/N>10$  was assumed to be RFI.

The heatmap of the resulting RFI trigger rate as function of azimuth and altitude is shown in Fig. 19. A peak at  $az=260^\circ$  and  $alt=65^\circ$  stands out from the otherwise uniform RFI distribu-

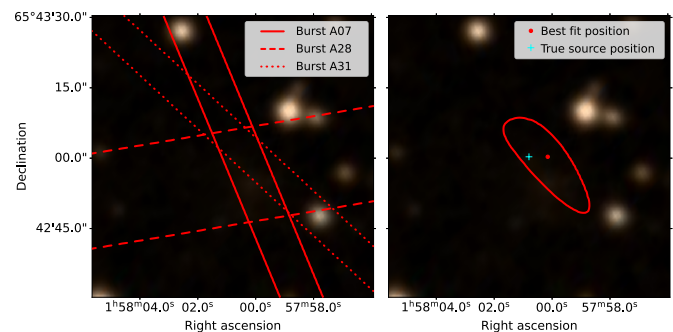


Fig. 18: Localisation of FRB 20180916B from three individual bursts. Left: a zoom-in on the overlap of the localisation regions for bursts A07, A28 and A31 (labels as in Pastor-Marazuela et al. 2021). Right: the combined, final localisation region.



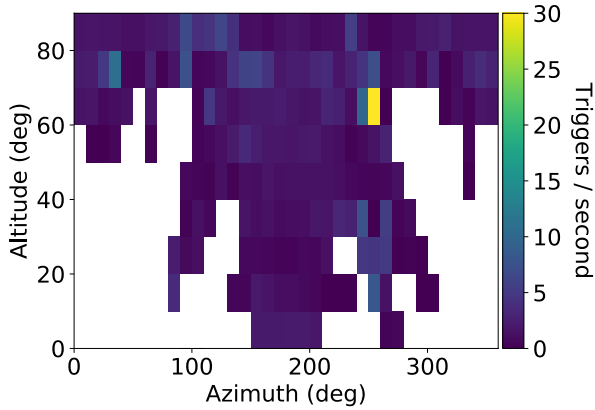


Fig. 19: Number of RFI triggers per second against direction. The strong RFI near  $(az, alt) = (260^\circ, 65^\circ)$  is due to the Smilde radio mast.

tion on the sky. The Smilde radio mast is located at this azimuth and its UHF antenna transmits in the Apertif frequency band. We likely observe a reflection on the troposphere. Mast emission that is reflected once, halfway between Smilde and WSRT, at a typical troposphere height of 17 km, is expected at an apparent altitude is  $68^\circ$ , which matches our observations.

#### 7.5.2. Fraction of data lost to RFI

The on-line RFI mitigation in AMBER (Sect. 5.1.1) employs two methods: Mitigation in time domain targets bright low-DM broad-band signals, while the frequency-domain method removes spurious narrowband RFI. Both methods are applied in an iterative manner, where each consecutive step applies mitigation to an ever-cleaner set of samples. Three iterations of each method are applied. We evaluated the overall impact of RFI on our time and frequency samples, in a representative 3-hour observation. We find that at most about 7% of the total bandwidth is affected by RFI for limited time periods ( $< 0.5$  hr). In general, less than 3% of data is lost to RFI. Fig. 20 highlights that the majority of RFI sources in our band consist of spurious narrowband emission.

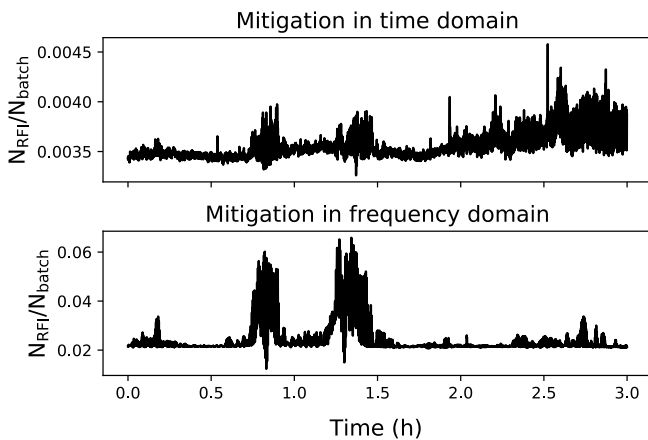


Fig. 20: Fraction of samples cleaned of RFI by the two mitigation strategies, throughout a standard 3-hour observing session.

#### 7.6. Observing efficiency

The end-to-end observing efficiency of our system can be determined by the fraction of time for which valid data reaches the archive (Sect. 11.2). Dead computing nodes and pipeline failures would prevent that outcome. This number is a lower limit to our observing efficiency for discoveries though, as those detections happen in real time. These can and have occurred when, for example, network issues prevented archiving, while real-time processing continued. For 2019, the archive efficiency was  $\sim 90\%$ , for 2020 it was 94%.

#### 7.7. Pipeline

The ARTS single-pulse search pipeline includes AMBER's dedispersion engine with simple clustering, a DM/time clustering algorithm to group islands of triggers in that space, and the aforementioned machine learning classifier. Throughout commissioning, each step in the pipeline was tested via simulated FRB injection tests and single-pulse observations of Galactic pulsars. For our simulated bursts, we used the injection package `injectfrb`<sup>10</sup> as well as evaluation code for assessing completeness<sup>11</sup>. We find that in the relevant search parameter space (Sect. 8.3), the pipeline is over 90% complete.

#### 7.8. Computing performance

The largest fraction of the computing requirements for ARTS is taken up by the FRB search. On each of the 40 nodes, 3 GPUs (Sect. 4.2.3) run AMBER to carry out this search. These three instances search the low, medium, and high DMs independently. Fig. 21 shows the amount of time spent in each AMBER function (Sect. 5.1.1) for a three-hour observation. After the very effective optimisation of, first, the dedispersion kernel (Sclocco et al. 2016), and next, the S/N kernel, input handling and integration (downsampling) are the steps that take most of the execution time in the production pipeline.

Due to the low arithmetic intensity, the dedispersion kernel and most other functions are memory bound. Performance is thus best understood by comparing our throughput against the theoretical memory bandwidth of the 1080 Ti of 484 GB/s. The AMBER instances processing low and medium DMs achieve a real-life throughput of almost 1 TB/s each. That throughput, averaged over all kernels, exceeds the theoretical memory bandwidth because the dedispersion kernel so effectively exploits data re-use, through cache access optimization. The instance processing high DMs achieves a throughput of 0.5 TB/s. This performance makes it possible to process observations in real time.

### 8. Survey and observation strategy

ARTS enables an all sky survey for FRBs and pulsars to pursue the science goals outlined in Sect. 2. This survey, ALERT, the Apertif-LOFAR Exploration of the Radio Transient sky, is described below. Its first results are presented in the next Section.

#### 8.1. Frequency coverage

ALERT uses a central frequency (cf. Sect. A.2) of 1370 MHz to avoid the RFI present at lower frequencies. This differs from the Apertif imaging-survey frequency settings. These are lower,

<sup>10</sup> <https://github.com/liamconnor/injectfrb>

<sup>11</sup> <https://github.com/EYRA-Benchmark/frb-benchmark>

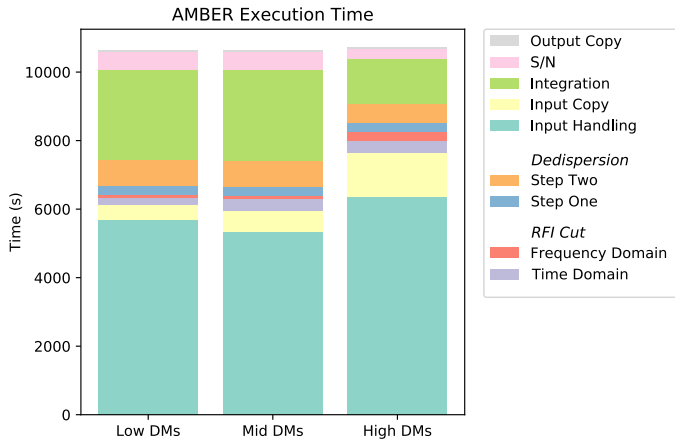


Fig. 21: The break down of the functions for the three AMBER instances that run on each CB/compute node. Shown are the various total execution times per function, that together ran real-time on the 3 hr observation.

centered on 1280 MHz, such that redshifted HI is observable throughout a larger cosmic volume.

### 8.2. Pointings and scheduling

In the 2019 Apertif schedule, time domain observations were allotted a 1/3rd share of the science time. These generally occurred as 2-week blocks every 6 weeks. Pointing definition followed the same field pattern used for the imaging surveys (Hess et al. 2022). To provide a relatively uniform coverage of the Northern sky in the planned survey time, we limit ourselves to pointings with declination  $>10^\circ$ ; and to maximize the number of FRB detections we avoid the increased foreground dispersion in fields closer to the Galactic Plane than  $5^\circ$ .

The pointing selection was guided by our triple aims of detecting, localizing, and characterizing FRBs. We thus target fields that a) produced earlier ALERT, detections, such that in follow-up we can determine if or how these repeat, or b) contain known repeater FRBs such that these can be better localized and/or studied, or c) are blank, to search for new FRBs. In the known-source fields (a) and (b), new detections were expected at the same rate as in blank fields, which indeed we found to be the case (Sect. 9). Blank fields are scheduled using Apersched<sup>12</sup> (Hess et al. 2022). Each pointing lasts 3 hr. Generally, preference is given to fields at hour angles close to zenith to minimize terrestrial RFI, which is more prevalent near the horizon.

### 8.3. Search parameter space

The survey is optimally sensitive to FRBs characterized by certain sets of parameters. Sources outside this space may still be detectable, but generally at reduced S/N. Our dedispersion plan (Table 4) starts at  $0 \text{ pc cm}^{-3}$ . Sources with DM below  $100 \text{ pc cm}^{-3}$  (similar to e.g., FRB 20200120E; Bhardwaj et al. 2021), however, may easily be misidentified as RFI in the human vetting, as they show little dispersion sweep over our 1.2–1.5 GHz band. That is especially the case for wide bursts. So for these low-DM bursts, and for bursts above our maximum DM of  $\sim 3400 \text{ pc cm}^{-3}$ , ALERT is not complete.

<sup>12</sup> <https://github.com/kmhess/apersched>

Table 4: The dedispersion setup for ALERT. The three GPUs cover subsequent parts of DM-trial parameter space. Each uses two-step subband dedispersion (Sect. 5.1.1) with 32 subbands and has optimal dispersion settings.

GPU	DM range ( $\text{pc cm}^{-3}$ )	DM step ( $\text{pc cm}^{-3}$ )	Subbanding DM step ( $\text{pc cm}^{-3}$ )
1	0–409.6	0.2	6.4
2	409.6–819.2	0.2	6.4
3	819.2–3379.2	2.5	40.0

AMBER searches through the incoming data at native time resolution of  $81.92 \mu\text{s}$ , and at resolutions downsampled by factors 5, 10, 25, 50, 100 and 250. Any bursts narrower than the original time samples, or wider than the last step, equaling 20 ms, will only be detected at reduced S/N.

## 9. First results

We here present the first set of ARTS results, based on observations up to 2019 Dec 31. We discovered five new FRBs, a significant addition to the  $\sim 100$  published at the time (see Petroff et al. 2016), most of which are only very roughly localised. The cut-off date is aligned with the adjustment of the Apertif time-domain survey strategy at the start of every calendar year. Results from following years will appear in the very near future (e.g. Pastor-Marazuela et al. 2022b). A summary of the observed and derived properties of the 2019 FRBs is given in Table 5. It lists both the FRB\_19MMDD format names that we used in earlier publications (Connor et al. 2020; Oostrum et al. 2020), and the TNS-network designations for these bursts, in FRB\_2019MMDD[A–Z] format (Yaron et al. 2020), that we use in this paper. In the following subsections, we discuss the characteristics and localisation of each FRB separately. Where required we describe analysis methods where they are used for the first time. The analysis of the ensemble is presented in Sect. 10.

### 9.1. FRB 20190709A

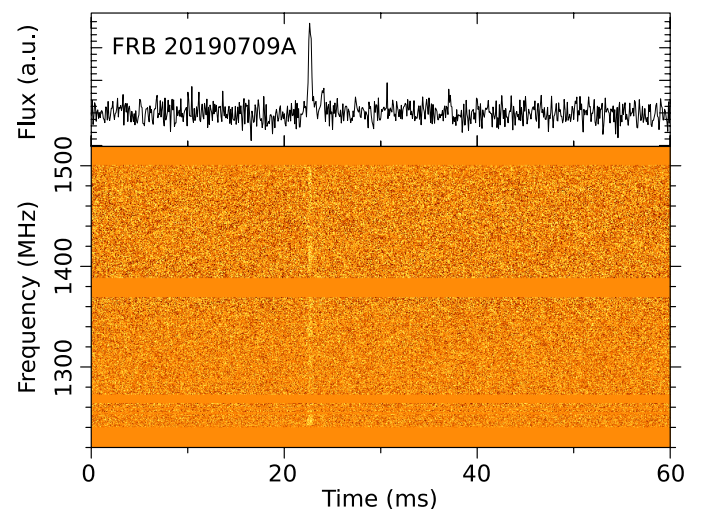


Fig. 22: Dynamic spectrum (bottom) and pulse profile (top; flux density scale in relative, arbitrary units) of FRB 20190709A.

Table 5: The ALERT FRBs up to 2019 Dec 31. First column lists TNS name, second lists previously used name (cf. [Oostrum et al. 2020](#); [Connor et al. 2020](#); [Oostrum 2020b](#)). MJD refers to the arrival time at the solar system barycentre at infinite frequency. DMs and widths were measured with pdmp from PSRCHIVE ([Hotan et al. 2004](#)). DM<sub>MW</sub> are the Milky Way DMs predicted using the NE2001 ([Cordes & Lazio 2002](#)) and YMW16 ([Yao et al. 2017](#)) models, respectively. We assume a 10% uncertainty on the observed pulse widths and 20% on the derived fluences. The position error regions are strongly elongated and presented individually. The best position is not always at the center of the elliptical region. The derivation of the redshift upper limit  $z_{\max}$  is described in Sect. 10.4.

FRB	Internal name	MJD	S/N	DM (pc cm <sup>-3</sup> )	DM <sub>MW</sub> (pc cm <sup>-3</sup> )	$z_{\max}$	Width (ms)	Fluence (Jy ms)	RA (J2000)	Dec (J2000)
20190709A	190709	58673.21792057	26	663.1±0.1	52 / 45	0.65	0.49±0.05	7.0±1.4	01:39:19s	+32:03:13
	190903*	58729.02228880	8	664±10	53 / 46	0.65	23±2	98±20	01:32:47	+33:03:43
20190926B	190925	58752.03093855	15	957.3±0.5	51 / 44	0.97	2.2±0.2	7.6±1.5	01:42:06	+30:58:05
20191020B	191020	58776.78080366	17	465.0±0.2	102 / 101	0.38	1.04±0.10	9.1±1.8	20:30:39	+62:17:43
20191108A**	191108	58795.83082563	103	588.1±0.1	43 / 52	0.54	0.34±0.03	8.2±1.6	01:33:47	+31:51:30
20191109A	191109	58796.54885262	22	531.2±0.1	108 / 108	0.44	0.48±0.05	4.5±0.9	20:35:15	+61:49:02

\* Candidate

\*\* The arrival time published in [Connor et al. \(2020\)](#) contained an error in the barycentric correction. In this table that is rectified.

FRB 20190709A was the first FRB resulting from our survey, discovered in the first week of the survey itself. It was detected in a 3C48 calibration drift scan observation. Its fluence of 7 Jy ms puts it at about the 50th percentile of the known population at the time (cf. Fig. 34).

The FRB fluences we report are calculated using the modified radiometer equation ([Cordes & McLaughlin 2003](#); [Maan & Aswathappa 2014](#)),

$$F = S \times W = \frac{S/N \text{ SEFD}}{\sqrt{N_{\text{pol}} BW}} \sqrt{W}, \quad (2)$$

where  $F$  is the fluence,  $S$  is the peak flux density,  $W$  is the pulse width,  $S/N$  is the signal-to-noise ratio, SEFD is the system-equivalent flux density,  $N_{\text{pol}}$  is the number of polarisations (two for Apertif), and  $BW$  is the observing bandwidth of 300 MHz. The SEFD is computed from a calibrator observation taken in the same week and using the same CB as the FRB discovery (Sect. 7.1). This value is then scaled to the relative sensitivity of the SB the FRB was found in, at the best-fit position.

At 663.1 pc cm<sup>-3</sup>, the DM far exceeds the Galactic electron density predicted in the direction of this event in either NE2001 ([Cordes & Lazio 2002](#)) or YMW16 ([Yao et al. 2017](#)), as listed in Table 5. Even though we acknowledge that the actual Inter-Galactic Medium (IGM) electron density may not be very well modeled, we roughly relate the IGM DM contributions, for this and subsequent detections, to redshift as

$$\frac{\text{DM}_{\text{IGM}}}{\text{pc cm}^{-3}} \approx 930 z, \quad (3)$$

where  $z$  is the redshift and DM<sub>IGM</sub> is the DM contribution of the IGM ([Petroff et al. 2019a](#)). Assuming no DM contribution from the host galaxy then gives a redshift upper limit of  $z = 0.65$ .

The FRB exhibits a strong narrow component and potentially a second equally narrow, trailing component (see Fig. 22). The observed width of the strong component is ~400 μs, and the trailing component is equally narrow. These widths are comparable to the expected dispersion smearing within individual frequency channels, suggesting the intrinsic widths of these components to be extremely narrow. The separation between the components is about 1.3 ms. At  $z = 0.65$  the actual separation at the emission site would be only about 0.8 ms.

FRB 20190709A was detected before IQUV triggering (Sect. 5.1.2) was in production. In the Stokes-I data, the autocorrelation function of the burst spectrum indicates smooth

structures with characteristic bandwidth of order 20–30 MHz. The Galactic scintillation bandwidth is expected to be only a few MHz. However, effects of any scintillation caused by the host galaxy medium cannot be ruled out.

#### 9.1.1. Localisation of FRB 20190709A

FRB 20190709A was detected in two CBs, across a total of 23 SBs. The derived localisation region is well represented by an ellipse of 10' × 39'', as shown in Fig. 23. These FRB localisation regions are derived using statistical errors. The systematic offset that [Oostrum \(2020b\)](#) found for the localisations from drift scan observations (relevant for this FRB 20190709A and for candidate FRB 190903; Sect. 9.2) is solved here.

For all FRBs, we have searched for putative host galaxies using the GLADE galaxy catalogue ([Dálya et al. 2018](#)). The catalogue was created by combining previously existing galaxy and quasar catalogues (GWGC, 2MPZ, 2MASS XSC, HyperLEDA and SDSS-DR12Q). Although its primary objective is to identify potential gravitational wave host galaxies, we used this database to look for potential FRB hosts within the error region of ARTS FRBs. The catalogue is complete up to a luminosity distance  $d_L = 37^{+3}_{-4}$  Mpc and contains all of the brightest galaxies up to  $d_L = 91$  Mpc. While most ARTS FRBs could originate from distant galaxies beyond the completeness limit of GLADE, this catalogue does allow us to check for the presence of possible nearby host galaxies which, if they are the host galaxy, could point to a large amount of DM local to the source.

For FRB 20190709A, the GLADE catalogue contains no galaxies within the error region limits.

#### 9.2. Candidate FRB 190903

Candidate FRB 190903 (see Fig. 24) was detected just above our detection threshold. Given its low S/N it is of course quite possible that FRB 190903 is not a transient, but a non-astrophysical signal fluctuation. The candidate did, however, survive blind machine-learning and human vetting. Only then was it realized the FRB was from the repeat follow-up field on FRB 20190709A, at the same DM. No further repeat detections at this DM were, however, seen in 120 hrs of follow-up of the field (see Sect. 10.5). Its width of 23 ms is an outlier compared to the generally ~ms widths of the unambiguous detections (Table 5).



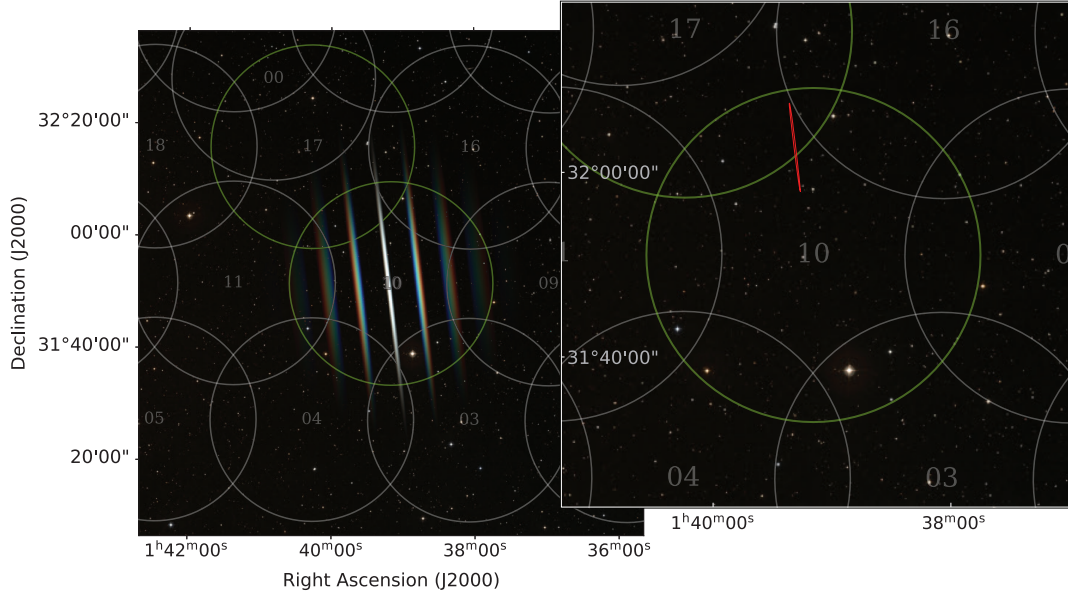


Fig. 23: The localisation region of FRB 20190709A. In both panels, and in the localisation region Figures that follow, the CBs at 1370 MHz are shown as white (non-detection) and green (detection) circles. In the left-hand side we show in the colour scale the simulated response of the SB in which the FRB was detected most strongly (cf. Fig. 16). On the right hand side, and in the follow Figures, the red, elongated and very narrow area indicates the 90% confidence level localisation area that results from combining the SB detections and upper limits of all surrounding CBs. Background image here and in the following Figures are from the Sloan Digital Sky Survey (SDSS; York et al. 2000).

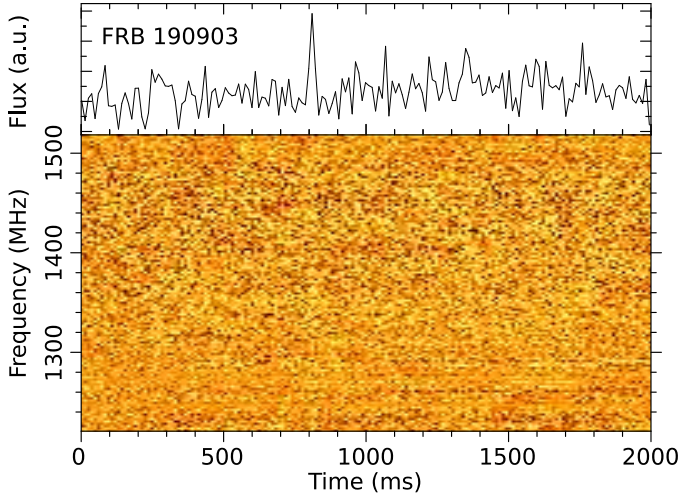


Fig. 24: Dynamic spectrum (bottom) and pulse profile (top) of FRB 190903.

### 9.2.1. Localisation of candidate FRB 190903

Because of its marginal detection in an outer beam, the localisation region of FRB 190903 is quite large: out to the SB model limit of  $40'$  from the CB centre, the region is roughly an ellipse of  $43' \times 30''$  (Fig. 25). However, we cannot exclude that FRB 190903 originated further away from main beam pattern. Given its similar DM and approximate location to FRB 20190709A, we consider that FRB 190903 might in fact be a repeat pulse of FRB 20190709A. This would place FRB 190903 far outside the main beam pattern, assuming FRB 20190709A did occur within the main beam pattern. As a precise enough model of the CB sidelobes is not currently available, we cannot further constrain

the localisation of FRB 190903 within the FRB 20190709A field and thus cannot prove whether or not these two bursts do in fact originate from the same source. There are two galaxies within a  $1'$  angular distance from the localisation region in CB 04 at a redshift  $z < 0.65$ , and one of them is located within the ellipse limits.

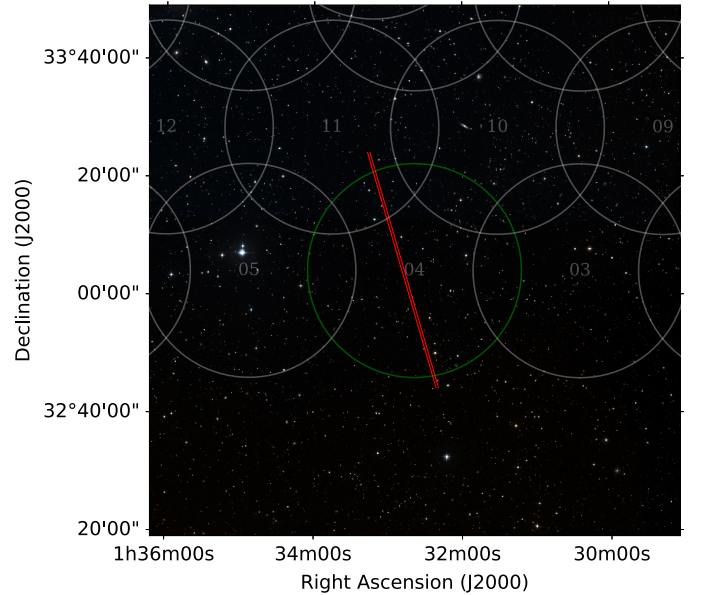


Fig. 25: The localisation region of FRB 190903. The circles and red area are as described for Fig. 23. The localisation area is not constrained towards lower declinations.

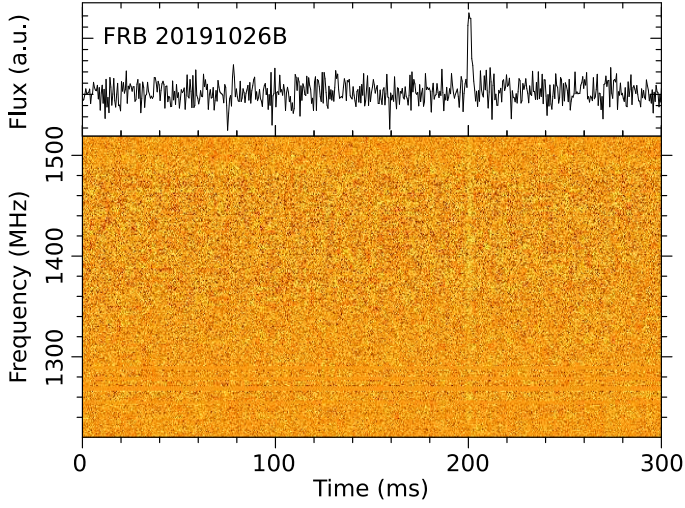


Fig. 26: Dynamic spectrum (bottom) and pulse profile (top) of FRB 20190926B.

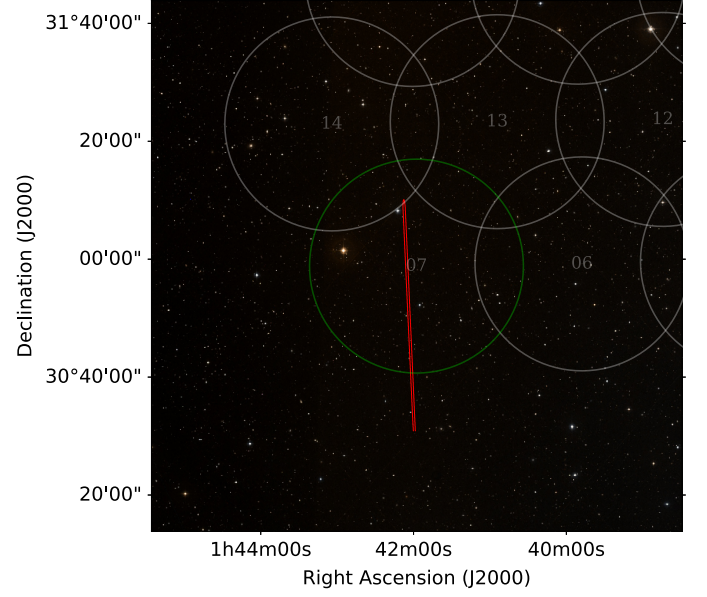


Fig. 28: The localisation region of FRB 20190926B. The localisation is not constrained towards lower declinations.

### 9.3. FRB 20190926B

FRB 20190926B was detected with a single, 2-ms wide component at a DM of  $957.3 \text{ pc cm}^{-3}$  (Fig. 26). Given that the dispersive smearing within individual channels is about 0.6 ms at the centre of the band, the burst is well resolved. The Galactic scintillation bandwidth towards this direction is expected to be only a few MHz. However, at the level of our detection significance, we see no evidence of scintillation in this burst.

This is the only burst on our sample that potentially shows an exponential decay in the intensity, associated to scattering (Fig. 27). Following the scattering characterisation described in [Pastor-Marazuela et al. \(2022b\)](#), we fit the dedispersed pulse pro-

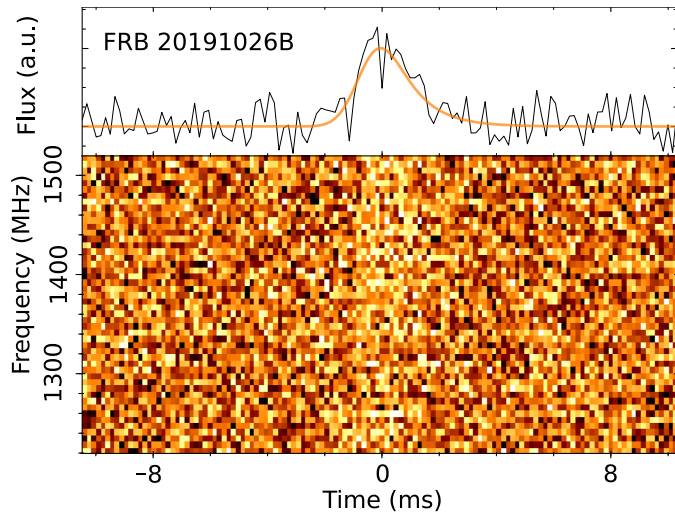


Fig. 27: FRB 20190926B at  $15\times$  higher time resolution than Fig. 26. The orange line in the top panel is the best fit when including a scattering tail.

file to a Gaussian function, with an optional convolution with a decreasing exponential. The Bayesian information criterion values are the same with or without the exponential tail; we thus cannot prove its presence, or rule it out. The best resulting scattering timescale  $\tau_{\text{sc}} = 1.0 \pm 0.3 \text{ ms}$  is several orders of magnitude larger than the expected contribution from the Milky Way. If present, it has thus likely been produced at the host galaxy or circumburst environment.

#### 9.3.1. Localisation of FRB 20190926B

FRB 20190926B was detected in one CB, across a total of 7 SBs. The derived localisation region is an ellipse of  $39' \times 30''$ , as shown in Fig. 28. Because the FRB was found in a CB on the edge of the beam pattern, the localisation region is not constrained towards lower declinations. However, if the FRB was indeed detected in a sidelobe, it would have been intrinsically extremely bright. Therefore, we find it more likely that it occurred within the main beam of CB 07 as indicated by the green circle in the figure. The GLADE catalogue contains one galaxy, SDSS 01424.24+305214.4, redshift 0.68, located at an angular distance of  $\sim 45''$  from the localisation region, within the main beam.



#### 9.4. FRB 20191020B

With a width of about 1 ms, FRB 20191020B is also resolved (Fig. 29). The burst is consistent with a single Gaussian component. The burst spectrum is fairly uniform. This detection was the first for which IQUV data saving (Sect. 5.1.2) was successfully triggered in real time. There is, however, no quasar data available in this epoch for polarisation calibration, and the S/N is too low to perform the calibration method on the FRB data itself that was demonstrated in Connor et al. (2020).

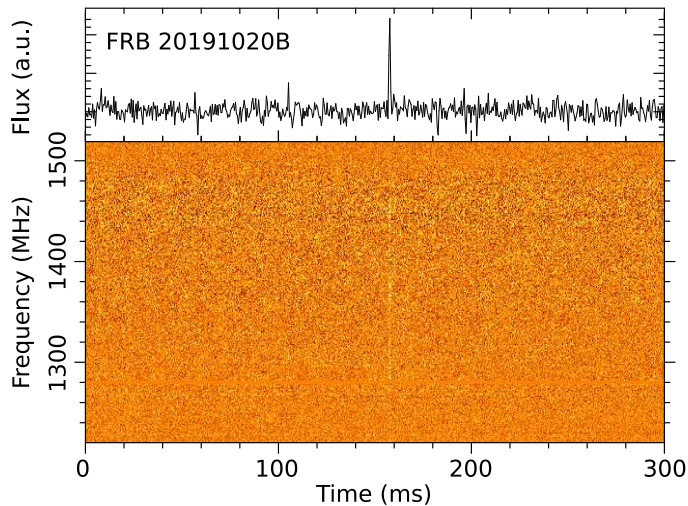


Fig. 29: Dynamic spectrum (bottom) and pulse profile (top) of FRB 20191020B.

##### 9.4.1. Localisation of FRB 20191020B

FRB 20191020B was detected in two CBs, across a total of 9 SBs. The derived localisation region is an ellipse of  $37' \times 35''$ , as shown in Fig. 30. Similar to FRB 20190926B, it was found

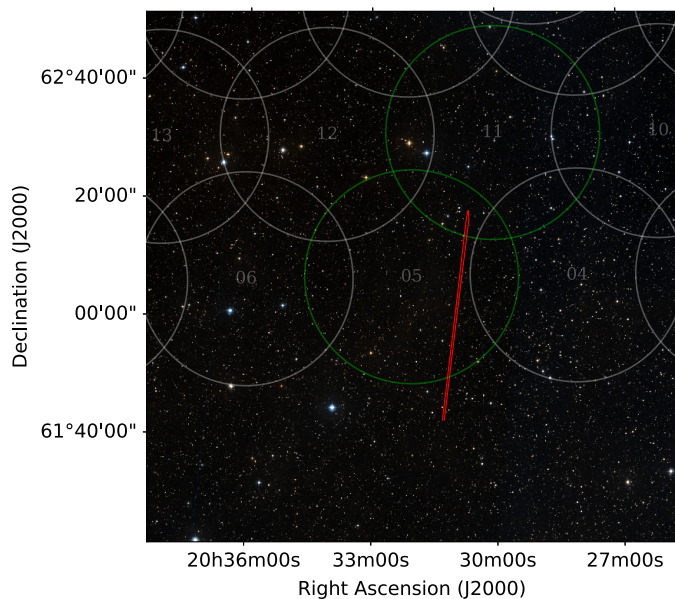


Fig. 30: The localisation region of FRB 20191020B. Again, the localisation is not constrained towards lower declinations.

in an outer CB and its localisation region is open-ended towards lower declinations. However, as for FRB 20190926B, we find it more likely that the FRB occurred in the primary beam of CB 05. There are no galaxies in the GLADE catalogue located at less than  $1'$  from the localisation ellipse within CB 05.

#### 9.5. FRB 20191108A

FRB 20191108A was detected in 48 SBs spread over three CBs, at a maximum S/N in the real-time pipeline of 60. The discovery DM was  $588 \text{ pc cm}^{-3}$ . Full-stokes data was captured and calibrated. The FRB exhibited a rotation measure of  $+474 \pm 3 \text{ rad m}^{-2}$ , much higher than expected from the Milky Way foreground, and much higher than seen in other sources close to this line of sight. The FRB is localised to a small,  $5''$  by  $7'$  region that is only  $1.20 \pm 0.05^\circ$  away from the core of Local Group galaxy M33. This discovery is described in detail in Connor et al. (2020). The implications of our various FRB lines of sight through the M33 halo are discussed in Sect. 10.5.

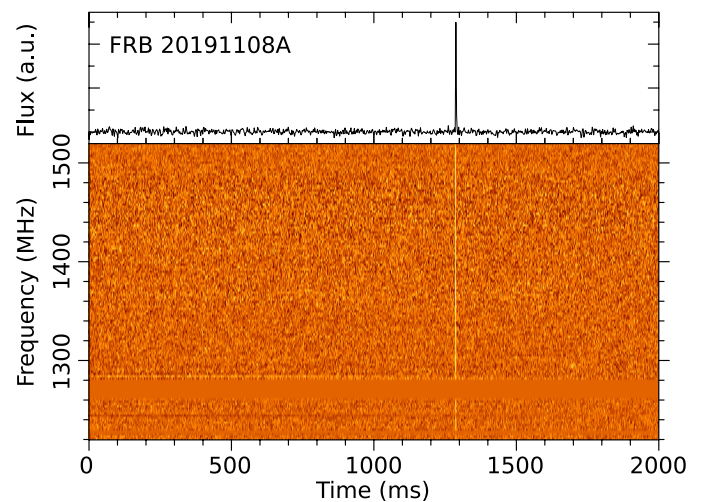


Fig. 31: Dynamic spectrum (bottom) and pulse profile (top) of FRB 20191108A.

#### 9.6. FRB 20191109A

FRB 20191109A exhibits multiple components — 2 discernible bright components and perhaps a faint third trailing component (Fig. 32). The widths of the individual components are around 0.6 ms, and at a DM of  $531 \text{ pc cm}^{-3}$  these are resolved over the intrachannel smearing. The first two components are separated by 1.2 ms. A one-off FRB model by Falcke & Rezzolla (2014), which involves collapse of a supermassive star into a black hole, predicts a leading precursor, a main burst and ring-down within 1 ms or more. While there is no sign of a precursor, the temporal structure of FRB 20191109A might be reminiscent of the above predicted ringdown. This multi-component profile, with its  $\sim 1$ -ms burst separation, could also be the FRB equivalent of quasi-periodic microstructure seen in pulsars. In Pastor-Marazuela et al. (2022a) we present additional FRBs with such structure, and provide a more detailed discussion.

FRB 20191109A also exhibits frequency structures with bandwidths of the order of 10–12 MHz. The structures are significantly correlated between the first two components, which means they are either intrinsic or are caused by scintillation af-



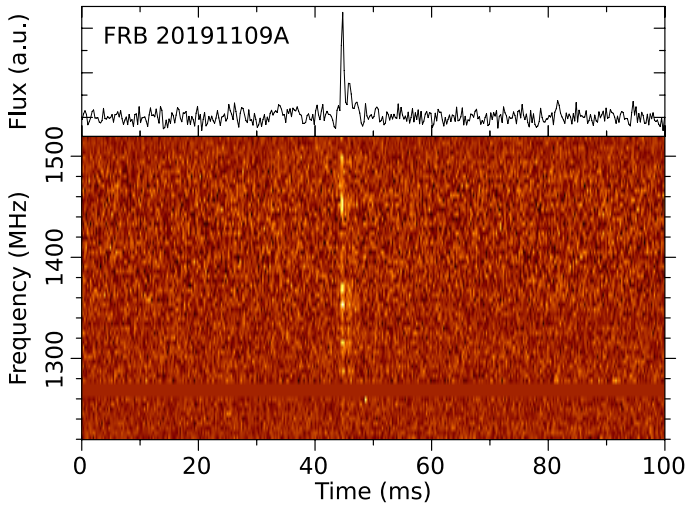


Fig. 32: Dynamic spectrum (bottom) and pulse profile (top) of FRB 20191109A.

fecting a broadband intrinsic pulse. The NE2001 and YMW16 electron density models both predict Galactic scintillation bandwidths to be much less than 1 MHz. Hence, the observed frequency structures might be intrinsic to the emission mechanism or might have been caused by the medium in the host galaxy.

Several repeating FRBs are known to exhibit frequency structures which drift downwards with time. By cross-correlating the spectra at the peaks of the first two components, we find an offset of about  $0.6 \pm 0.6$  MHz between the frequency structures under the corresponding components, consistent with zero. For a non-zero offset, the best-fit value would imply a subburst drift to lower frequencies with time at a rate of  $\sim 0.5 \text{ MHz ms}^{-1}$ , i.e., much lower than that observed for the repeating FRB 121102 ( $\sim 200 \text{ MHz ms}^{-1}$ ; Hessels et al. 2019).

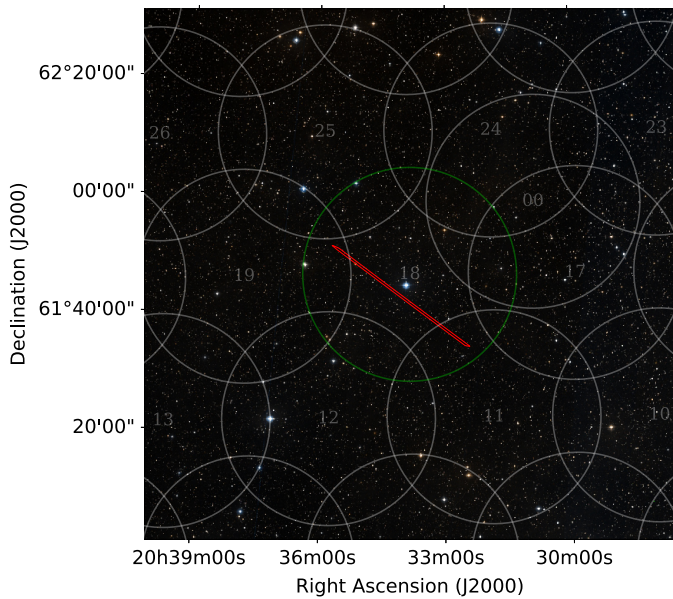


Fig. 33: The localisation region of FRB 20191109A. The CBs at 1370 MHz are shown in white (non-detection) and green (detection). The red, elongated and very narrow area indicates the 90% confidence level localisation area.

### 9.6.1. Localisation of FRB 20191109A

FRB 20191109A was detected in one CB, across a total of 15 SBs. The derived localisation region is an ellipse of  $29' \times 5''$ , as shown in Fig. 33. GLADE does not contain any galaxy located at less than  $1'$  from the localisation region.

## 10. Discussion

### 10.1. Characteristics of the discovered sample

The fluences of the Apertif-discovered bursts are around the median of the known fluence distribution (Fig. 34). When comparing the 1.4 GHz surveys, Parkes detected bursts that were generally fainter, as its SEFD is lower (30 K; Manchester et al. 2001). Only brighter FRBs are generally detected by ASKAP, on the other hand, as that system searches data from incoherently added dishes (Bannister et al. 2019). As a result, following the basic relationship between the fluence limits and the visible volume up to the relative limiting redshift, the inferred redshifts of the bursts are also higher than the ASKAP bursts, and lower than the Parkes bursts.

Given the high time and frequency resolution of ARTS (detailed below), even our distant bursts suffer less from DM-related selection effects than the CHIME bursts (Fig. 34). Assuming a spectral index of  $-0.4$ , the best-fit value for the FRB population per Gardenier & van Leeuwen (2021), to compare the fluences, the CHIME bursts are generally dimmer, yet lower redshift. The Apertif FRB sample is free of selection effects out to larger distances than CHIME (Wang et al. 2022).

The stand-out characteristic of the Apertif bursts is that they are detected at significantly narrower widths than the FRB population that was known before. Fig. 35 shows that 3 of the Apertif FRBs are among the 6 narrowest overall. The reason for this unique trait is two-fold. The observing system has very high native time resolution, and very good frequency resolution, such that instrument smearing is low. For comparison, this time and frequency resolution are  $10\times$  and  $5\times$  higher, respectively, than for the ASKAP incoherent-sum mode. This allows us to deter-

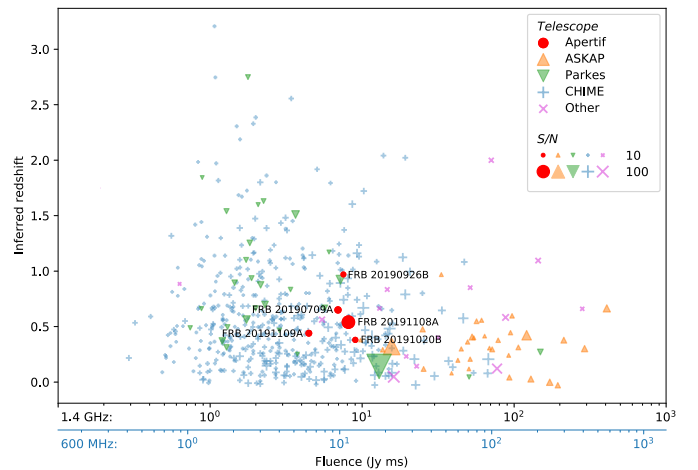


Fig. 34: The redshift and fluence for the FRBs presented here compared against those in the TNS also detected in or before 2019. In this semi-log plot, a spectral index of  $-0.4$  is used to compare the CHIME bursts (blue abscissa) with the other bursts (black abscissa). The Apertif FRBs are positioned around the mid point of the 1.4 GHz FRB fluence distribution.

mine the second, more fundamentally intrinsic characteristic: the bursts display very little temporal scattering. This means we can discern individual components even if they are only a millisecond apart, as for FRB 20191109A (and as analysed for Apertif FRB 20201020A in [Pastor-Marazuela et al. 2022a](#)).

Notable, too, are the generally large dispersion measures. There, the good frequency resolution limits the intra-channel dispersion smearing, in turn allowing short bursts to reach high signal-to-noise ratios, and be detected; whilst these same bursts might be washed out and missed by other telescopes. That brings a larger cosmic volume of bursts within our S/N reach, increasing detections at high DMs.

The 5 bursts reported here were the first discovered with the system, and IQUV polarisation recording and calibration was only successful for FRB 20191108A. For bursts discovered in 2020 and after, the availability of full-Stokes data is much higher ([Pastor-Marazuela et al. 2022b](#)).

Finally, all 5 bursts are broadband, covering the entire 300 MHz Apertif band, even if that coverage is modulated by frequency structure. This spectral modulation and band coverage fraction are qualitatively similar to the burst sample presented for ASKAP ([Shannon et al. 2018](#)). Of the four FRB archetypes proposed in [Pleunis et al. \(2021a\)](#), only two classes are represented in our sample. Morphologically, FRBs 20190926B, 20191020B and 20191108A display straight, Gaussian profiles in time, without much hint of a scattering tail, that are broadband (class I). FRBs 20190709A and 20191109A are spectrally similar but temporarily more complex (class III). We found no bursts that are narrowband (class II) or downward drifting (class IV). In principle the broad band nature of all bursts is encouraging for simultaneous detections of the same bursts with Apertif and LO-FAR (Sect. 2.2.5) although the separation of their observing frequencies is admittedly much larger than the bandwidth coverage achieved here.

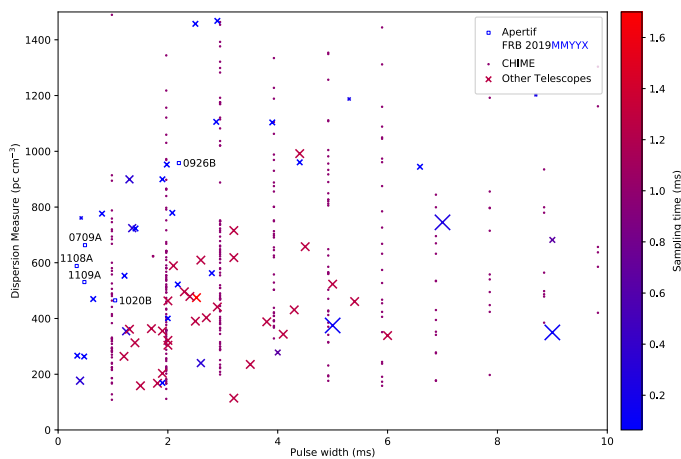


Fig. 35: The pulse width and dispersion measure of the 5 FRBs presented in this work, contrasted against the same bursts as in Fig. 34. The Apertif FRBs are among the narrowest known, and have high dispersion measure. Markers are sized and colored to reflect the frequency and time resolution, respectively. For Apertif, both are very high.

## 10.2. Survey detection rate and localisation

Our 2019 results show the total number of FRB detections per calendar year is high for ALERT at Apertif. Fig. 36 shows this

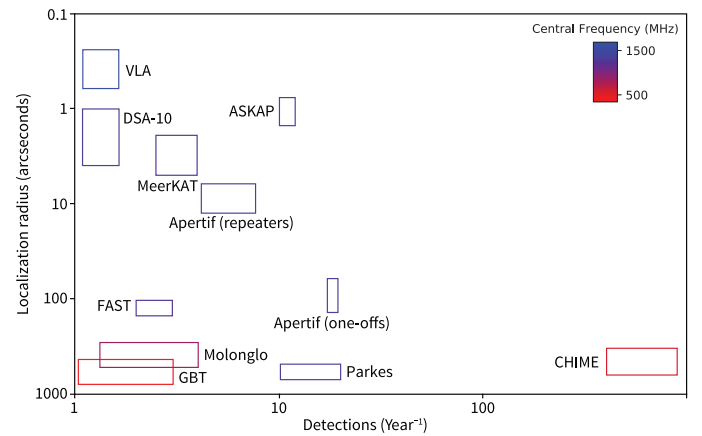


Fig. 36: Rate per calendar year versus general localisation properties for the main FRB surveys to date. Shown is localisation radius (or equivalent for elongated regions) versus the rate per year given the observing time. Apertif localisation numbers are provided for both single-burst detections (“one-offs”), and for repeat detections at different hour angles (“repeaters”), as detailed in Sect. 7.4. Data for other surveys from [Burke Spolaor \(2018\)](#), [Gardenier et al. \(2019\)](#) and [CHIME/FRB Collaboration et al. \(2021b\)](#).

large advance over (earlier) FRB surveys as carried out with GBT, VLA, and Molonglo. The high rate is a results of three main factors: the large time ALERT covered the sky, of about 1/3rd of the available observing hours; the large field of view enabled by the PAFs; and the high sensitivity from the full-field coherent beamforming.

As Apertif also offers 1-D interferometric FRB localisation, ALERT can localise bursts significantly better than single-dish surveys do. Fig. 36 shows the localisation radius (or its equivalent in case localisation regions are elongated) for the survey comparison. For Apertif we consider both the one-off case ( $\sim 100''$ , Sect. 9), and the case where multiple bursts are detected ( $\sim 10''$ , Sect. 7.4). For the rate of the latter, we assume a detected population comprised of Apertif discoveries that turn out to repeat, plus localisations from other, known, repeater FRBs. Overall, ASKAP, CHIME and Apertif each have their own tradeoff between rate and localisation accuracy, with Apertif providing both.

## 10.3. Detection rate of new FRBs versus field type

The ALERT pointing strategy (Sect. 8.2) contains three types of fields. The priority order is for fields that contain a) earlier ALERT detections, b) known repeater FRBs, or c) are blank. We find the approach works well in allowing both follow-up study and new detections. The repeat visits to detection fields (a) has allowed us to chart multiple lines of sight in fields with known sources, as demonstrated in Sect. 10.5. Fields with other known FRBs led to results detailed separately in e.g. [Pastor-Marazuela et al. \(2021\)](#) for FRB 20180916B. Mean while,  $\sim 90\%$  of the new FRB detections also occur in those known fields; only 10% of our new discoveries are from blank fields. This agrees with the distribution of the time spent on these pointings.

#### 10.4. Prospects for counterpart identification

While for some FRBs we have already identified one or more galaxies in their localisation regions, there are probably more, too faint to be included in the GLADE catalogue. Here we estimate the total number of galaxies we might expect in the localisation regions of our FRBs.

The number of potential host galaxies in a localisation region depends strongly on which types of galaxies are considered to possibly host FRB progenitors: Dwarf galaxies are far more common than massive galaxies. As the first repeating source, FRB 121102, was localised to a dwarf galaxy with a high specific star formation rate (Tendulkar et al. 2017), it was thought that this type of galaxy might be related to the FRB progenitor type. However, other FRBs — both repeating and non-repeating — have now been localised to a variety of galaxies (Chatterjee et al. 2017; Bannister et al. 2019; Ravi 2019; Prochaska et al. 2019; Marcote et al. 2020). We here apply the same analysis as done for FRB 110124 in Petroff et al. (2019b) and Oostrum (2020b), and estimate the number of dwarf galaxies ( $4 \times 10^7 M_\odot < M_{\text{stellar}} < 10^{10} M_\odot$ , i.e. between the mass of the host galaxy of FRB 121102 and the maximum dwarf-galaxy mass) and massive galaxies ( $M_{\text{stellar}} > 10^{11} M_\odot$ ) in the FRB localisation volumes. From the stellar mass function of Baldry et al. (2012), and from converting the Haynes et al. (2011) H $\alpha$  mass function at ratios between 1–10, we estimate a dwarf galaxy number density of  $n = (0.02 - 0.06) \text{ Mpc}^{-3}$ . For massive galaxies we use the luminosity function of Faber et al. (2007), and find  $n = (1.5 - 2.0) \times 10^{-3} \text{ Mpc}^{-3}$ .

The expected number of galaxies in an FRB localisation region is the galaxy number density multiplied by the comoving volume out to the redshift of the FRB, assuming that the mass functions do not evolve significantly up to the maximum redshift ( $z \approx 1$ ) of our FRB sample. The redshift is estimated from the IGM DM contribution ( $\text{DM}_{\text{IGM}}$ ) using Eq. 3.  $\text{DM}_{\text{IGM}}$  can be related to other sources of DM as

$$\text{DM}_{\text{IGM}} = \text{DM} - \text{DM}_{\text{MW}} - \text{DM}_{\text{halo}} - \frac{\text{DM}_{\text{host}}}{1+z}, \quad (4)$$

where  $\text{DM}_{\text{MW}}$ ,  $\text{DM}_{\text{halo}}$ , and  $\text{DM}_{\text{host}}$  are the DM contributions from the Milky Way, its halo, and the host galaxy (which includes the environment local to the source), respectively. For the Milky Way contribution, we take the lowest value predicted by the NE2001 and YMW16 models (see Table 5). Based on the Yamasaki & Totani (2020) model, we conservatively assume  $10 \text{ pc cm}^{-3}$  from the Milky Way halo, and we set the host galaxy contribution to zero. The resulting redshift estimates thus are conservative upper limits.

In Fig. 37 we show the resulting number of expected galaxies as a function of comoving volume. The comoving volume upper limit associated with each FRB is calculated as the total comoving volume to the FRB’s redshift multiplied by the fraction of the sky covered by the localisation region. The number of expected dwarf galaxies is  $\geq 1$  for all our FRBs, up to several hundred for FRB 20190926B. If a localisation region contains a known dwarf galaxy, one thus cannot straightforwardly conclude it is the host; other, potentially unknown dwarf galaxies will also most likely be present. In contrast, the number of expected massive galaxies is less than one for three of our FRBs. For the FRB with the smallest comoving volume associated with its localisation region, FRB 20191108A, the expected number is  $\sim 0.3$ . Assuming Poissonian error bars, the probability of finding a massive galaxy in the region by chance is then 27%. It would therefore also not be possible to definitively associate a massive galaxy with any of our FRBs.

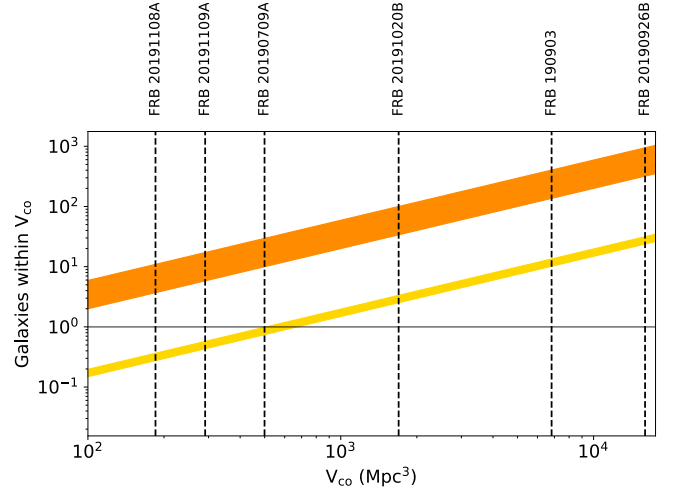


Fig. 37: The expected number of galaxies in the FRB localisation areas for a range of dwarf galaxy (orange) and massive galaxy (yellow) number densities as function of comoving volume. The comoving volume depends on both the redshift of the FRB and the size of the localisation region on-sky, and should be regarded as an upper limit. The horizontal line indicates where the expected number of galaxies is one.

In order to rule out spatial coincidence at the 95% level, we find that the comoving volume should be limited to  $\sim 30 \text{ Mpc}^3$  for association with a massive galaxy, and  $\sim 2 \text{ Mpc}^3$  for association with a dwarf galaxy. Such volumes could be reached by either better FRB localisation, or by finding an FRB at a relatively small distance. For example, an FRB with the same localisation region as our best-localised burst, FRB 20191108A, but at redshift of  $z = 0.28$ , as opposed to the current upper limit of  $z = 0.54$  (see Table 5), would be localised to the required comoving volume to rule out spatial coincidence with a massive galaxy. For a dwarf galaxy association, the redshift upper limit is  $z = 0.11$ . Such redshifts are not unreasonable within the overall FRB population; about a quarter of FRBs localised to hosts<sup>13</sup> are within that redshift range (we note, though, that localisable FRBs will generally be relatively close by, which biased the quoted fraction).

Another class of potentially interesting FRB counterparts are the persistent radio sources (PRSs). These were discovered for the first repeater FRB 121102 (Chatterjee et al. 2017; Marcote et al. 2017), and for repeating FRB 20190520B (Niu et al. 2021). As also discussed in Connor et al. (2020), radio point sources are sparser than optical galaxies, hence ARTS localisation regions might be small enough to identify radio sources associated with our FRBs.

For each FRB, we set a lower limit to the flux density of a persistent radio source that is ruled out to be in the localisation region by chance at the 10% level, following Eftekhari et al. (2018). The resulting flux densities are listed in Table 6. Given the  $5\sigma$  sensitivity limit for the Apertif imaging of  $350 \mu\text{Jy}$  as used in Connor et al. (2020), we note that Apertif imaging could identify persistent radio sources that are unlikely to be in the localisation region by chance for the majority of our FRB sample. In the first Apertif imaging data release (Adams et al. 2022) the sensitivity limit is even lower. Apertif thus not only has the capa-

<sup>13</sup> <https://frbhosts.org/>; 2022 Apr 1



Table 6: Flux densities above which no persistent radio sources are expected to be found in the FRB localisation region by chance at the 10% level, for a  $5\sigma$  sensitivity limit of  $350 \mu\text{Jy}$ .

FRB	S (mJy)
20190709A	0.21
190903	5.4
20190926B	5.3
20191020B	5.4
20191108A	0.14
20191109A	0.34

bility to discover FRBs; it can identify the potentially associated persistent radio sources as well.

### 10.5. Probing the M33 halo

As shown in Fig. 38, three of our first four detections and one unverified FRB candidate were found in the angular vicinity of Local Group galaxy M33 (the Triangulum galaxy). This is because our first detection, FRB 20190709A, was discovered during a calibration drift scan observation of the quasar 3C48, which is in the Triangulum constellation. FRB 20190926B and FRB 20191108A were later detected during follow up observations of our first discovery. The dispersion and scattering of this set of FRBs might help investigate the M33 halo. FRB 20191108A has the lowest angular separation from the core of M33 and has the smallest localisation region, but all three sources cut well through the M33 halo. They next also intersect the halo of the much larger, M31 (Andromeda) galaxy that is close to M33; and finally, the halo and disk of our own Milky Way. Interactions between these three Local Group galaxies produce connecting gas bridges that the FRBs also skewer. The hot gas bridge that Qu et al. (2021) identified between the Milky Way and M31, for example, is in the FRB line of sight. Combining the  $\sim 15^\circ$  angular distance between the FRBs and M31 with the bridge model of Qu et al. (2021) suggests the baryon bridge disperses the bursts by an additional  $\sim 40\text{--}200 \text{ pc cm}^{-3}$ . All the FRB DMs thus ought to have components that are attributable to the plasma of M33 and M31, and to the Local Group bridges; and that amount can be no larger than the minimum extragalactic DM of the three FRBs. As the lowest extragalactic DM of the three is  $\sim 540 \text{ pc cm}^{-3}$ , the electron column density in the Circumgalactic Medium of M33 and M31 must be less than  $\sim 500\text{--}340 \text{ pc cm}^{-3}$ . A larger sample of FRBs from Apertif and other surveys may better establish this bridge floor, or even a spatial DM gradient, in the direction of M31, in the future. In that sense it is unfortunate that dedicated surveys with LOFAR did not find further FRBs in either M31 (van Leeuwen et al. 2020) or M33 (Mikhailov & van Leeuwen 2016). None of these three Apertif bursts show any evidence of temporal scattering. As described in Connor et al. (2020), FRB 20191108A shows some frequency structure, but the broad,  $\sim 40 \text{ MHz}$  fluctuations are likely not due to propagation effects in the M33 halo.

### 10.6. All-sky burst rate

With ALERT we have discovered five FRBs in the 800 hours observed during 2019, corresponding to one FRB every  $\sim 6.9$  days. To convert this to an all-sky rate, we use the FoV derived in Sect. 7.2, of  $8.2 \text{ sq. deg.}$  Using a Poissonian 95% con-

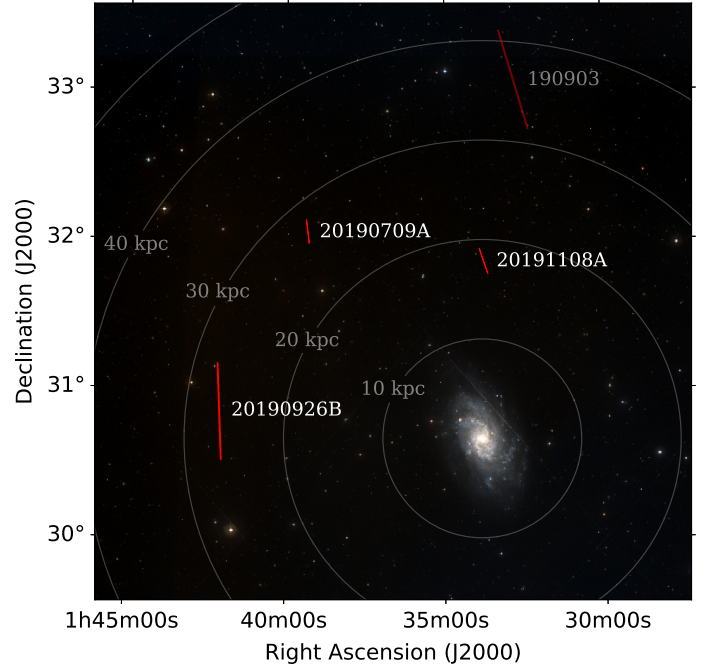


Fig. 38: The location of the three FRBs and one FRB candidate that cut within 50 kpc of M33.

fidence interval (Gehrels 1986), the inferred all-sky rate is  $700^{+800}_{-400} \text{ bursts sky}^{-1} \text{ day}^{-1}$ .

This burst rate is valid above a given fluence completeness threshold. To calculate this for Apertif, we consider the SEFD of the system, which is typically  $85 \text{ Jy}$  (Sect. 7.1). However, this value is measured for the centres of the CBs and varies across the FoV as is clearly visible in Fig. 15. The most conservative completeness threshold could be derived using twice this SEFD as we take our FoV to be the FoV out to half-power. However, most FRBs will be found in a part of the FoV that is more sensitive. Therefore we consider this limit too conservative: In 85% of the FoV, the sensitivity is at least 70% of the maximum value. Instead of 50%, we take this 70% of peak sensitivity as our sensitivity threshold. Using the radiometer equation (Eq. 2), we then find a fluence completeness threshold of  $1.6 \sqrt{\frac{W}{\text{ms}}} \text{ Jy ms}$ .

The derived burst rate is in agreement with earlier values at 1400 MHz from surveys with similar fluence thresholds (Champion et al. 2016; Bhandari et al. 2018; Rane et al. 2016).

## 11. Data and Code Releases

ARTS data are distributed as real-time alerts, and as a time-series archive. The ARTS codebase is publicly accessible.

### 11.1. Real time: VOEvents

ARTS sends out real-time FRB detection alerts using the International Virtual Observatory Alliance (IVOA) event messaging format, VOEvent. Detections that meet a pre-defined threshold for viability are communicated using the FRB VOEvent standard developed by Petroff et al. (2017). Events are generated locally on the ARTS cluster and broadcast via the ASTRON network. An internal link between ARTS and LOFAR allows for rapid triggering of the LOFAR system (cf. Pastor-Marazuela et al. 2021); currently this system is limited to triggers on previously discovered FRBs where the approximate DM and expected

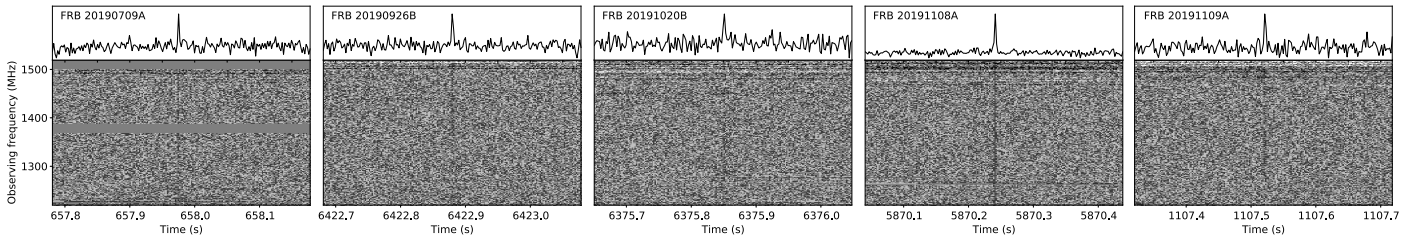


Fig. 39: Detection of the five 2019 FRBs in the archival FITS data. Top: pulse profile, bottom: dynamic spectrum.

signal-to-noise ratio are known. ARTS VOEvent alerts for new detections were distributed publicly through a COMET broker (Swinbank 2014).

### 11.2. Archive: ALTA and the VO

The public access to Apertif archived data is organized through data releases in the Apertif Long-Term Archive (ALTA) and in the Virtual Observatory (VO). These contain products for imaging (Adams et al. 2022) and for time domain. The ALTA web interface<sup>14</sup> provides querying, including an Aladin Lite based sky view, and download capabilities. ASTRONs VO service<sup>15</sup> is published in the VO Registry (Demleitner et al. 2015), making it accessible by VO applications by default. The data sets are accessible using the Table Access Protocol (TAP; Dowler et al. 2019).

The time-domain data are in PSRFITS format, with 1-bit sampling. The data are total intensity (Stokes I). For each pointing, all TABs are available. Data from before 2020 May 1 supply 384 channels of 0.8 MHz each, with a time resolution instead of 2.048 ms. Later data are archived using higher temporal and spectral resolution, and provide 768 channels of 0.4 MHz each, every 0.8 ms.

### 11.3. Data releases

Generally, data are released in batches per calendar year, together with an associated interpretation paper. Specific additional releases accompanied Oostrum et al. (2020); Connor et al. (2020) and Pastor-Marazuela et al. (2021).

Furthermore, the data specifically recorded during the Apertif Science Verification Campaign (SVC; cf. Sect. 6.4) are in a central data release on ALTA. These data include all TABs for 47 survey field from that campaign, and are publicly available<sup>16</sup>. They are in a similar PSRFITS format as the final data (Sect. 11.2), but recorded at a central frequency of 1400 MHz.

Together with this paper covering our first, 2019 discoveries, we have released the full set of 2019 survey data through ALTA<sup>17</sup> and the VO. The data releases for subsequent calendar years will follow on much shorter timescales.

The five FRBs presented in the current paper (Sect. 9) were discovered in raw, high-resolution data, but are also visible in this archived data. The resulting detection plots are displayed as Fig. 39. All archive data for these five pointings are directly

accessible through the VO<sup>18</sup>. For other pointings the metadata is directly available, but the data itself first needs to be staged from tape by the ASTRON helpdesk.

### 11.4. Code releases

The codes that are used to operate ARTS and ALERT are open source. They are free for re-use and open to contributions through the TRANSients Software ALLiance (TRASAL)<sup>19</sup>. The realtime search system code is released as AMBER (Sclocco et al. 2016; Sclocco et al. 2020) and RFIIm (Sclocco et al. 2019). The accompanying real-time data handling is released as Attema et al. (2020a,b). The pipeline orchestration code suite is freely available (Oostrum 2021c, 2020a, 2021b,a). Finally, the machine-learning post processing is released as Connor (2018).

Custom code used to generate published Apertif FRB results are released through Zenodo, for both the current paper<sup>20</sup> (van Leeuwen et al. 2022) and for previous publications (e.g. Pastor-Marazuela et al. 2020).

## 12. Future

### 12.1. Expected detection rates

Expected detection rates provide a measure by which changes in the operational performance of a system or even in the intrinsic FRB population can be identified. On the operations side, these rates can be beneficial in determining operational versus design sensitivity, setting survey strategies or even in selecting scientific priorities. To these ends, we use the FRB population synthesis code base frbpoppy (Gardenier et al. 2019) to derive the expected detection rate for ALERT. Following the results presented therein, we adopt a ‘complex’ intrinsic Euclidean FRB population, for an ALERT survey with an SEFD of  $\sim 100$  Jy and the beam sensitivity pattern as presented in Sect. 7. Based on these inputs, and scaling with respect to the HTRU detection rates, we expect ALERT to detect 1 FRB every  $4.75^{+3.33}_{-2.10}$  days (where the quoted margin is the  $1\sigma$  Poissonian error). The current detection rate found in Sec. 10.6 falls within this range, implying the system to be functioning as expected.

### 12.2. Operations time scales

The Apertif surveys are operated from 1 July 2019 until 31 Dec 2021. Per that end date, the ALERT survey for pulsars and FRBs ceases. Down-sampled data from the pointings that were covered will continue to be available through the archive.

<sup>14</sup> <https://alta.astron.nl/>, includes manual

<sup>15</sup> <https://vo.astron.nl>

<sup>16</sup> [https://alta.astron.nl/science/dataproducts/release\\_release\\_id=SVC\\_2019\\_TimeDomain](https://alta.astron.nl/science/dataproducts/release_release_id=SVC_2019_TimeDomain)

<sup>17</sup> [https://alta.astron.nl/science/dataproducts/release\\_release\\_id=APERTIF\\_DR1\\_TimeDomain](https://alta.astron.nl/science/dataproducts/release_release_id=APERTIF_DR1_TimeDomain)

<sup>18</sup> <https://science.astron.nl/sdc/astron-data-explorer/data-releases/apertif-time-domain-dr1/>

<sup>19</sup> <https://github.com/TRASAL>

<sup>20</sup> <https://doi.org/10.5281/zenodo.6415175>



### 13. Conclusions

The Apertif Radio Transient System achieves full coherent-addition sensitivity over the entire field of the view of Apertif. ARTS powers the ALERT survey, and we detect 1 FRB every 7 days of observing. The fact that the interferometer consists of steerable dishes allows for follow-up campaigns on existing and such newly detected Fast Radio Bursts. While none of the discoveries reported here were seen to repeat, other known repeater FRBs were detected and studied. All the while, new FRBs were found in these fields at the same rate as for blank fields. Five one-off FRBs were discovered in 2019, during the first 6 months of overall operation, and each was interferometrically localized. This combination of solid detection rates and good localisation is essential for mapping the magneto-ionic material in the Universe along different, well-defined lines of sight.

**Acknowledgements.** We thank Richard Blaauw, Raymond van den Brink, Chris Broekema, Lute van de Bult, John Bunton, Adam Deller, Paul Demorest, Roy de Goei, Peter Gruppen, Jason Hessels, Gemma Janssen, Gert Kruijthof, Hans van der Marel, Rob van Nieuwpoort, Jan David Mol, Gijs Molenaar, Kaushtubh Rajwade, John Romein, Gijs Schoonderbeek, Mike Sipior, Jurjen Sluman, Laura Spitler, Ben Stappers, Marc Verheijen, Nico Vermaas, and René Vermeulen for contributions to the realisation and operation of Apertif, ARTS and ALERT, and for comments and discussions. We thank Vlad Kondratiev, Joe Callingham, Sarvesh Sridhar, Emma Tigelaar, and Matthijs van der Wiel for suggesting, providing and operating the microwave oven used in Sect. 6.4. This research was supported by the European Research Council (ERC) under the European Union's Seventh Framework Programme (FP/2007-2013)/ERC Grant Agreement No. 617199 ('ALERT'); by Vici research programme 'ARGO' with project number 639.043.815, financed by the Dutch Research Council (NWO); by the Netherlands eScience Center under the project 'AA-ALERT' (027.015.G09, grant ASDI.15.406); by the Netherlands Research School for Astronomy, NOVA, under 'NOVA-NW3', and 'NOVA5-NW3-10.3.5.14'; and through CORTEX (NWA.1160.18.316), under the research programme NWA-ORC, financed by NWO. Instrumentation development was supported by NWO (grant 614.061.613 'ARTS') and NOVA ('NOVA4-ARTS'). PI of aforementioned grants is JvL. EP acknowledges funding from an NWO Veni Fellowship. The contributions of SMS were supported by NASA grant NNX17AL74G issued through the NNH16ZDA001N Astrophysics Data Analysis Program (ADAP). EAKA is supported by the WISE research programme, which is financed by NWO. BA acknowledges funding from the German Science Foundation DFG, within the Collaborative Research Center SFB1491 "Cosmic Interacting Matters - From Source to Signal". KMH acknowledges financial support from the State Agency for Research of the Spanish Ministry of Science, Innovation and Universities through the "Center of Excellence Severo Ochoa" awarded to the Instituto de Astrofísica de Andalucía (SEV-2017-0709), from the coordination of the participation in SKA-SPAIN, funded by the Ministry of Science and Innovation (MCIN). KMH and JMvdH acknowledge funding from the ERC under the European Union's Seventh Framework Programme (FP/2007-2013)/ERC Grant Agreement No. 291531 ('HISStoryNU'). RM acknowledges support from the same programme under ERC Advanced Grant RADIOLIFE-320745. This work makes use of data from the Apertif system installed at the Westerbork Synthesis Radio Telescope owned by ASTRON. ASTRON, the Netherlands Institute for Radio Astronomy, is an institute of NWO. Part of this research has made use of the EPN Database of Pulsar Profiles maintained by the University of Manchester, available at: <http://www.jodrellbank.manchester.ac.uk/research/pulsar/Resources/epn/>.

### References

Abadi, M., Agarwal, A., Barham, P., et al. 2015, TensorFlow: Large-Scale Machine Learning on Heterogeneous Systems, software available from tensorflow.org

Adams, E. A. K. & van Leeuwen, J. 2019, *Nature Astronomy*, **3**, 188

Adams, E. A. K., Adebahr, B., de Blok, W. J. G., et al. 2022, *A&A*, *submitted*

Attema, J. J., Oostrum, L. C., & van Leeuwen, J. 2020a, dadafilterbank, <https://doi.org/10.5281/zenodo.3944623>

Attema, J. J., Oostrum, L. C., & van Leeuwen, J. 2020b, dadafits, <https://doi.org/10.5281/zenodo.3944631>

Backer, D. C. 2000, in *Perspectives on Radio Astronomy: Science with Large Antenna Arrays*, ed. M. P. van Haarlem, 285

Baldry, I. K., Driver, S. P., Loveday, J., et al. 2012, *MNRAS*, **421**, 621

Bannister, K. W., Shannon, R. M., Macquart, J.-P., et al. 2017, *ApJ*, **841**, L12

Bannister, K. W., Deller, A. T., Phillips, C., et al. 2019, *Science*, **365**, 565

Bassa, C. G., Janssen, G. H., Karuppusamy, R., et al. 2016, *MNRAS*, **456**, 2196

Bera, A. & Chengalur, J. N. 2019, *MNRAS*, **490**, L12

Bhandari, S., Keane, E. F., Barr, E. D., et al. 2018, *MNRAS*, **475**, 1427

Bhardwaj, M., Gaensler, B. M., Kaspi, V. M., et al. 2021, *ApJ*, **910**, L18

Bilous, A. V., Griebmeier, J. M., Pennucci, T., et al. 2022, *A&A*, **658**, A143

Bochenek, C., Kulkarni, S., Ravi, V., et al. 2020, *The Astronomer's Telegram*, **13684**, 1, library Catalog: [www.astronomerstelegram.org](http://www.astronomerstelegram.org)

Bochenek, C. D., Ravi, V., Belov, K. V., et al. 2020, *Nature*, **587**, 59

Boersma, O. M., van Leeuwen, J., Adams, E. A. K., et al. 2021, *A&A*, **650**, A131

Bregman, J. A., Schipper, B., Beerekamp, W., et al. 2018, in *Westerbork Telescope 50th Anniversary*, Vol. 361, 11

Burke Spolaor, S. 2018, in FRB2018: Finding and understanding Fast Radio Bursts, <http://caastro.org/wp-content/uploads/2018/06/spolaor-frb2018-realfast-swinburne-1.pdf>

Caleb, M., Flynn, C., Bailes, M., et al. 2017, *MNRAS*, **468**, 3746

Camilo, F., Ransom, S. M., Halpern, J. P., et al. 2006, *Nature*, **442**, 892

Champion, D. J., Petroff, E., Kramer, M., et al. 2016, *MNRAS*, **460**, L30

Chatterjee, S., Law, C. J., Wharton, R. S., et al. 2017, *Nature*, **541**, 58

Chawla, P., Kaspi, V. M., Josephy, A., et al. 2017, *ApJ*, **844**, 140

Chawla, P., Andersen, B. C., Bhardwaj, M., et al. 2020, arXiv e-prints, arXiv:2004.02862

CHIME/FRB Collaboration, Amiri, M., Bandura, K., et al. 2018, *ApJ*, **863**, 48

CHIME/FRB Collaboration, Andersen, B. C., Bandura, K., et al. 2019, *ApJ*, **885**, L24

CHIME/FRB Collaboration, Andersen, B. C., Bandura, K. M., et al. 2020, *Nature*, **587**, 54

CHIME/FRB Collaboration, Andersen, B. C., Bandura, K., et al. 2021a, arXiv e-prints, arXiv:2107.08463

CHIME/FRB Collaboration, Amiri, M., Andersen, B. C., et al. 2021b, *ApJS*, **257**, 59

Chollet, F. et al. 2015, Keras, <https://keras.io>

Chu, Q., Howell, E. J., Rowlinson, A., et al. 2016, *MNRAS*, **459**, 121

Coenen, T., van Leeuwen, J., Hessels, J. W. T., et al. 2014, *A&A*, **570**, A60

Connor, L. 2018, liamconnor/single\_pulse\_ml: First release of single pulse machine learning code, <https://doi.org/10.5281/zenodo.1442657>

Connor, L. 2019, *MNRAS*, **487**, 5753

Connor, L. & van Leeuwen, J. 2018, *AJ*, **156**, 256

Connor, L., van Leeuwen, J., Oostrum, L. C., et al. 2020, *MNRAS*, **499**, 4716

Cordes, J. M. & Lazio, T. J. W. 2002, ArXiv:astro-ph/0207156, [arXiv:astro-ph/0207156](https://arxiv.org/abs/astro-ph/0207156)

Cordes, J. M. & McLaughlin, M. A. 2003, *ApJ*, **596**, 1142

Cruces, M., Spitler, L. G., Scholz, P., et al. 2021, *MNRAS*, **500**, 448

Dai, S., Lower, M. E., Bailes, M., et al. 2019, *ApJ*, **874**, L14

Dálya, G., Galgóczi, G., Dobos, L., et al. 2018, *MNRAS*, **479**, 2374

Day, C. K., Deller, A. T., Shannon, R. M., et al. 2020, *MNRAS*, **497**, 3335

Demleitner, M., Harrison, P., Taylor, M., & Normand, J. 2015, *Astronomy and Computing*, **11**, 91

Dénes, H., Hess, K. M., Adams, E. A. K., et al. 2022, *A&A*, *submitted*

Desvignes, G., Kramer, M., Lee, K., et al. 2019, *Science*, **365**, 1013

Dowler, P., Rixon, G., Tody, D., & Demleitner, M. 2019, Table Access Protocol Version 1.1, IVOA Recommendation 27 September 2019

Eftekhari, T., Berger, E., Williams, P. K. G., & Blanchard, P. K. 2018, *ApJ*, **860**, 73

Faber, S. M., Willmer, C. N. A., Wolf, C., et al. 2007, *ApJ*, **665**, 265

Falcke, H. & Rezzolla, L. 2014, *A&A*, **562**, A137

Fonseca, E., Andersen, B. C., Bhardwaj, M., et al. 2020, *ApJ*, **891**, L6

Gardner, D. W., Connor, L., van Leeuwen, J., Oostrum, L. C., & Petroff, E. 2021, *A&A*, **647**, A30

Gardner, D. W. & van Leeuwen, J. 2021, *A&A*, **651**, A63

Gardner, D. W., van Leeuwen, J., Connor, L., & Petroff, E. 2019, *A&A*, **632**, A125

Gehrels, N. 1986, *ApJ*, **303**, 336

Hallinan, G., Corsi, A., Mooley, K. P., et al. 2017, *Science*, **358**, 1579

Haynes, M. P., Giovanelli, R., Martin, A. M., et al. 2011, *AJ*, **142**, 170

Hess et al., K. M. 2022, *MNRAS*, *in prep.*

Hessels, J. W. T., Spitler, L. G., Seymour, A. D., et al. 2019, *ApJ*, **876**, L23

Hilmarsson, G. H., Michilli, D., Spitler, L. G., et al. 2021, *ApJ*, **908**, L10

Hobbs, G. & Edwards, R. 2012, Tempo2: Pulsar Timing Package

Hobbs, G. B., Edwards, R. T., & Manchester, R. N. 2006, *MNRAS*, **369**, 655

Holties, H., Vermaas, N., & de Goei, R. 2019, in *Astronomical Data Analysis Software and Systems XXIX*, <https://www.adass2019.nl/conference-info/posters/pdf?table=poster&id=140>

Hotan, A. W., van Straten, W., & Manchester, R. N. 2004, *PASA*, **21**, 302

Houben, L. J. M., Spitler, L. G., ter Veen, S., et al. 2019, *A&A*, **623**, A42

Hulse, R. A. & Taylor, J. H. 1975, *ApJ*, **201**, L55

James, C. W., Osłowski, S., Flynn, C., et al. 2020, *MNRAS*, **495**, 2416

Janssen, G. H., Stappers, B. W., Braun, R., et al. 2009, *A&A*, **498**, 223

Karastergiou, A., Chennamangalam, J., Armour, W., et al. 2015, *MNRAS*, **452**, 1254



- Karuppusamy, R., Stappers, B., & van Straten, W. 2008, *PASP*, **120**, 191
- Keane, E. F., Kramer, M., Lyne, A. G., Stappers, B. W., & McLaughlin, M. A. 2011, *MNRAS*, **415**, 3065
- Kramer, M. & Champion, D. J. 2013, *Classical and Quantum Gravity*, **30**, 224009
- Kramer, M., Stairs, I. H., Manchester, R. N., et al. 2006, *Science*, **314**, 97
- Kumar, P., Shannon, R. M., Lower, M. E., et al. 2022, *MNRAS*, [arXiv:2109.11535 \[astro-ph.HE\]](https://arxiv.org/abs/2109.11535)
- Kutkin, A., Oosterloo, T. A., Morganti, R. H., et al. 2022, *A&A*, *submitted*
- Law, C. J., Bower, G. C., Burke-Spolaor, S., et al. 2018, *ApJS*, **236**, 8
- Loose, M. 2016, in *Astronomical Data Analysis Software and Systems XXVI*, <http://www.adass2016.inaf.it/index.php/participants-all/4-poster/54-loose-marcel>
- Lorimer, D. R., Bailes, M., McLaughlin, M. A., Narkevic, D. J., & Crawford, F. 2007, *Science*, **318**, 777
- Maan, Y. & Aswathappa, H. A. 2014, *MNRAS*, **445**, 3221
- Maan, Y., Joshi, B. C., Surnis, M. P., Bagchi, M., & Manoharan, P. K. 2019, *ApJ*, **882**, L9
- Maan, Y. & van Leeuwen, J. 2017, *IEEE Proc. URSI GASS*, [arXiv:1709.06104](https://arxiv.org/abs/1709.06104)
- Macquart, J.-P., Bailes, M., Bhat, N. D. R., et al. 2010, *PASA*, **27**, 272
- Macquart, J. P., Keane, E., Grainge, K., et al. 2015, in *Advancing Astrophysics with the Square Kilometre Array (ASKA14)*, 55
- Manchester, R. N., Hobbs, G. B., Teoh, A., & Hobbs, M. 2005, *AJ*, **129**, 1993
- Manchester, R. N., Lyne, A. G., Camilo, F., et al. 2001, *MNRAS*, **328**, 17
- Marcote, B., Paragi, Z., Hessels, J. W. T., et al. 2017, *ApJ*, **834**, L8
- Marcote, B., Nimmo, K., Hessels, J. W. T., et al. 2020, *Nature*, **577**, 190
- Mereghetti, S., Savchenko, V., Ferrigno, C., et al. 2020, *ApJ*, **898**, L29
- Michilli, D., Seymour, A., Hessels, J. W. T., et al. 2018, *Nature*, **553**, 182
- Mikami, R., Asano, K., Tanaka, S. J., et al. 2016, *ApJ*, **832**, 212
- Mikhailov, K. 2018, PhD thesis, University of Amsterdam, <http://hdl.handle.net/11245.1/d3a5406f-e636-4bb8-a280-54a3eedd0a52>
- Mikhailov, K. & Sclocco, A. 2018, *Astronomy and Computing*, **25**, 139
- Mikhailov, K. & van Leeuwen, J. 2016, *A&A*, **593**, A21
- Niu, C. H., Aggarwal, K., Li, D., et al. 2021, *arXiv e-prints*, [arXiv:2110.07418](https://arxiv.org/abs/2110.07418)
- Oosterloo, T., Verheijen, M. A. W., van Cappellen, W., et al. 2009, in *Wide Field Astronomy & Technology for the Square Kilometre Array*, 70
- Oostrum, L. C. 2020a, ARTS tools, <https://doi.org/10.5281/zenodo.4292175>
- Oostrum, L. C. 2020b, PhD thesis, University of Amsterdam, <https://dare.uva.nl/search?identifier=abe5c8fa-1fdf-490b-ac0d-61e946f5791f>
- Oostrum, L. C. 2021a, ARTS localisation, <https://doi.org/10.5281/zenodo.4560043>
- Oostrum, L. C. 2021b, ARTS tracking beams, <https://doi.org/10.5281/zenodo.4452631>
- Oostrum, L. C. 2021c, DARC: Data Analysis of Real-time Candidates, <https://doi.org/10.5281/zenodo.4419555>
- Oostrum, L. C., Maan, Y., van Leeuwen, J., et al. 2020, *A&A*, **635**, A61
- Pastor-Marazuela, I., Vohl, D., Oostrum, L. C., & Connor, L. 2020, *Reproduction package for "Chromatic periodic activity down to 120MHz in a Fast Radio Burst"*, <https://doi.org/10.5281/zenodo.4559593>
- Pastor-Marazuela, I., Connor, L., van Leeuwen, J., et al. 2021, *Nature*, **596**, 505
- Pastor-Marazuela, I., van Leeuwen, J., Bilous, A., et al. 2022a, *arXiv e-prints*, [arXiv:2202.08002](https://arxiv.org/abs/2202.08002)
- Pastor-Marazuela, I., van Leeuwen, J., Bilous, A., et al. 2022b, *A&A*, *in prep.*
- Pearlman, A. B., Majid, W. A., Prince, T. A., Kocz, J., & Horiuchi, S. 2018, *ApJ*, **866**, 160
- Perley, R. A. & Butler, B. J. 2017, *ApJS*, **230**, 7
- Petroff, E., Hessels, J. W. T., & Lorimer, D. R. 2019a, *A&A Rev.*, **27**, 4
- Petroff, E., Hessels, J. W. T., & Lorimer, D. R. 2021, *arXiv e-prints*, [arXiv:2107.10113](https://arxiv.org/abs/2107.10113)
- Petroff, E., Bailes, M., Barr, E. D., et al. 2015a, *MNRAS*, **447**, 246
- Petroff, E., Keane, E. F., Barr, E. D., et al. 2015b, *MNRAS*, **451**, 3933
- Petroff, E., Barr, E. D., Jameson, A., et al. 2016, *PASA*, **33**, e045
- Petroff, E., Houben, L., Bannister, K., et al. 2017, *arXiv e-prints*, [arXiv:1710.08155](https://arxiv.org/abs/1710.08155)
- Petroff, E., Oostrum, L. C., Stappers, B. W., et al. 2019b, *MNRAS*, **482**, 3109
- Platts, E., Weltman, A., Walters, A., et al. 2019, *Phys. Rep.*, **821**, 1
- Pleunis, Z., Good, D. C., Kaspi, V. M., et al. 2021a, *ApJ*, **923**, 1
- Pleunis, Z., Michilli, D., Bassa, C. G., et al. 2021b, *ApJ*, **911**, L3
- Prochaska, J. X., Macquart, J.-P., McQuinn, M., et al. 2019, *Science*, **365**, aay0073
- Qu, Z., Huang, R., Bregman, J. N., & Li, J.-T. 2021, *ApJ*, **907**, 14
- Rajwade, K. M., Mickaliger, M. B., Stappers, B. W., et al. 2020, *MNRAS*, **495**, 3551
- Rane, A., Lorimer, D. R., Bates, S. D., et al. 2016, *MNRAS*, **455**, 2207
- Ransom, S. 2011, PRESTO: Pulsar Exploration and Search Toolkit, <https://ui.adsabs.harvard.edu/abs/2011ascl.soft07017R>
- Ravi, V. 2019, *MNRAS*, **482**, 1966
- Ravi, V., Catha, M., D'Addario, L., et al. 2019, *Nature*, **572**, 352
- Sanidas, S., Cooper, S., Bassa, C. G., et al. 2019, *A&A*, **626**, A104
- Schoenmakers, A., Coolen, A., & Mulder, H. 2019, in *Astronomical Data Analysis Software and Systems XXIX*, <https://www.adass2019.nl/conference-info/posters/pdf?table=poster&id=116>
- Schoonderbeek, G. W., Szomoru, A., Gunst, A. W., Hiemstra, L., & Hargreaves, J. 2019, *Journal of Astronomical Instrumentation*, **8**, 1950003
- Sclocco, A., Heldens, S., & van Werkhoven, B. 2020, *SoftwareX*, **12**, 100549
- Sclocco, A., van Leeuwen, J., Bal, H. E., & van Nieuwpoort, R. V. 2016, *Astronomy and Computing*, **14**, 1
- Sclocco, A., Vohl, D., & van Nieuwpoort, R. V. 2019, in *2019 RFI Workshop - Coexisting with Radio Frequency Interference (RFI)*, 1, [arXiv: 2001.03389](https://arxiv.org/abs/2001.03389)
- Shannon, R. M., Macquart, J.-P., Bannister, K. W., et al. 2018, *Nature*, **562**, 386
- Smits, R., Kramer, M., Stappers, B., et al. 2009, *A&A*, **493**, 1161
- Sokolowski, M., Bhat, N. D. R., Macquart, J. P., et al. 2018, *ApJ*, **867**, L12
- Spitler, L. G., Cordes, J. M., Hessels, J. W. T., et al. 2014, *ApJ*, **790**, 101
- Spitler, L. G., Scholz, P., Hessels, J. W. T., et al. 2016, *Nature*, **531**, 202
- Stappers, B. W., Hessels, J. W. T., Alexov, A., et al. 2011, *A&A*, **530**, A80
- Straal, S. M. 2018, PhD thesis, University of Amsterdam, <https://pure.uva.nl/ws/files/30186974/Thesis.pdf>
- Strom, R., Van Ardenne, A., & Torchinsky, S. 2018, 50 Years Westerbork Radio Observatory: A Continuous Journey to Discoveries and Innovations, *Astrophysics and space science library (ASTRON)*, <https://pos.sissa.it/361/>
- Swinbank, J. 2014, *Astronomy and Computing*, **7**, 12
- Szomoru, A. 2010, in *10th European VLBI Network Symposium and EVN Users Meeting: VLBI and the New Generation of Radio Arrays*, Vol. 10, 98
- Tan, G. H. 1991, in *Astronomical Society of the Pacific Conference Series*, Vol. 19, IAU Colloq. 131: Radio Interferometry. Theory, Techniques, and Applications, ed. T. J. Cornwell & R. A. Perley, 42
- Tendulkar, S. P., Bassa, C. G., Cordes, J. M., et al. 2017, *ApJ*, **834**, L7
- ter Veen, S. 2015, PhD thesis, Radboud University Nijmegen, <http://hdl.handle.net/2066/147186>
- ter Veen, S., Enriquez, J. E., Falcke, H., et al. 2019, *A&A*, **621**, A57
- Thornton, D., Stappers, B., Bailes, M., et al. 2013, *Science*, **341**, 53
- van Cappellen, W. A., Oosterloo, T. A., Verheijen, M. A. W., et al. 2022, *A&A*, **658**, A146
- van Haarlem, M. P., Wise, M. W., Gunst, A. W., et al. 2013, *A&A*, **556**, A2
- van Leeuwen, J. 2014, in "The Third Hot-wiring the Transient Universe Workshop", ed. P. R. Wozniak, M. J. Graham, A. A. Mahabal, & R. Seaman, 79
- van Leeuwen, J., Mikhailov, K., Keane, E., et al. 2020, *A&A*, **634**, A3
- van Leeuwen, J., Oostrum, L. C., Pastor-Marazuela, I., Vohl, D., & Wang, Y. Y. 2022, *Reproduction package for "The Apertif Radio Transient System (ARTS): Design, Commissioning, Data Release, and Detection of the first 5 Fast Radio Bursts"*, <https://doi.org/10.5281/zenodo.6415175>
- van Leeuwen, J. & Stappers, B. W. 2010, *A&A*, **509**, 7
- van Leeuwen, J., Kasian, L., Stairs, I. H., et al. 2015, *ApJ*, **798**, 118
- van Straten, W., Jameson, A., & Osłowski, S. 2021, PSRDADA: Distributed Acquisition and Data Analysis for Radio Astronomy
- Vermaas, N., Moss, V., & de Goei, R. 2019, in *Astronomical Data Analysis Software and Systems XXIX*, <https://www.adass2019.nl/conference-info/posters/pdf?table=poster&id=216>
- Wang, Y. Y., van Leeuwen, J., Gardenier, D. W., Oostrum, L. C., & Vohl, D. 2022, *A&A*, *in prep.*
- Yamasaki, S. & Totani, T. 2020, *ApJ*, **888**, 105
- Yao, J. M., Manchester, R. N., & Wang, N. 2017, *ApJ*, **835**, 29
- Yaron, O., Ofek, E., Gal-Yam, A., & Sass, A. 2020, *Transient Name Server AstroNote*, 70, 1
- York, D. G., Adelman, J., Anderson, Jr., J. E., et al. 2000, *AJ*, **120**, 1579

## Appendix A: Detailed Design I: Functions and Data

Three appendices with more detail on this ARTS design follow: (A) covers function and data; (B) describes hardware; and (C) presents software and firmware.

We move through the system following the end-to-end data path shown in Fig. A.1. Functions on this path either *process* data (e.g. fringe stopping, filterbank, and beamformer), or *move* data (e.g., reordering, selection, packetizing, and physical I/O).

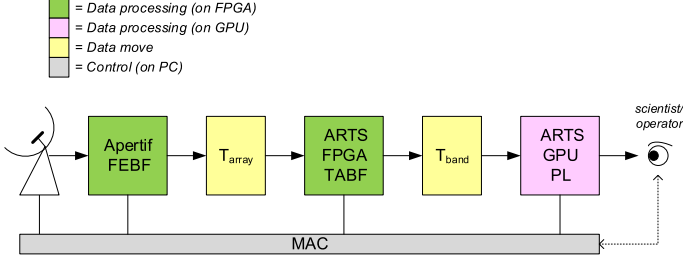


Fig. A.1: ARTS top level data path, with main interfaces. A user controls ARTS via the MAC and accesses the data products via the ARTS Pipeline processing (PL).

### Appendix A.1: Apertif Front-End Beamformer subsystem

The Apertif Front-End Beamformers (FEBFs; van Cappellen et al. 2022) provide the CB480 data to ARTS. The FEBFs first sample the data of all antenna elements at 800 MHz. This produces  $800 \text{ MHz} \times 8 \text{ bits/sample} \times 128 \text{ ADCs/dish} \times 12 \text{ dishes} = 9.8 \text{ Tbps}$ . Of these ADCs, 121 are connected to a PAF receiver element. The two polarizations are processed independently. The sampled data is next separated into 512 subbands by means of a PFB that uses a 1024-point Fast Fourier Transform (FFT). These subbands are also known as coarse channels. The subband filterbank is critically sampled, so the subband sample rate is 781250 Hz. The PAF beamformer then forms *beamlets* for these subbands. A beamlet is defined as a beam formed for one subband; hence, a beamlet is a subband with direction. Creating one beamlet requires input from all PAF antenna elements. This requires a transpose  $T_{\text{ant}}$  that groups the subbands from all 64 PAF antenna elements per polarisation. This cross connect thus transposes the data in space. A CB is formed by a group of 384 beamlets all with identical direction, that spans 300 MHz bandwidth (BW). This  $\text{CB}_{\text{BW}} = 300 \text{ MHz}$  typically ranges from 50 MHz to 350 MHz in the  $\text{RF}_{\text{BW}} = 400 \text{ MHz}$ . With  $N_{\text{dish}} = 12 \text{ dishes} \times K_{\text{CB}} = 40$  compound beams the total output of the FEBF is referred to as CB480. The CB480 data flows at  $12 \text{ dishes} \times 2 \text{ polarizations} \times$

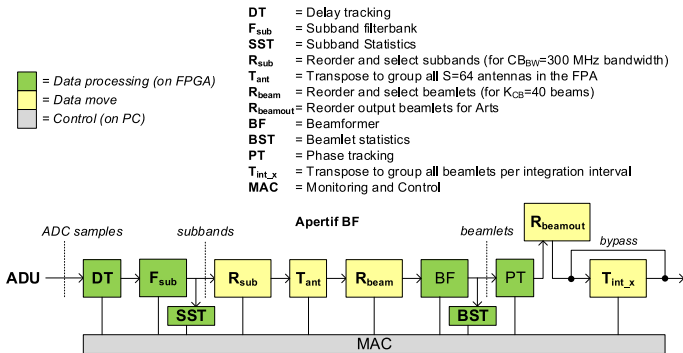


Fig. A.2: The Apertif FEBF subsystem that is input to ARTS.

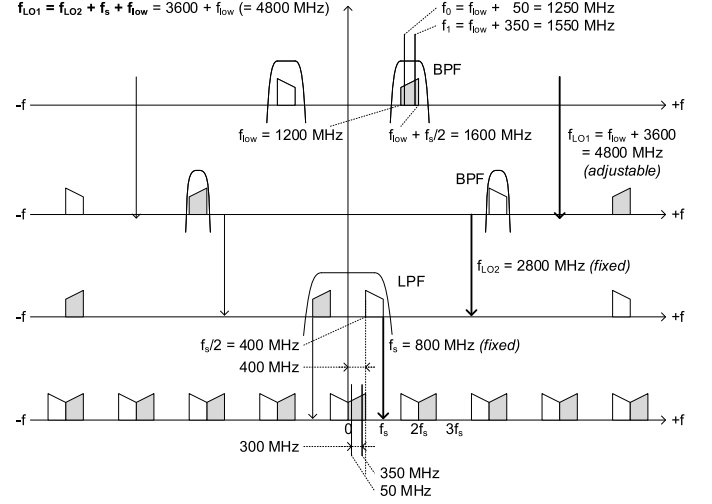


Fig. A.3: Apertif FEBF mixer and subsampling scheme for 300 MHz beams, from e.g.  $f_0 = 1250 \text{ MHz}$  to  $f_1 = 1550 \text{ MHz}$ . The  $\text{RF}_{\text{BW}} = 400 \text{ MHz}$ . The  $f_{\text{LO}2} = 2800 \text{ MHz}$  and is fixed. By setting  $f_{\text{LO}1}$  appropriately, the  $f_{\text{low}}$  maps to 0 Hz and  $f_0$  to 50 MHz.

40 CBs  $\times$  300 MHz  $\times$  2 complex  $\times$  6 bit = 3.456 Tb/s, at 9 Gbps per 10G link (Table A.1).

Fig. A.2 shows the Apertif FEBF with the subband filterbank  $F_{\text{sub}}$ , the transpose  $T_{\text{ant}}$  and the PAF beamformer (BF). The  $T_{\text{int}_x}$  transpose groups beamlets in time and is used for the Apertif correlator (X). For ARTS Timing (TAB1), the Apertif FEBF bypasses this  $T_{\text{int}_x}$  transpose. The reorder function  $R_{\text{sub}}$  selects the  $N_{\text{sel}} = 384$  subbands for  $\text{CB}_{\text{BW}} = 300 \text{ MHz}$ .

Fringe Stopping (FS) compensates for the change in geometrical delay between dishes due to the rotation of Earth. In the FEBF, it consists of true sample Delay Tracking (DT) operating on the ADC samples, followed by a residual Phase Tracking (PT) on the beamlets per compound beam. FS is thus valid for the center of each CB. The operation and the selection of subbands and beamlet are carried out by MAC (Sect. 4.2.1). It also sets fringe stopping coefficients and the FEBF weights that point the CBs.

### Appendix A.2: Frequency and bandwidth

The FEBF operates in the 1130–1720 MHz Radio Frequency (RF) range (van Cappellen et al. 2022). Fig. A.3 shows how a 400 MHz is down converted and subsampled, and how the central frequency can be adjusted in steps of 10 MHz.

Typically the middle subbands 64 to 447 are selected (cf. Fig. A.3 and A.4) to achieve 300 MHz bandwidth. Down stream, these subbands are split into 4 sub-channels in the TABF (Fig. A.4). By implementing this split as a 64-channel separation followed by a 16-channel integration, the impact of the channel leakage in the FFT is reduced, while effectuating the intended downsampling in time (Sect. 3.5).

The early design choice for  $400/512 \text{ MHz} = 781250 \text{ Hz}$  channels means frequency channels need to be converted to tie Apertif into e.g. LEAP for pulsar timing (Bassa et al. 2016) and into standard VLBI. Both use (multiples of) 1 MHz channels.

### Appendix A.3: Data formats and interface data loads

The ARTS beamformers (Sect A.4) produce data in voltage and/or power data formats (Fig. A.5).

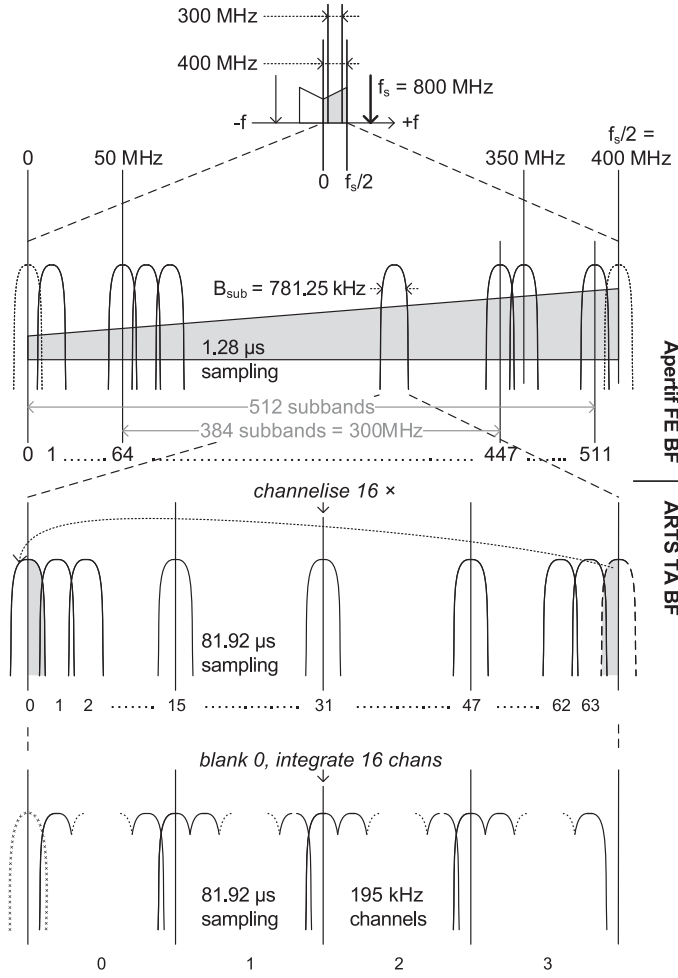


Fig. A.4: Polyphase filterbanks in the Apertif FEBF, with  $N_{\text{sub}} = 512$  subbands, followed by a second filterbank, plus an integration step, in the TABF.

For voltage beams, such as the CB and the TAB1 for Timing, the data vector  $[X_{\text{re}}, X_{\text{im}}, Y_{\text{re}}, Y_{\text{im}}]$  consists of the complex samples for both polarizations.

The search modes use integrated Stokes power data beams, such that samples can be integrated to achieve data reduction (see Sect. 4.1.1). The Stokes vector  $[I, Q, U, V]$  is based on both polarizations X and Y as:

$$\begin{aligned} I &= XX^* + YY^* \\ Q &= XX^* - YY^* \\ U &= X^*Y + XY^* = 2 * \text{Re } XY^* \\ V &= X^*Y - XY^* = -2 * \text{Im } XY^* \end{aligned} \quad (\text{A.1})$$

Table A.1 summarizes the data loads on the ARTS Beamformer (BF) interfaces. The default input data is CB480

Mode	Data Type	Dish N	CBs N	TABs N	$N_{\text{int}}$	Load Gbps
CB480	XY	12	40	-	-	3456
CHAN320	XY	8	40	-	-	3456
TAB1	XY	12	1	1	-	9.6
TAB480	XY	12	40	12	-	4608
TAB480	IQUV	12	40	12	16	288
TAB480	I	12	40	12	16	72
I+IQUV/node		12	40	12	16	9
IAB40	IQUV	12	40	-	16	24

Table A.1: Data-rate loads for ARTS TABF interfaces. The number of samples per integration is  $N_{\text{int}} = 16$ , for  $81.92 \mu\text{s}$  sampling. In XY modes the data are voltages. I and IQUV modes are detected Stokes data. I+IQUV/node denotes the load of the combine Stokes I and IQUV data per GPU workstation, at  $(288 + 72)/40 = 9$  Gbps.

for a dedicated search (Sect. A.1). For commensal searching (Sect. 3.7), the input data load in CHAN320 mode is 12 dishes  $\times$  2 polarizations  $\times$  40 CB  $\times$  300 MHz  $\times$  2 complex  $\times$  9 bit = 3.456 Tbps.

The default search output is 12 TABs per CB for TAB480. Optionally each first TAB can be replaced by an IAB for IAB40. The search mode internally first creates TAB480 voltage streams, totaling 12 dishes  $\times$  2 polarizations  $\times$  40 CB  $\times$  300 MHz  $\times$  2 complex  $\times$  8 bit = 4.608 Tbps. For each TAB the output consists of both a Stokes I and a Stokes-IQUV data stream. As the Stokes I data (for real time detection) and IQUV data (for data buffering) have different purpose and format, the Stokes I data is included (again) in the IQUV data stream.

#### Appendix A.4: Beamforming Algorithms

The coherent beamformer weights and sums the input voltage data from dishes  $d$ . The weights  $w_{\text{TAB}}$  are complex values. The coherent beamformer operates separately per polarisation  $p$ . The single voltage output data  $v\text{TAB}$ , that directly operates on the input beamlets  $b$ , is

$$v\text{TAB}(p, b) = \sum_{d=0}^{N_{\text{dish}}-1} w_{\text{TAB}}(d, b) \times \text{CB}(p, d, b) \quad (\text{A.2})$$

For the intermediate voltage TABs used in the *survey* modes, the same weight is used for all subchannels:

$$v\text{TAB}(p, s) = \sum_{d=0}^{N_{\text{dish}}-1} w_{\text{TAB}}(d, b) \times \text{CB}(p, d, s) \quad (\text{A.3})$$

Using Eq. A.1 these  $v\text{TAB}$ s are first converted into full Stokes power data and next integrated over  $N_{\text{int},a} = 16$  subchannels into each channel  $c$ , resulting in the integrated power  $p\text{TAB}$  stream to the search PL:

$$p\text{TAB}(c) = \sum_{s=0}^{N_{\text{int},a}-1} \text{Stokes}(v\text{TAB}(p, s)) \quad (\text{A.4})$$

In contrast to the TABs, the incoherent beamformer already operates on power data (see Fig. A.5). Weights are generally 0 or 1. It, too, next integrates over the subchannels:

$$\text{IAB}(c) = \sum_{s=0}^{N_{\text{int},a}-1} \sum_{d=0}^{N_{\text{dish}}-1} w_{\text{IAB}}(d) \times \text{Stokes}(\text{CB}(p, d, s)) \quad (\text{A.5})$$

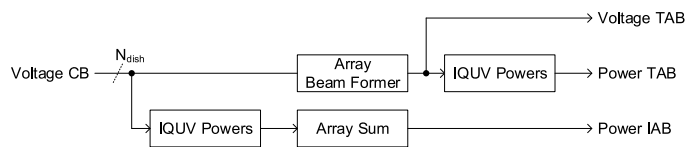


Fig. A.5: Coherent and incoherent array beamforming in ARTS.



FPGA		# BRAM × 1000	# multipliers × 1000
16 UNB	128	150 / 158 M9K (94%)	122 / 165 (74%)
4 UNB2	16	41 / 43 M20K (95%)	22 / 24 (90%)

Table A.2: The FPGA resources used versus their availability, over the ARTS TABF. Listed are the Uniboard (UNB) and Uniboard<sup>2</sup> (UNB2) systems, 16 and 4 boards respectively. For the commensal search on Uniboard<sup>2</sup>, resources for the channeliser that also serves the correlator are not included. The BRAM and multiplier usage is noted as Used/Available [Type] (Percentage).

#### Appendix A.5: FPGA Usage

Each UNB uses 8 Stratix IV FPGAs. Each UNB2 uses 4 Arria10 FPGAs. Both are clocked at 200 MHz.

The FPGA usage of the *connectivity* is defined by the required optical links. Each entire UNB (with OEB, see Sect. B.2) and each individual FPGA on UNB2 can connect 24 optical 10G links. The 384 10G links that come in from the FEBF thus determine that the TABF requires at least 16 UniBoards or 4 UNB2. The usage of the *logic* in the FPGA is split over the utilization of the flip flops (FF) and the lookup tables (LUT). Each Stratix IV has 182,400 FF, each Arria10 has 1,708,800 FF.

The *memory* in the FPGA is organized in Block RAMs (BRAMs), that can also be used as FIFOs. The *multiplier* usage follows from Sect. A.4 and the number of TABs/CB. The 16 UNBs can form up to 14 TABs/CB, where only 12 are required for the dedicated search (cf. Eq. D.3, Sect. D.1). The 9 TABs/CB required for commensal search can exactly fit 4 UNB2, but only if channel filterbanking is done in the Aperitif Correlator (Sect. 3.7). Table A.2 lists the FPGA resource usage in the TABFs.

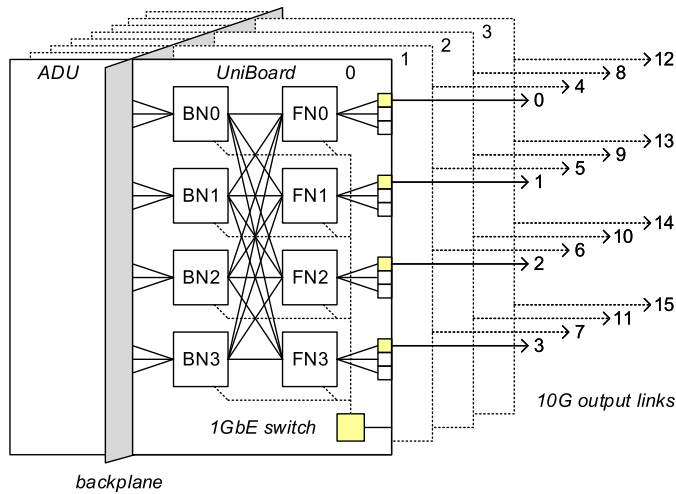


Fig. B.1: One FEBF subrack with 4 UniBoards per telescope path. The FPGAs are marked Back Node (BN) and Front Node (FN).

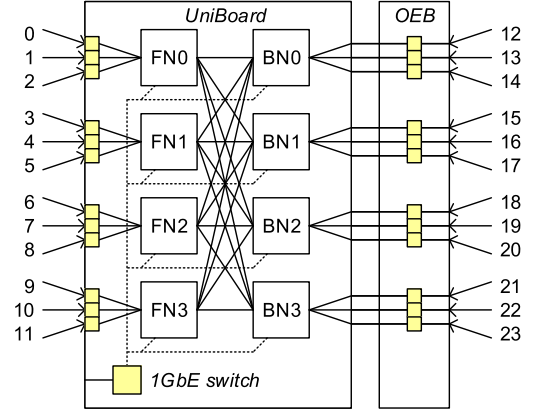


Fig. B.2: One UniBoard + Optical-Electrical Board. This unit processes 18.75 MHz for 24 telescope paths.

## Appendix B: Detailed Design II: Hardware

### Appendix B.1: Uniboards for FEBF

Each FEBF subsystem of Fig. A.2 processes one polarization from one dish for all CBs on one independent hardware sub-rack (Fig. B.1). There are thus 24 of these, each containing 4 UNBs. Through a backplane the UNBs connect to each other, and to 8 Analogue to Digital Unit (ADU) boards that together host 64 ADCs, to digitize the data from the 61 antenna elements in the PAF (van Cappellen et al. 2022). On each UNB, the data is channelized on the 4 Back Node (BN) FPGAs and beamformed on the 4 Front Node (FN) FPGAs. The transpose  $T_{\text{ant}}$  is implemented through a combination of the backplane and the mesh interconnects. The 384 FEBF 10G links output the CB480 data to the TABF.

### Appendix B.2: UniBoards and OEBs for TABF

Fig. B.2 shows the UNB with the OEB. The 8 FPGAs on UNB are StratixIV type EP4SGX230KF40C2. In contrast to the FEBF, there is no distinction between FN and BN in the TABF. All FPGAs have the same function. That is possible because the OEBs extends the BNs with fiber optics IO. Then, each FPGA supports three 10G links. On the UNB, the mesh, consisting of 5 Gbps transceiver links, interconnects the FPGAs as shown in Fig. B.2. One UNB plus OEB provides full duplex I/O for 240 Gbps. In total there are 128 FPGAs on the 16 independently-operating UNB in the TABF.

### Appendix B.3: Uniboards for TABF

On UNB2 all FPGAs are connected identically. There are no BN or FN, only Processing Node (PN). There are 16 such FPGAs, type Arria10 10AX115U2F45E1SG, in the 4 UNB2s comprising the TABF, as shown in Fig. B.3. In most respects, such as connectivity, transposing, and signal processing, one PN on UNB2 replaces an entire UNB.

### Appendix B.4: Connecting UniBoard to UNB2

The 128 FPGAs on the 16 UNBs are each connected to the Aperitif FEBF via 3 incoming Rx-only 10G links. Outgoing data is carried over the corresponding Tx-only link. The first 10G link



### Appendix C.2.2: Message Bus

The message bus consists of queues, exchanges, and brokers. Messages are wrapped in an envelope that contains the address of the recipient, and sent to an exchange. A broker helps forward the message to a destination queue for pick up by the recipient. Messages queuing provides reliable communication, guaranteed message delivery, and is easy to use. Routing is run-time configurable.

Apertif uses the Advanced Message Queuing Protocol (AMQP), which is based on IEEE standard (ISO/IEC 19464). Apache Qpid provides an implementation of AMQP, in both C++ and in Python. The choice for Qpid was driven by experience in LOFAR. We run a broker daemon on every host. A single exchange routes messages to their destination queues. Each component has queues for difference message types.

### Appendix C.2.3: Layered Design

The Monitoring & Control software follows a layered design, from drivers (lowest), to controllers, to orchestration (highest). The drivers interface with hardware, over Ethernet. All drivers are written in Python although the UniBoard driver is partly in C++ for performance. The controllers, next, handle Message Bus commands and serialize access to the drivers. Some high-level commands are sent to the whole system (e.g., "Start Observation"). Other, low-level commands are subsystem or driver oriented (e.g., "get\_status"). Different applications in the orchestration layer, finally, set up components throughout the system as a whole.

### Appendix C.2.4: Software Components

Each component has a functional and a management interface (van Cappellen et al. 2022). Both support normal-priority synchronous function calls, and high-priority asynchronous calls. Each component also generates events and notifications.

### Appendix C.2.5: Controllers

The controller framework has three main tasks. A RequestHandler places new messages from the bus into the command queue. An ExecutionHandler schedules and executes these queued commands. A ResponseHandler monitors the resulting response queue.

### Appendix C.3: Science-pipeline software

#### Appendix C.3.1: Pulsar timing

The components of the pulsar timing pipeline are detailed in Fig. C.3. The arts-0 machine contains two sets of NIC, CPU, and GPU. Each set is connected by a dedicated interconnect, and the data handling and reduction processes are pinned to the appropriate network ports, compute cores, and GPUs. This streamlining was essential for reaching real-time performance without data loss.

#### Appendix C.3.2: Transient searching

The detailed overview of the ARTS cluster survey controllers described in Sect. 4.2.3 and 5.1.2 are presented in Fig. C.4.

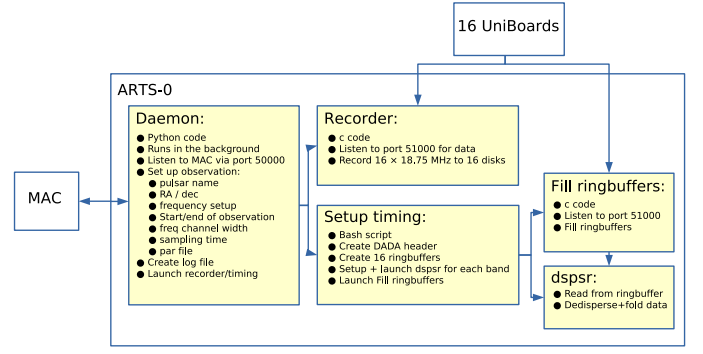


Fig. C.3: Schematic overview of the ARTS timing software pipeline

### Appendix D: Tied-array beam simulations

The hierarchical beam forming scheme used for ARTS was introduced at a high level in Sect. 2.4.2. In this appendix we provide a more quantitative discussion; first on the formation of Tied-Array Beams (TABs); next, on combining TABs to Synthesized Beams (SBs) and Tracking Beams (TBs).

#### Appendix D.1: Tied Array Beams

To determine many TABs are required to cover the Compound Beam (CB), we will assume that the separation between TABs,  $\theta_{\text{sep}}$  is equal to their half power beam width (HPBW), which depends on the observing wavelength  $\lambda$  and the projected longest baseline  $B_{\text{max}}$  as

$$\theta_{\text{sep}} = \alpha \frac{\lambda}{B_{\text{max}} \cos(\theta_{\text{proj}})}, \quad (\text{D.1})$$

where  $\theta_{\text{proj}}$  is the angle between the plane perpendicular to the linear WSRT configuration and the line of sight. We determine  $\alpha$  empirically, for  $\theta_{\text{proj}} = 0$ . We find that for the 144-m spaced arrays of 8 and 10 dishes (Apertif-8, dishes RT2–RT9,  $B_{\text{max}} = 1008$  m; and Apertif-10, comprising RT2–RTB,  $B_{\text{max}} = 1296$  m),  $\alpha = 0.78$  and  $\alpha = 0.80$  respectively.

If the TABs together cover the angular distance equal to that between a TAB main beam and its first grating response, they provide full coverage of the CB, by a combination of their main beams and first grating response. The grating distance  $\theta_{\text{grat}}$  depends on the observing wavelength and the projected common quotient baseline  $B_{\text{cq}}$  of the regular array as

$$\theta_{\text{grat}} = \arcsin\left(\frac{\lambda}{B_{\text{cq}} \cos(\theta_{\text{proj}})}\right) \approx \frac{\lambda}{B_{\text{cq}} \cos(\theta_{\text{proj}})}, \quad (\text{D.2})$$

where the approximation holds for small angles.

The number of TABs required per CB,  $N_{\text{TAB}}$ , then follows from the ratio of the grating distance and the TAB separation:

$$N_{\text{TAB}} = \frac{\theta_{\text{grat}}}{\theta_{\text{sep}}} = \frac{B_{\text{max}}}{\alpha B_{\text{cq}}}. \quad (\text{D.3})$$

Note that the wavelength and the projection angle cancel. This implies the number of TABs required depends on neither the projection angle nor the frequency. The number of TABs can be kept unvarying. Using Eq. D.3, we find that 12 and 9 TABs are needed for Apertif-10 and Apertif-8 respectively.



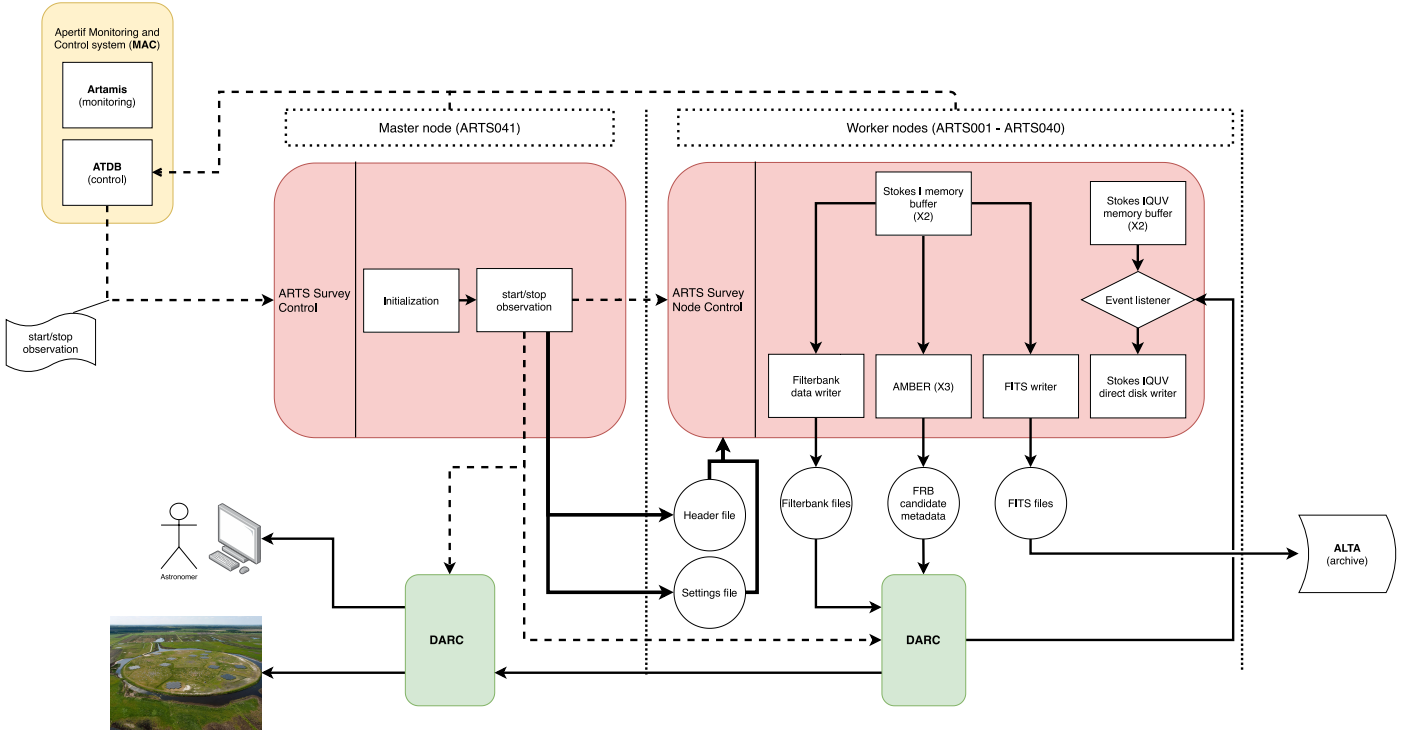


Fig. C.4: The direct interactions of the ARTS specific survey controllers. The controllers are represented by the red boxes. Dashed lines represent system control messages. Communication between the monitoring system (ARTAMIS) and the nodes, as well as any relevant communication between MAC and other components of the system (e.g. ALTA) are omitted for clarity. Since the stokes IQUV data is post processed before being used, the direct disk writer does not show any output.

#### Appendix D.2: Synthesized Beams

As shown by Eq. D.2, the grating lobe distance is frequency-dependent. This is illustrated in Fig. D.1, which shows the grating response of the central TAB at 1500 MHz and the TAB left from the central beam at 1367 MHz for Apertif-10. The first grating response right from the center of these two TABs coincides. This shows that a transient signal received in the first grating response of the central TAB to the right of the center at 1500 MHz will not be detected in the corresponding grating re-

sponse at 1367 MHz, but by the corresponding grating response of the first TAB left from the central TAB at 1367 MHz. For all but the main beam of the central TAB, we therefore may have to combine chunks of bandwidth from different TABs to form an SB at a given distance from the CB center.

In principle, there is an optimal combination of chunks of bandwidth from different TABs for each position within the FoV. In practice, the number of Synthesized Beams (SBs) that we can form is limited. A practical minimum number of SBs can be set by considering the TAB separation at the highest operating frequency, i.e., take

$$\theta_{\text{SB}} = \theta_{\text{sep}}(f_{\text{max}}) = \alpha \frac{\lambda_{\text{min}}}{B_{\text{max}}}. \quad (\text{D.4})$$

For Apertif-10, we found  $\alpha = 0.80$  and we have  $B_{\text{max}} = 1296$  m. Assuming  $f_{\text{max}} = 1500$  MHz and a field-of-view of 30 arcmin, we find that the number of SBs required is 71. A grid where SBs are spaced at 0.5 HPBW to improve sensitivity across the field-of-view results in 151 SBs. While both modes are possible in ARTS, its standard operation uses 71 SBs, based on compute-load trade-offs throughout the entire search signal chain.

At a given frequency, the optimal contribution to the SB denoted by index  $n_{\text{SB}}$  is coming from a specific grating response denoted with index  $n_{\text{gr}}$  from TAB with index  $n_{\text{TAB}}$ . In the remainder of this section, we determine which grating response from which TAB gives the optimal contribution to a given SB. Since the position shift of the grating responses over frequency increases with distance from the main beam, it is convenient to choose the reference position to be in the center of the CB. This intuitively leads to an indexing scheme in which 0 denotes the central position, a negative index implies a position left or westward of the center and a positive index denotes a position right

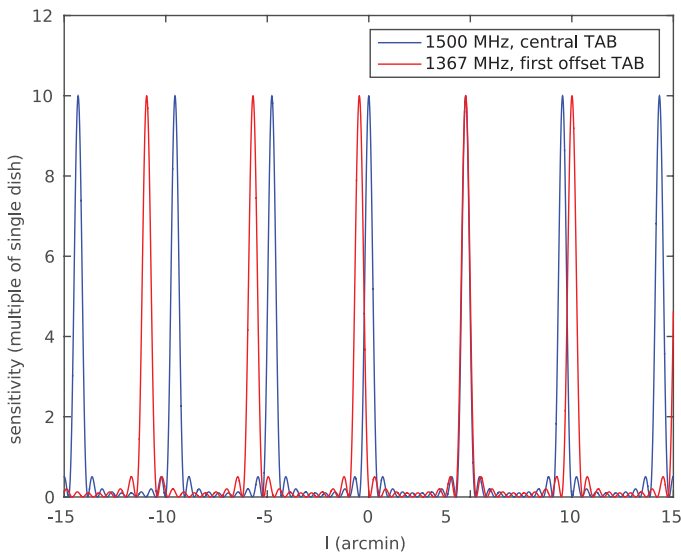


Fig. D.1: Grating response of the central TAB at 1500 MHz and the first TAB left from the center at 1367 MHz for Apertif-10.

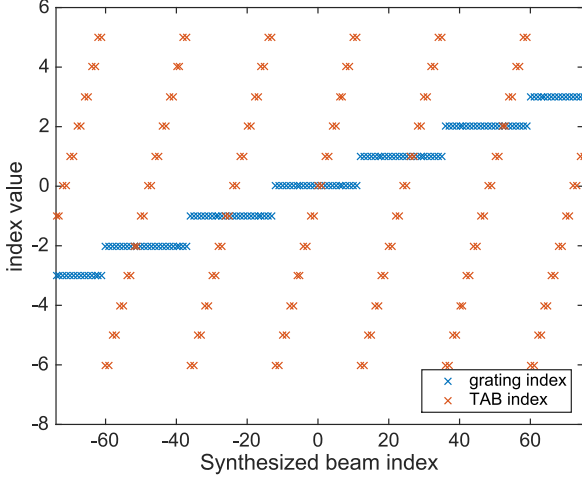


Fig. D.2: Grating index and TAB index for each SB index at the highest frequency.

or eastward of the center. For example,  $n_{\text{gr}} = -1$  denotes the first grating response left from the main beam,  $n_{\text{TAB}} = 0$  denotes the central TAB and  $n_{\text{SB}} = 5$  denotes the synthesised beam located five grid points to the right of the center of the CB.

We assign a grating index and a TAB index at the highest frequency to each SB index. We first determine the closest grating response of the central TAB by  $n_{\text{gr}} = \lceil n_{\text{SB}}/N_{\text{TAB}} \rceil$ , where  $\lceil \cdot \rceil$  denotes rounding upward towards the next higher integer value. Next, we determine the TAB index such that  $n_{\text{TAB}} = \{-N_{\text{TAB}}/2, -N_{\text{TAB}}/2 + 1, \dots, N_{\text{TAB}}/2 - 2, N_{\text{TAB}}/2 - 1\}$  by calculating

$$n_{\text{TAB}} = n_{\text{SB}} \bmod N_{\text{TAB}} \quad (\text{D.5})$$

and subtracting  $N_{\text{TAB}}$  if  $n_{\text{TAB}} > N_{\text{TAB}}/2 - 1$ .

Figure D.2 shows the resulting grating indices and TAB indices for all SB indices when  $N_{\text{TAB}} = 12$ . Note that the calculation above holds for even  $N_{\text{TAB}}$ . A similar convention can be defined for odd  $N_{\text{TAB}}$ . This is not spelled out here to keep this section concise.

The position of the SB with index  $n_{\text{SB}}$  is described by

$$\theta_{n_{\text{SB}}} = n_{\text{SB}}\theta_{\text{SB}} = n_{\text{gr}}\theta_{\text{grat}}(f_{\text{max}}) + n_{\text{TAB}}\theta_{\text{sep}}(f_{\text{max}}). \quad (\text{D.6})$$

Since  $\theta_{\text{grat}}$  and  $\theta_{\text{sep}}$  are frequency-dependent, at a certain (lower) frequency, the grating response of the next TAB will be at the same position and is therefore the optimal choice at that frequency. To find the frequency at which the position of the grating response of the next TAB at frequency  $f_0$  coincides with the grating response of the original TAB at  $f_{\text{max}}$ , we solve  $f_0$  from

$$n_{\text{gr}}\theta_{\text{grat}}(f_{\text{max}}) + n_{\text{TAB}}\theta_{\text{sep}}(f_{\text{max}}) = n_{\text{gr}}\theta_{\text{grat}}(f_0) + (n_{\text{TAB}} - \text{sgn}(n_{\text{SB}}))\theta_{\text{grat}}(f_0), \quad (\text{D.7})$$

where  $\text{sgn}$  denotes the signum function. Substitution of Eq. D.1 and Eq. D.2 while replacing  $\lambda$  by  $c/f$  and taking  $\theta_{\text{proj}} = 0$ , we obtain

$$n_{\text{gr}} \frac{c}{f_{\text{max}} B_{\text{cq}}} + n_{\text{TAB}} \frac{\alpha c}{f_{\text{max}} B_{\text{max}}} = n_{\text{gr}} \frac{c}{f_0 B_{\text{cq}}} + (n_{\text{TAB}} - \text{sgn}(n_{\text{SB}})) \frac{\alpha c}{f_0 B_{\text{max}}}, \quad (\text{D.8})$$

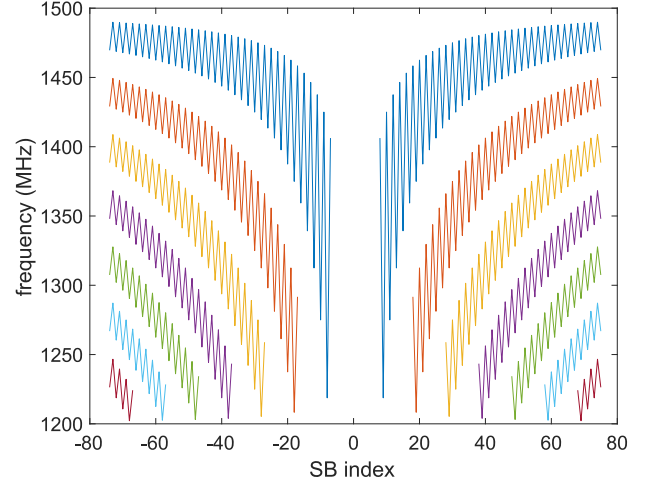


Fig. D.3: Switching frequencies for all SBs of Apertif-10 covering a FoV of 30 arcmin over the frequency range from 1200 to 1500 MHz.

which gives

$$f_0 = f_{\text{max}} \frac{n_{\text{gr}} B_{\text{max}} + (n_{\text{TAB}} - \text{sgn}(n_{\text{SB}})) \alpha B_{\text{cq}}}{n_{\text{gr}} B_{\text{max}} + n_{\text{TAB}} \alpha B_{\text{cq}}}. \quad (\text{D.9})$$

Note that a situation in which  $n_{\text{TAB}} - \text{sgn}(n_{\text{SB}}) \notin \{-N_{\text{TAB}}/2, -N_{\text{TAB}}/2 + 1, \dots, N_{\text{TAB}}/2 - 2, N_{\text{TAB}}/2 - 1\}$  may occur. Since the position of  $n_{\text{TAB}} + N_{\text{TAB}}/2$  for  $n_{\text{gr}}$  coincides with  $n_{\text{TAB}} - N_{\text{TAB}}/2$  for  $n_{\text{gr}} + 1$ , this can be solved by modifying the indices accordingly. A similar procedure can be followed for  $n_{\text{TAB}} - N_{\text{TAB}}/2 - 1$ .

From the discussion above, it is clear that for the  $n_{\text{SB}}$ th SB, for which the chunk of bandwidth close to  $f_{\text{max}}$  is coming from the  $n_{\text{gr}}$ th grating response of the  $n_{\text{TAB}}$ th TAB, the optimal chunk of bandwidth around  $f_0$  is provided by the  $n_{\text{gr}}$ th grating of the  $(n_{\text{TAB}} - \text{sgn}(n_{\text{SB}}))$ th TAB. Since the HPBW changes only slowly with frequency and the shift of the grating responses scales linearly with frequency, the optimal switching frequency will be approximate halfway  $f_{\text{max}}$  and  $f_0$  if consecutive SBs are separate by the half power beam width while the optimal switching frequency will be at approximately a quarter of this frequency interval if consecutive SBs are separated by half the HPBW. The latter applies to ARTS when using 151 SBs, so we determine the switch frequency as  $f_{\text{sw}} = 0.75f_{\text{max}} + 0.25f_0$  for even SBs, and as  $f_{\text{sw}} = 0.25f_{\text{max}} + 0.75f_0$  for odd SBs. The resulting switching frequencies are shown in Fig. D.3.

Fig. D.4 shows the sensitivity, expressed relative to the sensitivity of a single WSRT dish, within the CB field-of-view as function of frequency when using the switching frequencies calculated above. These sensitivity data indicate that the 151 SBs described above provide an average sensitivity across the full FoV of 81% of the maximum achievable sensitivity of the WSRT array. The latter would require to form a TAB phase centered at each individual point within the CB field-of-view, i.e., it would, strictly speaking, require the formation of an infinite number of TABs, which is practically infeasible.

### Appendix D.3: Tracking Beams

The grating response of each TAB rotates around the center of the FoV of the CB during an observation. This is illustrated in

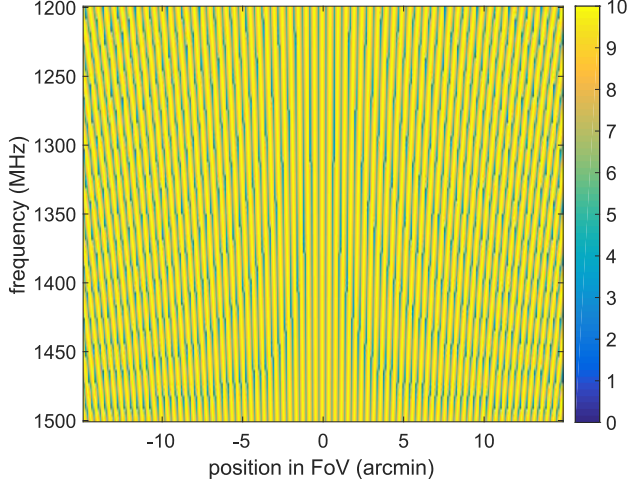


Fig. D.4: Sensitivity within the CB field-of-view as function of frequency when using the switching frequencies shown in Fig. D.3. The sensitivity is expressed in terms of the sensitivity of a single WSRT dish.

Fig. 4e. A given source may therefore traverse multiple SBs during an observation. To track a specific source (or position within the CB) during an observation, we may thus have to concatenate time domain data from multiple SBs. This section describes a procedure to determine which time intervals from which SBs need to be combined to track a desired position within the CB, i.e., to form a Tracking Beam (TB).

Fig. 4e illustrates how the TAB gratings rotate through the FoV during an observation. A specific point within the CB thus moves through the TAB gratings. This perspective, where the coordinate system is fixed to the TAB grating response, is shown in Fig. D.5. At a specific reference time  $t = 0$ , a specific locus can be specified by cylindrical coordinates  $(\theta_0; \phi_0)$ , where  $\theta_0$  measures the distance from the field center and  $\phi_0$  measures the angle between the line from the field center to the locus and the line parallel to the array, i.e., the line orthogonal to the grating

responses. During an observation, this locus will follow a circular path through the CB with an angular velocity given by  $\omega_E$  as indicated by the red track.

The cross-over points between SBs are indicated in Fig. D.5 by vertical dashed blue lines. The area between two such lines is associated with a specific SB that can be identified by its SB index as described in Sec. D.2. If we define the central SB as index 0, we can find the SB associated with a specific locus at a specific instant  $t$  during an observation by finding out in which SB the point  $\theta_0 \cos(\phi_0 + \omega_E t)$  lies (Fig. D.5):

$$n_{\text{SB}} = \left\lfloor \frac{\theta_0 \cos(\phi_0 + \omega_E t)}{\theta_{\text{SB}}} \right\rfloor, \quad (\text{D.10})$$

where  $\lfloor \cdot \rfloor$  denotes rounding.

Each point in the compound beam is covered by the grating response of one of the SBs at  $t = 0$ . Eq. D.10 provides the SB index at each instant  $t$  during the observation. From this, we construct a TB for the full observation for a given point in the CB. The time series associated with these TBs cover the full length of the observation and therefore allow detection of weaker sources than will be feasible to detect during the drift time for an individual SB.

To cover the full field-of-view of the CB, we can define a hexagonally close-packed grid of TBs. As the CBs themselves are arranged in a similar fashion, the ratio between the hexagonal area covered by a TB in a full synthesis observation and the hexagonal area of a CB is then equal to  $(\theta_{\text{SB}}/\theta_{\text{CB}})^2$ . The number of TBs needed to cover a CB will be approximately the inverse, i.e.,  $(\theta_{\text{CB}}/\theta_{\text{SB}})^2$ . If the maximum number of TABs is used to fill the space between the grating responses of Apertif-10,  $\theta_{\text{SB}} = 0.398$  arcmin. If we assume that  $\theta_{\text{CB}} = 30$  arcmin, we will need to synthesise about 5700 TBs. For shorter observations, this number may be reduced as the TBs will have an elongated shape in the direction perpendicular to the array at the mid-point of the observation, which would allow for a larger separation between TBs along that direction.

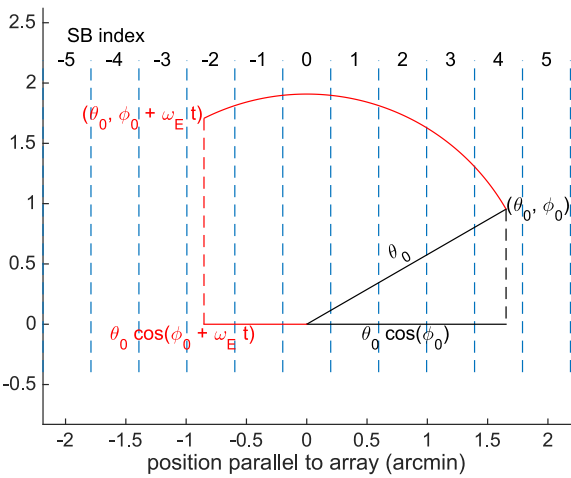


Fig. D.5: Movement of the locus at cylindrical coordinates  $(\theta_0; \phi_0)$  at the start of the observation through the synthesised beams during an observation.